Performance Evaluation of Passive Cavitation Mapping for Estimating Ultrasound-Induced Cavitation Dose

by

Megan YanYan Banh Tran

A thesis
presented to the University of Waterloo
in fulfillment of the
thesis requirement for the degree of
Master of Applied Science
in
Electrical and Computer Engineering

Waterloo, Ontario, Canada, 2023

© Megan YanYan Banh Tran 2023

Author's Declaration

I hereby declare that I am the sole author of this thesis. This is a true copy of the thesis, including any required final revisions, as accepted by my examiners.

I understand that my thesis may be made electronically available to the public.

Abstract

The development of targeted drug delivery technologies to increase the specificity and efficacy of cancer treatments and reduce the reliance on systemic chemotherapy drugs have long been areas of research. Recent advances in therapeutic ultrasound have shown that targeted, enhanced drug uptake can be achieved using ultrasound-mediated microbubble cavitation, a non-invasive drug delivery scheme which leverages the mechanical effects of microbubble cavitation to increase vascular permeability. Spatiotemporal measurement and control of cavitation activity are needed to ensure that only the desired bioeffects (e.g., increased drug penetration) are induced, and the harmful ones (e.g., hemorrhage) are avoided. However, many of the current passive cavitation mapping (PCM) methods lack a standard, system-independent measure of cavitation dose, which impedes the generalizability of research into cavitation-bioeffects relationships. In this thesis, we propose an experimental platform and comparative study that enables us to evaluate the accuracy and performance of PCM methods end-to-end.

The experimental platform was designed to allow for the codetection of a microbubble cavitation target with both an ultrasound array (for PCM) and a hydrophone, which provided an independent reference measurement of cavitation energy (dose). In the comparative study, four popular PCM methods whose absolute cavitation dose magnitudes have not all previously been compared were implemented. Cavitation maps for different frequency bands corresponding to different types of cavitation activity were generated for each input pressure and analyzed for dose accuracy and spatial performance. The key result from the analysis revealed biases and variations in cavitation dose estimation that were both method-specific and frequency-dependent. Additionally, the extracted cavitation dynamics and spatial performance aligned with previous work, validating the experimental platform for simultaneous testing of dose accuracy and spatial performance. These findings confirm that PCM-induced dose bias needs to be accounted for in cavitation dose reporting. Overall, the proposed method was able to quantify differences in cavitation dose accuracy of PCM methods, the first step needed toward the goal of standardizing cavitation dosimetry, which can potentially allow for the smoother clinical translation of cavitation-mediated therapies.

Acknowledgements

I would like to thank Prof. Alfred Yu for giving me the opportunity to pursue my Master's degree at LITMUS under his supervision. I am grateful for his feedback and mentorship which shaped my confidence and development as a graduate student. Our discussions always left me encouraged to investigate deeply, hold my work to high standards, and to continue to persevere.

Next, I want to extend thanks to Dr. Billy Yiu for kindly and patiently helping me throughout my studies with his depth of knowledge and experience in medical ultrasound. I would also like to thank Rebekah, Chris, Robyn, Jason, and all my fellow LITMUS lab members, who were not only amazing coworkers but whose friendships, endless laughs, and daily support I will always cherish.

Finally, I want to express my gratitude to my parents and Alex for their unconditional support and motivation throughout this journey, making sure home was never far away and always lending an ear when I needed. I could not have done this without them.

Table of Contents

Author's Declaration ii

Abstract iii

Acknowledgements iv

List of Figures ix

List of Tables xi

List of Abbreviations xii

List of Symbols xiv

1 Introduction 1

1.1 Chapter Overview 1

1.2 Background 1

1.2.1 The Need for Targeted Drug Delivery 1

1.2.2 Enhanced Drug Delivery with Focused-Ultrasound-Mediated Cavitation . . 2

1.2.3 Existing Cavitation Dosing Methods 3

1.3 Outline of Thesis Study 5

1.3.1 Motivation and Hypothesis 5

1.3.2 Research Objectives 6

2 Cavitation Dose Estimation Using Ultrasound Imaging - Background and Theory 8

2.1 Chapter Overview . . . 8

2.2 Ultrasound-Induced Cavitation . . . 9

2.2.1 Microbubble Composition . . . 9

2.2.2 Ultrasound-Microbubble Interaction . . . 9

2.3 Measuring Cavitation with Ultrasound Imaging . . . 13

2.3.1 Active Ultrasound Imaging . . . 13

2.3.2 Passive Cavitation Mapping . . . 15

2.3.3 Passive Cavitation Detection . . . 16

2.4 Quantitative Passive Cavitation Mapping Beamformers . . . 17

2.4.1 Review of Current PCM Methods . . . 17

2.4.2 Derivation of Certain Absolute Beamforming Algorithms . . . 24

2.5 Chapter Summary . . . 31

3 Method and Platform for Evaluating Passive Cavitation Mapping Algorithms 33

3.1 Chapter Overview . . . 33

3.2 Design of a Cavitation Exposure Platform and Tested Parameters . . . 33

3.3 Ultrasound Array Calibration Methods . . . 37

3.4 Ultrasound Imaging, Preprocessing, and Beamforming . . . 38

3.4.1 Beamformer Implementation Details . . . 38

3.4.2 Cavitation Mapping Signal Processing Pipeline . . . 39

3.4.3 Robust Capon Beamformer Tuning . . . 40

4 Experimental Results of the Passive Cavitation Mapping Evaluations 42

4.1 Chapter Overview . . . 42

4.2 Overview of Beamforming Results . . . 42

4.2.1 Summary B-mode and PCM Overlay . . . 42

4.2.2 Effect of Tuning on RCB . . . 43

4.3 PCM-Estimated Dose at Increasing Pressure 43
4.3.1 Overview 43
4.3.2 Cavitation Dose Thresholds 45
4.4 PCM-Estimated Dose Differences 48
4.5 Source Localization Accuracy 49
4.5.1 Constant Frequency / Varied Pressure 49
4.5.2 Constant Pressure / Varied Frequency 50
4.6 PCM Beam Area Performance 50
4.7 Cavitation Dose vs. Hydrophone 53
4.8 Array Calibration and FUS Characterization Results 55

5 Interpretation and Discussion of Experimental Results 56

5.1 Chapter Overview 56
5.2 Observed Cavitation Doses Versus Expected Cavitation Dynamics 56
5.2.1 Cavitation Thresholds 56
5.2.2 Non-Beamformed Dose is Greater than Beamformed Dose in Ultraharmonic and Broadband Frequencies 58
5.3 Factors Affecting Dose Estimation Difference 58
5.3.1 Equivalence between Time- and Frequency-domain Delay-and-Sum 58
5.3.2 Constant Percent Differences Between Angular Spectrum and Delay-and-Sum 59
5.3.3 Large Variation in Differences Between RCB and Delay-and-Sum 60
5.4 Frequency-Dependent Spatial Performance 61
5.5 Hydrophone as a Passive Cavitation Detector 62
5.6 Advantages and Limitations of the Study 63
5.6.1 Single Experimental Configuration 63
5.6.2 Constant Preprocessing Steps 63
5.6.3 Hydrophone Codetection 64

6 Significance and Conclusions of Study Findings **65**

6.1 Summary of Contributions 65

6.2 Significance of Study Findings 66

6.2.1 Equivalent Beamformer Implementations Reveal Fundamental Differences . 66

6.2.2 Standardization of Cavitation Dose 66

6.3 Future Directions 67

6.3.1 Evaluation of the Wider Scope of PCM Algorithms 67

6.3.2 Combined Approach for PCM Image Formation 67

6.4 Concluding Remarks 68

References **69**

References 69

APPENDICES **78**

A Additional PCM Plots **79**

A.1 Cavitation Map 3D Comparisons 79

A.1.1 Cavitation Maps vs. Frequency 79

A.1.2 Cavitation Maps vs. Pressure 79

A.2 Cavitation Dose vs. Pressure 79

A.3 Percent Difference Cavitation Dose from FDAS vs. Pressure 80

A.4 PCD vs. PCM 80

List of Figures

2.1 Example bubble dynamics, acoustic responses, and bioeffect mechanisms 12

2.2 Overview of cavitation imaging methods 14

2.3 Passive cavitation mapping signal model 24

3.1 Cavitation exposure platform with PCM-PCD codetection 35

3.2 L14-5 element sensitivity calibration methods 38

3.3 RCB tuning example 41

4.1 Example PCM-B-mode overlay with true tube location shown 44

4.2 RCB tuning results 45

4.3 Summary of beamformer outputs at constant frequency and varied pressure 46

4.4 Cavitation dose comparison at constant frequency 47

4.5 Summary of pairwise beamformer cavitation dose differences 49

4.6 Summary of beamformer outputs at constant pressure and varied frequency 51

4.7 Summary of beamformer maximum pixel distance to the tube 52

4.8 PCM beam dimensions over varied frequency 53

4.9 Summary of reference hydrophone PCD readings against PCM 54

4.10 Array sensitivity and FUS beam profile 55

A.1 3D PCM comparisons vs. frequency at 400, 700, and 1000 kPa (N1) 81

A.2 3D PCM comparisons vs. frequency at 400, 700, and 1000 kPa (N2) 82

A.3 3D PCM comparisons vs. frequency at 400, 700, and 1000 kPa (N3) 83

A.4 3D PCM comparisons vs. pressure at H, UH, BB bands (N1) 84
A.5 3D PCM comparisons vs. pressure at H, UH, BB bands (N2) 85
A.6 3D PCM comparisons vs. pressure at H, UH, BB bands (N3) 86
A.7 3D PCM comparisons vs. pressure at 5, 5.5 and 8 MHz bands (N1) 87
A.8 3D PCM comparisons vs. pressure at 5, 5.5 and 8 MHz bands (N2) 88
A.9 3D PCM comparisons vs. pressure at 5, 5.5 and 8 MHz bands (N3) 89
A.10 PCM Dose vs. Pressure at all frequency bands (N1) 90
A.11 PCM Dose vs. Pressure at all frequency bands (N2) 90
A.12 PCM Dose vs. Pressure at all frequency bands (N3) 91
A.13 PCM Dose Differences vs. Pressure at all frequency bands (N1) 91
A.14 PCM Dose Differences vs. Pressure at all frequency bands (N2) 92
A.15 PCM Dose Differences vs. Pressure at all frequency bands (N3) 92
A.16 PCD spectra vs. PCM spectra (N1) 93
A.17 PCD spectra vs. PCM spectra (N2) 93
A.18 PCD spectra vs. PCM spectra (N3) 94

List of Tables

2.1 Review of PCM Algorithms and Performance Metrics 19

3.1 Exposure Platform Experimental Parameters 36

3.2 Beamforming Parameters 39

4.1 Mean ± Std Dev of Distance (mm) from Maximum Pixel to Tube Centre 50

List of Abbreviations

AS Angular Spectrum

BB Broadband

BeW Beam width

DAS Delay-and-Sum

DSPC 1,2-Distearoyl-*sn*-glycero-3-phosphocholine

DSPE 1,2-Distearoyl-*sn*-glycero-3-phosphoethanolamine

FD Frequency-Domain

FDAS Frequency-domain Delay-and-sum

FUS Focused Ultrasound

FWHM Full-Width at Half Maximum

H Harmonic(s)

IQR Inter-Quartile Range

MB Microbubble

PCD Passive Cavitation Detection/Detector

PCM Passive Cavitation Mapping

PEG Polyethylene glycol

PFC Perfluorocarbon

Pos (Source) Position

RC Robust Capon (Beamformer)

RCB Robust Capon Beamformer

RF Radio-frequency (i.e., digitized ultrasound data)

RT Run time

TD Time-Domain

TDAS Time-domain Delay-and-Sum

UH Ultraharmonic(s)

List of Symbols

$\mathbf{1_M}$ Vector of ones of length M

$\mathbf{a}$ Steering vector

c_0 Speed of sound (SI unit: m/s)

ε RCB tuning parameter

f Frequency (SI unit: Hz)

k Frequency index (discrete)

k' Wavenumber (SI unit: rad/m)

λ Wavelength

L Aperture size (linear array)

M Number of elements

$M(f)$ Frequency-dependent array receive sensitivity (Unit: V/Pa)

p Pressure (SI unit: Pa)

ρ Density (SI unit: $\mathrm{kg/m^3}$)

r Radius (SI unit: m)

$\mathbf{R_s}$ Sample covariance matrix

σ Surface tension (SI unit: N/m)

t Time (continuous)

u Spatial frequency (continuous)

v Spatial frequency index (discrete)

Δx Array pitch

Z Acoustic impedance (SI unit: Rayl)

Chapter 1

Introduction

1.1 Chapter Overview

Focused-ultrasound (FUS)-mediated cavitation is an emerging therapy capable of targeted drug delivery in a wide variety of applications throughout the body. Passive cavitation mapping (PCM) algorithms measure and monitor the safety and efficacy of the treatment. This chapter introduces the clinical motivation for FUS-mediated cavitation therapy and the basics of PCM for measuring cavitation dose to maintain safe operation. The first section starts with the clinical importance of targeted therapies in various diseases. The following subsections describe how ultrasound-mediated cavitation can meet this need and how this treatment has been monitored. The final section describes the limitations of current monitoring methods and outlines the motivation, hypothesis, and research objectives of this thesis.

1.2 Background

1.2.1 The Need for Targeted Drug Delivery

Cancer is the leading cause of death in Canada (Brenner et al., 2022), posing a significant health and economic burden. An estimated 233,900 Canadians were diagnosed with cancer, and an estimated 85,100 cancer deaths occurred in 2022 (Brenner et al., 2022). This was estimated to cost Canadians 7.5 billion dollars in direct healthcare costs in 2012 (de Oliveira et al., 2018), with the total societal burden estimated to be 26.2 billion dollars in 2021. The majority of the cost

comes from hospital-based treatments, such as chemotherapy and radiation therapy. Receiving cancer treatment is not easy either – owing to their lack of specificity, it is well known that chemotherapy drugs are systemically cytotoxic to rapidly replicating cells, often causing side effects such as hair loss, diarrhea, and possibly organ damage. As a result, significant research efforts have focused on developing more specific targeted therapeutics, for example, monoclonal antibody-conjugates (Lambert & Berkenblit, 2018). Unfortunately, tumours can uptake only about 0.01% of these therapeutics, limiting their efficacy (Lambert & Berkenblit, 2018). Delivery of drugs is especially challenging in the brain, where the vascular structure of the blood-brain barrier prevents the majority of drugs from leaving the bloodstream and entering the brain tissue (Daneman & Prat, 2015). While developing new therapeutics remains an integral part of achieving specific, targeted treatment of tumours, the advent of other delivery schemes, such as vessel permeabilization through ultrasound-mediated cavitation, shows immense promise for achieving this goal with the existing body of oncological therapeutics.

1.2.2 Enhanced Drug Delivery with Focused-Ultrasound-Mediated Cavitation

Recent advances in therapeutic ultrasound have shown that enhanced uptake of drugs can be achieved using ultrasound-mediated microbubble cavitation (Stride & Coussios, 2019; Kooiman et al., 2020), a drug delivery scheme which leverages the thermal and mechanical effects of microbubble cavitation to increase vascular permeability. Therapeutic ultrasound is particularly well-suited for enhancing targeted drug delivery due to its relative safety, spatial specificity, and non-invasiveness. Using focused ultrasound (FUS) transducers, an ultrasound field can be generated to target its energy to a specific area in the body. In the presence of an oscillating pressure field, gas-cored ultrasound contrast agents (such as microbubbles or MBs) undergo volumetric oscillations – known as cavitation – that act on the fluids and tissues around them. The resultant fluid forces and shockwaves generated by the compression and expansion of MBs can permeabilize the surrounding vessels and tissues, thereby allowing simultaneously circulating drugs or biomolecules to pass through where they previously could not, promoting greater and deeper uptake. Such ultrasound-mediated acoustic cavitation of ultrasound contrast agents has seen recent pre-clinical and clinical translation in various applications. These include clinical trials in blood-brain-barrier disruption for the treatment of Alzheimer's disease (Lipsman et al., 2018) and brain tumours (Mainprize et al., 2019; Idbaih et al., 2019), treatment of liver metastases

(Haram et al., 2023), and breast tumours (Zhou et al., 2022).

1.2.3 Existing Cavitation Dosing Methods

Despite the demonstrated successes, careful measurement and control of the cavitation is essential to avoid harmful bioeffects and ensure safe and effective treatments (Jones & Hynynen, 2019; Hu, Wei, Shen, Chen, & Chen, 2023). Cavitation dose is generally defined as the energy emitted by cavitating contrast agents within the target area onto the surrounding tissue. Vessel permeabilization has been shown to be possible even at low cavitation doses produced by low ultrasound pressure amplitudes (Stride & Coussios, 2019). However, when MBs are excited at high ultrasound intensity, the resulting increase in cavitation dose and changes in the cavitation regime can result in undesired effects such as hemorrhaging. Since different doses and regimes of cavitation induce different effects, successful treatment monitoring depends on our ability to discern, quantify, and localize the cavitation dose in and around the desired volume (Hu et al., 2023). Many studies have attempted to investigate links between ultrasound parameters, relative cavitation level, and various bioeffects in *in vitro*phantoms (Smith & Coussios, 2020; Martinez, Bottenus, & Borden, 2022), individual cells (Duan, Yu, & Wan, 2019; Duan, Lo, Lee, Wan, & Yu, 2022), *ex vivo* organs (Chen, Brayman, Evan, & Matula, 2012), *in vivo* small animal models (Chen & Konofagou, 2014), and large animal models (Wu et al., 2014). The following subsections describe some advantages and disadvantages of different methods for measuring cavitation activity at different scales.

Optical Imaging

Optical imaging techniques have previously been used to directly observe cavitation dynamics in isolation using high-speed imaging and shadowgraphic imaging (Bouakaz, Versluis, & de Jong, 2005) as well as the mechanisms for bubble-cell interactions such as sonoporation (Hu, Wan, & Yu, 2013) using live confocal microscopy and high-speed imaging (Chen, Brayman, Kreider, Bailey, & Matula, 2011). High-speed imaging of a cavitating bubble while tracking its radius is often used to confirm theoretical models of bubble behaviour (Dollet, Marmottant, & Garbin, 2019). While also helpful in measuring macro bioeffects like lesion size (H.-C. Lin, Fan, Ho, & Yeh, 2020) and analyzing cellular mechanisms (in combination with downstream cellular bioeffect

assays) (Duan et al., 2022), the use cases for optical imaging for quantifying cavitation dose are limited. Although the changing radius of a single bubble can sometimes be observed, it is difficult to translate this to larger-scale studies where there are often thousands of bubbles interacting in clouds or clusters (Roovers et al., 2019). Lastly, the limited field of view and the requirement for optically transparent samples further limit optical imaging from dosing cavitation *in vivo*. As such, optical imaging of cavitation provides only qualitative information regarding cavitation dose.

Acoustic Monitoring

Acoustic monitoring of cavitation activity is the only quantitative method that can bridge the findings between *in vitro* and *in vivo* studies. This group of techniques utilizes ultrasound transducers to capture and image the ultrasound-frequency acoustic emissions generated by the cavitating microbubbles themselves. When these emissions are measured using a single-element ultrasound transducer, this is known as passive cavitation detection (PCD). Standard diagnostic ultrasound arrays can also measure these emissions and subsequently beamform them with passive cavitation mapping (PCM) algorithms, producing spatial maps that localize the source of the cavitation activity and compute the cavitation dose. PCM algorithms utilize many of the same imaging principles as conventional ultrasound to quantify and generate maps of cavitation activity.

The spectral content of the pressure waves generated by cavitating microbubbles is related to their oscillation regime, amplitude, and frequency. Harmonics and ultraharmonics of the excitation frequency are associated with stable cavitation, which is typically of lower amplitude and associated with hemorrhage avoidance. The sum of these spectral components is thus referred to as stable cavitation dose (Wu et al., 2014). Broadband signals are associated with the more violent shockwaves produced by inertial cavitation (bubble collapse) at high excitation pressures. The sum of these spectral components is referred to as inertial cavitation dose. With this knowledge, many different signal processing methods have been developed to filter the harmonic, ultraharmonic, and broadband spectral components of cavitation emissions and beamform them into maps of the cavitation energy. However, discrepancies in reported values arise due to the large variety of signal processing methods (beamforming and filtering), ultrasound systems (bandwidth and sensitivity), and ultrasound propagation paths employed in different experiments and

applications. Additionally, many implementations of PCM in biologically relevant experiments report cavitation energy as normalized or relative units, which depend on the specific ultrasound system used, as opposed to absolute units (such as Joules), which are obtained after system calibration. Therefore, a standard metric of absolute cavitation dose remains an important missing piece in establishing generalizable, absolute relationships between cavitation activity and bioeffects that are independent of setup (Hu et al., 2023). As a result, comparison of *in vitro* and pre-clinical results between research groups remains challenging due to heterogeneous reporting of absolute/relative dosage units, spectral bandwidths included in the analysis, receive sensitivity of PCM receivers, and the PCM beamformers themselves.

Unifying the reported cavitation doses and the methods used to compute them is needed to achieve standardization of cavitation dosimetry. The first step would be to identify and characterize the sources of dose magnitude error or bias introduced by the different parts of the PCM processing pipeline (e.g., filtering, beamforming, bandwidth). Next, determine the most critical system-independent dose metrics and errors through further bioeffects studies. As new PCM methods are developed and evaluated, the best-performing and most accurate methods will emerge and be more widely adopted. Alternatively, researchers can develop techniques for error compensation between PCM algorithms. Lastly, standardize the reporting of cavitation dose so that the quantities measured in these studies are directly comparable. In the current state of the literature, the quantification accuracy of the absolute dose of PCM algorithms has rarely been experimentally validated between methods or against independent ground truth reference values. Such a performance evaluation experiment could more clearly demonstrate the biases between PCM methods and contribute to the first step toward developing standard cavitation dosimetry.

1.3 Outline of Thesis Study

1.3.1 Motivation and Hypothesis

As will be described in detail in Chapter 2, numerous PCM algorithms exist for localizing cavitation activity and quantifying cavitation dose. However, many PCM beamformers are not implemented quantitatively with equivalent models for cavitation signal spreading and with absolute units. Many existing evaluations focus primarily on spatial performance without focusing on dose magnitude differences between algorithms. As such, there is a need for a systematic evaluation

of PCM algorithms that can simultaneously compare their absolute dose accuracy and spatial performance. This would provide a more complete picture of the advantages and disadvantages of each algorithm and provide a framework for evaluating the performance of new algorithms that is generalizable to different ultrasound systems. In this thesis study, we try to address this need first by considering four commonly used beamformers: time-domain delay-and-sum (TDAS), time-domain robust Capon beamformer (RCB), frequency-domain delay-and-sum (FDAS), and frequency-domain angular spectrum approach (AS). We are guided by two hypotheses:

Primary hypothesis: By implementing different beamformers with the same bubble signal models and with the necessary scaling factors to obtain absolute units, different beamformers will differ both in cavitation dose estimation and spatial performance metrics. Specifically, TDAS and FDAS should yield the same result (being just two implementations of the same beamformer), but RCB and AS will both differ from either DAS. The results will be dependent on the cavitation behaviour and frequency bandwidths beamformed.

Secondary hypothesis: A reference hydrophone that codetects the total cavitation dose will have a smaller difference in dose estimates to one of the delay-and-sum algorithms (FDAS, TDAS, or RCB) compared to non-delay-and-sum beamformers like AS.

1.3.2 Research Objectives

The overall goal is to design an end-to-end testing framework for PCM algorithms. This is to be accomplished by achieving the following objectives:

1. Devise an *in vitro* experimental platform for the controlled codetection of a variety of cavitation behaviours with an ultrasound array (for PCM) and hydrophone (for PCD).

2. Calibrate the ultrasound array to enable absolute, quantitative estimation of cavitation dose.

3. Implement four commonly used beamformers with absolute quantitative scaling factors and compensation for spherical spreading.

4. While keeping preprocessing and postprocessing steps the same, evaluate the dose estimation and spatial performance of each beamformer against both cavitation behaviour (mod-

ulated by excitation pressure) and beamformed frequency (indicative of different cavitation behaviour) using the proposed *in vitro* experimental platform.

Chapter 2

Cavitation Dose Estimation Using Ultrasound Imaging - Background and Theory

2.1 Chapter Overview

This thesis primarily focuses on evaluating PCM algorithms for quantifying cavitation dose. Ultrasound contrast agents like microbubbles (MBs) have been widely used in ultrasound imaging, and the same physical principles of cavitation and imaging principles apply to quantitative PCM for therapeutic use, with some adaptations. This chapter aims to present the fundamental principles of the acoustic properties of microbubbles and the use of ultrasound imaging for measuring cavitation. Section 2.2 describes microbubble composition, the acoustic response of microbubbles when exposed to an ultrasound field, and the factors governing microbubble cavitation. The following section (2.3) introduces the principles of active imaging, passive imaging, and passive detection as three methods for measuring bubble activity. Next, an overview of existing quantitative PCM beamformers and their validation methods is presented in Section 2.4. Finally, the last section derives the quantitative beamformers with absolute units that are used in the thesis study.

2.2 Ultrasound-Induced Cavitation

2.2.1 Microbubble Composition

Microbubbles are micrometre-sized, gas-cored bubbles that are typically encapsulated with a shell of phospholipids or proteins. To serve both diagnostic and therapeutic applications, MB suspensions are injected intravenously (Kooiman et al., 2020) and must be stable within the body long enough to reach the target area and then have the appropriate properties to enhance image contrast and/or deliver drugs. Their chemical and physical properties are designed to accomplish these goals. MBs typically range in diameter from 0.5-10 μm (Roovers et al., 2019). The internal pressure difference required to stabilize a bubble in a given medium is called the Laplace pressure (ΔP) and depends on the surface tension (σ) and radius (r) of the bubble:

$$\Delta P = 2\sigma/r \tag{2.1}$$

Compared to unshelled, free-gas bubbles of the same size, the phospholipid or protein shell often contains surfactants which reduce the surface tension and thereby the Laplace pressure required to stabilize the bubble. The shell also slows gas exchange between the bubble and liquid medium, which would also otherwise reduce the radius and accelerate the dissolution of the bubble. Lipid and protein shells also increase the stiffness and viscosity of the interface, which resists oscillations and dampens cavitation (Roovers et al., 2019). To further increase stability and slow down gas exchange, MBs are often filled with heavy non-water-soluble gases such as perfluorocarbon (PFC) gases like decafluorobutane (DFB, chemical formula C_4F_{10}) instead of water-soluble gases such as nitrogen or oxygen (Roovers et al., 2019). For therapeutic applications such as solid tumour drug delivery, the most popular microbubbles are lipid-shelled and can be modified to include ligands such as sugars, antibodies, and anti-cancer drugs to target specific tumour biomolecules or act as drug transporters (Kooiman et al., 2020). The compressibility of gas is what allows for bubble stabilization and pressure-responsive volumetric oscillations to take place.

2.2.2 Ultrasound-Microbubble Interaction

Single-Microbubble Cavitation

Figure 2.1 summarizes some of the key features of microbubble cavitation which are described below. In this study, we will focus on the behaviour of lipid-shelled MBs. Bubble behaviour

in an acoustic field has been extensively studied (Dollet et al., 2019) through both modelling and observation, with the key pressure-dependent behaviours summarized in Figure 2.1A. In response to an oscillating pressure field of a given fundamental frequency f_0, a variety of time-evolving, pressure-dependent bubble dynamics can be observed. At low pressures (<100 kPa at 1MHz), bubbles undergo linear, spherical volumetric oscillations (Stride & Coussios, 2019) which re-radiate the incident ultrasound field at its fundamental frequency. As pressure increases (approximately 100-500 kPa), the volumetric oscillations become non-linear, and the higher harmonics of the fundamental frequency can be seen in the acoustic response (Figure 2.1B). At even higher pressures (>500 kPa), the oscillations become increasingly non-linear, with fractional harmonics (i.e. ultraharmonics and subharmonics) appearing in the acoustic response (Stride & Coussios, 2019). In some cases (depending on the shell properties), non-spherical vibration modes can also appear, and thresholded behaviour caused by shell buckling and rupture can occur. Finally, at high enough pressures, the microbubbles can undergo transient behaviours such as collapse, generating shockwaves which appear as broadband noise in the frequency spectrum. After collapse, the microbubble gases may dissolve or leave behind small fragments.

These cavitation dynamics have been hypothesized and observed to produce bioeffects in various ways (Figure 2.1C). The microbubble volumetric oscillations impart forces on the fluids surrounding them, producing fluid motion around the bubble (microstreaming). The fluid microstreaming applies both shear and normal forces on the vasculature, opening holes and tears in cell membranes or widening junctions between cells. Fluid forces from acoustic radiation or other cavitation sources can also push bubbles into adjacent cells (tunnelling). At high pressures, bubbles can produce shockwaves which can also disrupt membranous structures. Additionally, highly asymmetric boundary conditions may cause asymmetric bubble collapse, resulting in the formation of fluid microjets which can puncture cell membranes. Within a small, flexible tube such as a capillary, bubble collapse can produce negative pressures of sufficient magnitude to invaginate the vessel walls toward the point of collapse as shown (Chen et al., 2011, 2012), or distend vessel walls during expansion.

The term 'stable' cavitation is often used to describe microbubble behaviour involving prolonged oscillations, namely those non-linear vibrations that produce harmonic and ultraharmonic acoustic emissions. On the other hand, the term 'inertial' cavitation is generally ascribed to transient bubble behaviour such as bubble collapse. This is derived from the notion that this

behaviour is dominated by the inertia of the surrounding fluid as opposed to the bubble compression.

As harmonic oscillators, the resonance frequency of bubbles of a given radius R_0 is typically estimated by determining the resonance frequency of a linear harmonic oscillator model of a microbubble (Roovers et al., 2019; Jong, Bouakaz, & Frinking, 2002). However, modifications to this equation have been made to include shell properties (Jong et al., 2002). Equation 2.2 (Jong et al., 2002) shows the resonance frequency of a free, uncoated bubble. Here, κ is the polytropic index of the gas core ($\kappa = 1.1$ for heavy gases such as PFCs (Roovers et al., 2019)), ρ is the medium density, P is the ambient pressure experienced by the bubble, and R_0 is its radius at rest.

$$f_r = \frac{1}{2\pi R_0}\sqrt{\frac{3\kappa P}{\rho}} \tag{2.2}$$

As shown in Equation 2.3, the shell properties add an additional term, which increases the resonance frequency of a given bubble. Here, S_{shell} refers to the stiffness and m the mass of the shell (Jong et al., 2002).

$$f_r^2 = \frac{1}{4\pi^2 R_0^2}\frac{3\kappa P}{\rho} + \frac{S_{shell}}{4\pi^2 m}. \tag{2.3}$$

In general, bubbles will still respond to driving frequencies within 1 MHz of the resonance frequency (Roovers et al., 2019), but the oscillation amplitudes are maximal at their resonance frequency.

Multi-Microbubble Cavitation

Although single-bubble modelling is well studied, predicting the cavitation dose resulting from a population of MBs in the body is more difficult due to heterogeneity in MB size, the interactions between bubbles, and changing boundary conditions. At present, the preparation method of commercial MBs results in a population of MBs with a relatively wide distribution of radii, or polydisperse radii. As a result, when exposed to the same ultrasound field, the majority of MBs are excited outside their resonance frequency, producing a heterogeneous cavitation response, which complicates research into the bioeffects (Roovers et al., 2019). Another reason MBs might be driven outside their resonance frequency is a preference for lower frequency ultrasound (¡1 MHz) which achieves deeper penetration and bypasses structures such as the skull, which absorbs more ultrasound at higher frequencies (Jones & Hynynen, 2019). Fortunately, there have been

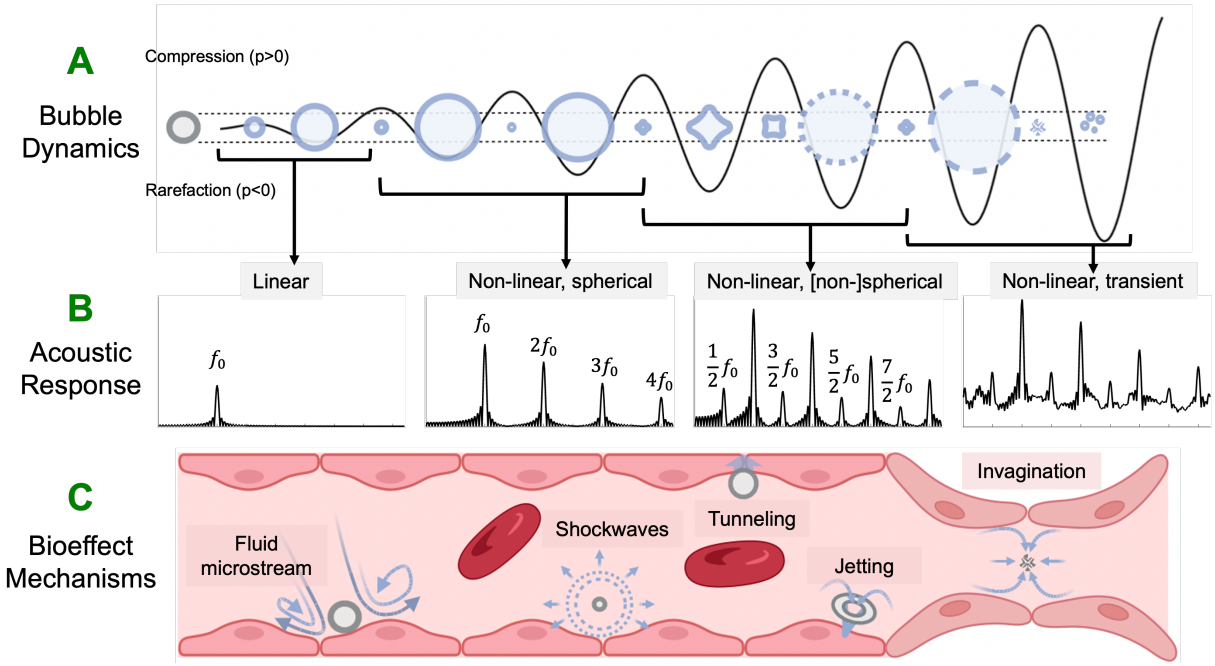


Figure 2.1: Examples of: A) bubble dynamics with increasing pressure, B) acoustic responses with increasing pressure, and C) cavitation-induced bioeffect mechanisms. A) and C) were created in Biorender.com

developments in the manufacturing of size-isolated, or monodisperse, MBs (Segers et al., 2018) which are purported to produce more homogeneous cavitation behaviour.

In addition to size distribution, the concentration of MBs is another important factor in the delivery of cavitation-mediated therapies. At low concentrations, MB cavitation approaches the single-bubble case where there are minimal bubble-bubble interactions (Dollet et al., 2019). As the concentration increases, the average distance between individual MB decreases, which increases the likelihood of bubble-bubble interactions such as coalescence (the merging of multiple bubbles into one larger bubble) and interactions between the pressure field scattered off an MB toward other nearby MBs. At high concentrations, the layer of MBs closest to the excitation transducer can reflect a large fraction of the incident ultrasound energy, shielding the MBs behind them from the field and reducing the total cavitation activity (Roovers et al., 2019). Additionally, the behaviour of MB clusters or clouds differs from single MBs, whereby the resonance frequency of the cluster approaches that of a single bubble with an equivalent total volume (Roovers et al., 2019).

Lastly, it is important to consider that there is no one-to-one mapping between cavitation dynamics and acoustic response, especially considering the heterogeneous response of bubble populations. The goal of cavitation mapping and dosing is to compute useful quantitative metrics that can be shown to correlate to measurable biological responses in different applications. While fine-tuning MB dose for a specific therapeutic application is not the focus of this thesis, knowledge of the multi-faceted factors affecting MB cavitation is essential for selecting appropriate experimental parameters for testing PCM algorithms.

2.3 Measuring Cavitation with Ultrasound Imaging

To understand how we can quantify cavitation through imaging methods, we will compare the physical principles of conventional (active) ultrasound imaging to the passive methods used for cavitation imaging, as in Figure 2.2.

2.3.1 Active Ultrasound Imaging

Conventional pulse-echo (active) ultrasound imaging (Figure 2.2A) is typically accomplished by transmitting a short pulse of ultrasound (at t=0) with centre frequency f_c through a piezoelectric ultrasound transducer array placed on the skin. The ultrasound pressure wave propagates into the tissue and interacts with scatterers in the tissue. These particles scatter the incident pressure waves through a combination of backscattering and Rayleigh scattering (where the particle size is larger than the wavelength). Scattering and reflection occur due to a mismatch in acoustic impedance,

$$Z = \rho c_0 \tag{2.4}$$

the product of the medium density, ρ and speed of sound, c_0, between the medium and the scatterers. The backscattered echoes are then detected by the transducer array elements and digitized. The ultrasound pulse propagates for a known, two-way time-of-flight from the transducer to the point of interest (a pixel on the final image) and back to each transducer element. The delay-and-sum beamforming operation takes the point in each array element's analytic signal envelope (denoted by the red dots) that corresponds to the time-of-flight to each element and sums them coherently. The amplitude of the delayed-and-summed envelope determines the pixel brightness. When repeated for every pixel, this forms a Brightness-mode or B-mode image.

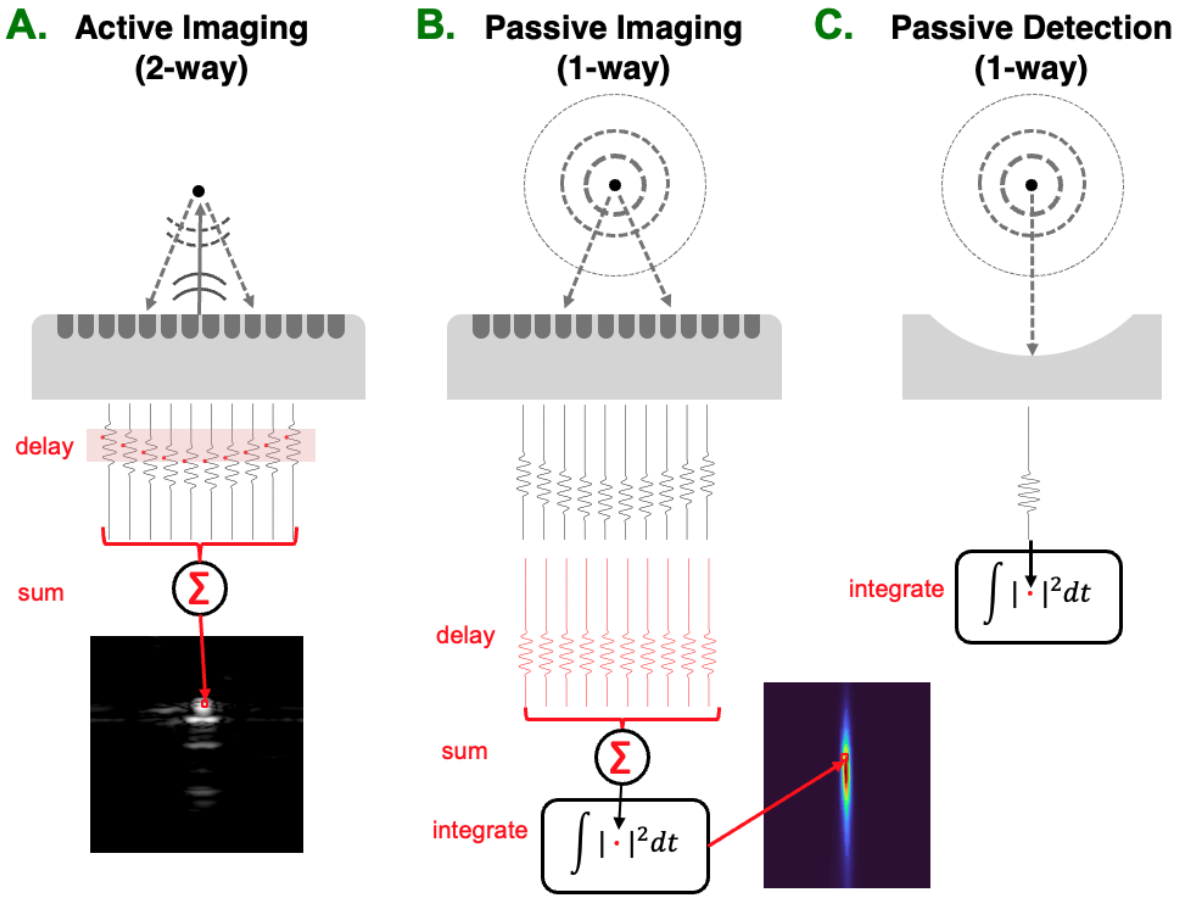


Figure 2.2: Overview of cavitation imaging methods. A) Active (pulse-echo) imaging, B) Passive quantitative cavitation mapping, C) Passive quantitative cavitation detection.

The spatial resolution of pulse-echo ultrasound imaging is proportional to the wavelength and duration of the excitation pulse.

In this form of active imaging, bubbles will appear as brighter pixels due to the mismatch in acoustic impedance between the bubbles' gas cores and the surrounding medium, as well as the reradiation of the ultrasound through cavitation. The cavitation behaviour described in the previous section can also be leveraged in harmonic contrast imaging (cardiac), where the RF data is first filtered to the 2nd (or higher) harmonic of the centre frequency ($2f_c$) before beamforming to isolate echoes originating from bubble cavitation (Frinking, Bouakaz, Kirkhorn, Cate, & de Jong, 2000). A therapeutic application of active cavitation imaging is in monitoring high-intensity focused ultrasound (HIFU) therapies, where FUS transducers are used to thermally

and mechanically ablate tissues (without the assistance of exogenous MB contrast agents). Active cavitation imaging can monitor the nucleation and persistence of endogenous cavitation bubbles and the resulting changes in tissue echogenicity using B-mode imaging (Coussios, Farny, ter Haar, & Roy, 2007). However, active cavitation imaging has mainly previously been used to localize and identify the onset of bubbles rather than for cavitation quantification purposes.

2.3.2 Passive Cavitation Mapping

In contrast, passive imaging (Figure 2.2B) techniques have been developed for estimating the energy of cavitation through direct measurement of the bubbles' acoustic emissions. Passive imaging differs from active imaging in that it assumes the ultrasound pulses are generated from points within the imaging plane, possibly at random points in time, rather than as echoes from pulses generated by the array. The pulses are assumed to undergo one-way propagation, and a relative delay for each element is based on the one-way time-of-flight from the point of interest toward the array. Since we do not have prior knowledge about the timing of the sources, each element's entire analytic signal is time-shifted by the one-way time-of-flight to induce a relative phase shift before coherent summing. Sources originating from the pixel of interest will coherently sum maximally, whereas outside areas of cavitation, the signals will sum destructively. Assuming that the only acoustic sources in the field of view are due to cavitation, the signal energy of the resulting beamformed signal, $\tilde{s}(t)$, is thus a measure of the cavitation energy.

$$E_{rel} = \int_T |\tilde{s}(t)|^2 dt \tag{2.5}$$

For a scanner whose frequency-dependent pressure sensitivity is unknown (i.e., uncalibrated scanner), the raw radio-frequency (RF) data is in units of Volts or digital counts. Thus, the cavitation energy would be reported after normalization to the maximum pixel or in relative units such as $\frac{\mathrm{J{\cdot}Pa^2}}{\mathrm{V^2}}$ which acknowledge the unknown calibration constant, in units of V/Pa. Absolute cavitation energy is system-independent and described in physical units of energy, J. To compute this, the array must be calibrated to convert the voltage signal to a pressure signal, $p(t)$, and the signal energy over an interval T must be scaled as follows,

$$E_{abs} = \frac{4\pi d^2}{\rho c_0} \int_T |p(t)|^2 dt \tag{2.6}$$

where the $4\pi d^2$ scaling factor compensates for spherical spreading from a distance d to the point of interest, and ρc_0, the acoustic impedance, is required. The signal model is described in further

detail in Section 2.4.2. Unlike active imaging, the spatial resolution of the passive image is not a function of the cavitation pulse frequency or duration but of the array's frequency-dependent diffraction pattern (Haworth, Bader, Rich, Holland, & Mast, 2017). The spatial resolution can be approximated with the Fresnel approximation of a line source with the same width as an array aperture, L. The -6dB axial depth of field and lateral beamwidth for an on-axis point source located at depth z are thus given by (Haworth et al., 2017)

$$D_{6dB} = \frac{9.69\lambda z^2}{L^2} \tag{2.7}$$

$$W_{6dB} = \frac{1.21\lambda z}{L} \tag{2.8}$$

where λ is the wavelength of interest, related to the beamformed frequencies by the relation $\lambda = c_o/f$.

Another factor to be aware of is that due to the wide bandwidth of cavitation emissions, the array should ideally have as wide bandwidth as possible to capture the full spectrum of cavitation activity. This cannot be easily modulated for most commercial diagnostic imaging arrays, so signals are often bandpass filtered to the array's bandwidth before processing. The array's bandwidth or analyzed bandwidth must be considered in energy dose reporting since it affects the total estimated energy, especially for inertial cavitation.

2.3.3 Passive Cavitation Detection

PCD (Figure 2.2C) is a simpler method of measuring cavitation activity involving only a single-element transducer to detect the acoustic cavitation emissions and, thus, a single ultrasound signal. A measure of cavitation energy can be obtained using the same principles as in PCM, assuming a calibrated sensor. Cavitation emissions have previously been measured using hydrophones (unfocused) (Jiang, Sujarittam, Yildiz, Dickinson, & Choi, 2022) and focused transducers (Coussios et al., 2007). Because of the single-element limitation of PCD, there is often a trade-off between spatial specificity and sensitivity. Unfocused receivers such as hydrophones and piston transducers can detect signals from a wider area. However, the spatial origin of the received signals is uncertain, and they may not always be sensitive enough to detect low-amplitude cavitation signals. Focused receivers tend to be more sensitive and can detect cavitation emanating from their focal area but are insensitive to any cavitation activity outside of it. The different forms

of transducers make them suitable for different applications with different geometries, treated volumes, and treatment goals.

2.4 Quantitative Passive Cavitation Mapping Beamformers

2.4.1 Review of Current PCM Methods

While the delay-and-sum premise of passive cavitation mapping is relatively simple, many algorithms have been developed that improve the spatial resolution and other performance metrics. A review of the current quantitative beamformers for passive cavitation mapping of cavitation dose for drug delivery and brain applications is presented in Table 2.1. The PCM algorithm publications are first grouped based on their characteristics, like their base mode of operation (e.g., frequency-domain delay-and-sum with/without second-order statistics), then the beamforming particulars such as adaptive tuning parameters, and whether or not they have been demonstrated an estimate of absolute cavitation power or energy. Last, to highlight the trends in the performance analysis methods, the spatial and dose performance metrics are presented, as well as the details of any comparative analysis against other PCM algorithms or other means (such as optical imaging). Note that this is not a complete review of all the PCM literature, but publications were selected to demonstrate the breadth of methodology, implementation, and performance evaluation.

As shown in Table 2.1, many different beamforming techniques have been demonstrated for passive cavitation mapping. Most studies focus mainly on the spatial resolution performance (in terms of normalized beamwidth and contrast) and localization accuracy of a couple of algorithms. In terms of spatial metrics, we see measurements of the axial and lateral beamwidth (denoted BeW), including the main lobe FWHM (full-width at half maximum), -3dB beamwidth, -6dB beamwidth, total beam area of the top 50% of pixel values, and point-spread function. Additionally, source position error (denoted Pos) is often described, as well as various contrast ratios (denoted CAR) describing signal-to-noise ratio or signal-to-artifact ratio. The spatial resolution, presence of artifacts, and localization accuracy are certainly all important performance metrics in PCM since they can directly impact one's ability to discern cavitation occurring within the desired treatment area from that outside it. Poor spatial resolution and the presence of side lobes and tail artifacts can obscure the presence of nearby cavitation sources, and the cavitation area

can appear larger than it truly is.

However, toward the goal of quantitatively dosing cavitation for establishing relationships to bioeffects, far fewer studies have demonstrated both computations of energy-based cavitation dose and compared their absolute magnitudes to other beamformers. Those that have are highlighted in green, and they encompass TDAS (Gyöngy & Coussios, 2010a), TD-RCB (Coviello et al., 2015), FDAS (Haworth et al., 2017), and aperture-domain wavefront fitting (Telichko, Lee, Hyun, et al., 2021). Those denoted as 'Rel' (Relative) may or may not have proposed an energy- or intensity-based dose but made their performance comparisons (to other beamformers) using normalized (or relative, uncalibrated) units. Furthermore, no study attempts to validate the absolute cavitation dose against an independent reference value using a different technique (i.e., a secondary transducer or passive cavitation detector). However, in Gray, Lyka, and Coussios (2018) and Kamimura et al. (2021) (highlighted in orange), a PCD is used to qualitatively confirm overall cavitation dose trends as well as the presence of harmonics, ultraharmonics, and broadband spectral components.

Through this thesis study, described in Section 1.3, we hope to address this research gap highlighted by this literature review by focusing primarily on cavitation dose magnitude differences with a reference PCD, along with the spatial performance.

Table 2.1: Review of PCM Algorithms and Performance Metrics

TD=Time domain, DAS=Delay and sum, FD=Frequency domain, ToF=Time of flight, AS=Angular spectrum, RC=Robust Capon, BeW = Beamwidth or beam area (includes any of FWHM, -3dB, -6dB, min resolvable distance, A50, spot size), CAR=Cavitation-artifact ratio (includes other contrast metrics), Pos=Source position error, EC=Energy comparison (includes energy estimation ratios, difference, direct comparisons), RT=Run time, Qual.=Qualitative comparisons, MRI=Magnetic resonance imaging, HSOI=high-speed optical imaging

Citation	**Base Algorithm**	**Variation/Detail**	**Energy-based Dose**	**Quantitative Performance Metrics**	**Experimentally Validated Against**
Gyöngy and Coussios (2010a)	TD-DAS	-	Abs	-	-
Gyöngy and Coussios (2010b)		-	Rel	Qual.	Bmode
O'Reilly et al. (2014)		-	Rel	BeW, Sep	MRI
Kamimura et al. (2021)		Sparse matrix implementation	Rel	EC(qual), BeW, RT	PCD (non-calibrated) MRI
Coviello et al. (2015)		RC	Abs	EC, BeW, CAR, Pos	Gyöngy and Coussios (2010a) Capon (1969)
Gray and Coussios (2018)		RC with attenuation compensation	Abs	EC, BeW	Gyöngy and Coussios (2010a)
Gray et al. (2018)		RC with element diffraction compensation	Abs	EC, BeW	Gyöngy and Coussios (2010a) PCD (non-calibrated)

Continued on next page

Citation	Base Algorithm	Variation/Detail	Energy-based Dose	Quantitative Performance Metrics	Experimentally Validated Against
Lu et al. (2018)		RC in signal subspace of eigenspace	Rel	BeW, CAR	Gyöngy and Coussios (2010a) Coviello et al. (2015)
C. Li et al. (2020)		RC with angle response steering vector	Rel	BeW, CAR	Gyöngy and Coussios (2010a) Coviello et al. (2015)
Boulos et al. (2018)		Phase coherence factor weighting	Rel	Pos	Gyöngy and Coussios (2010a)
Boulos et al. (2016)			Rel	BeW, Pos	Gyöngy and Coussios (2010a) Fink et al. (2003)
Bae et al. (2021)		Signal coherence factor weighting	Rel	BeW, RT	Gyöngy and Coussios (2010a) Lu et al. (2018)
Lyka et al. (2018)		Robust beamforming by linear programming (higher-order statistics)	Abs	EC, BeW	Gyöngy and Coussios (2010a) Coviello et al. (2015)
Lu, Yu, et al. (2019)		Dual apodization with cross-correlation	Rel	BeW, CAR, Pos, RT	Gyöngy and Coussios (2010a)

Continued on next page

Citation	Base Algorithm	Variation/Detail	Energy-based Dose	Quantitative Performance Metrics	Experimentally Validated Against
Lu et al. (2020)		Multi apodization with cross-correlation	No	BeW, CAR	Gyöngy and Coussios (2010a) Lu, Yu, et al. (2019)
Davies et al. (2021)	ToF-gated TD-DAS		Rel	BeW, Pos	Gyöngy and Coussios (2010a) Coviello et al. (2015) Histology
Burgess et al. (2018)			Rel	Qual.	MRI
Lu, Li, et al. (2019)	TD Delay-Multiply-Sum		Rel	BeW, CAR, Pos, RT	Gyöngy and Coussios (2010a)
H.-C. Lin et al. (2020)	TD Pulse compression, Dual-frequency Chirp excitation		No	BeW, CAR, SNR	Bmode *Ex vivo* staining

Continued on next page

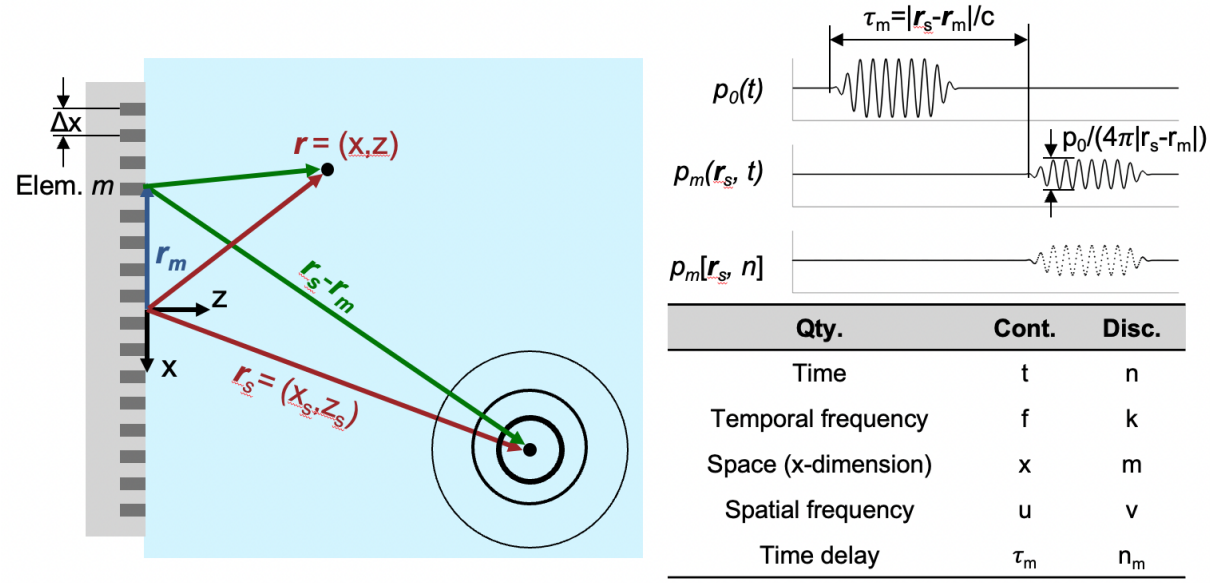
Citation	Base Algorithm	Variation/Detail	Energy-based Dose	Quantitative Performance Metrics	Experimentally Validated Against
Salgaonkar et al. (2009)	FD-DAS	-	Rel	BeW, Pos	Bmode
Haworth et al. (2012)			Rel	BeW	-
Haworth et al. (2017)			Abs	-	-
Arvanitis et al. (2015)		Skull SoS, absorption corrections	Rel	BeW, Pos	MRI, CT
H. Abadi et al. (2013)		Frequency-sum	Rel	Qual.	-
Polichetti et al. (2021)		RC	Rel	BeW, CAR, Pos	Haworth et al. (2012) HSOI
		P-th root compression	Rel	BeW, CAR, Pos	
		Multiple signal classification (MuSiC) method	No	BeW, CAR, Pos	
Lu et al. (2017)		RC + Frequency-sum	Rel	BeW, CAR	Haworth et al. (2012), H. Abadi et al. (2013)
Kim et al. (2020)		Pre-beamforming Hilbert filter + downsampling	Rel	BeW, Qual.	Haworth et al. (2012)

Continued on next page

Citation	Base Algorithm	Variation/Detail	Energy-based Dose	Quantitative Performance Metrics	Experimentally Validated Against
Arvanitis et al. (2017)	FD-AS	-	Rel	BeW, Pos, RT, SBNR	Gyöngy and Coussios (2010a) Haworth et al. (2012) MRI
Schoen and Arvanitis (2020a)		Sound speed correction for continuously stratified media	Rel	Pos, RT	Arvanitis et al. (2017)
Schoen and Arvanitis (2020b)		A priori sound speed correction for heterogeneous media	Rel	BeW, Pos, RT, SBNR	Arvanitis et al. (2017)
Telichko, Lee, Jakovljevic, and Dahl (2021)	Aperture-Domain Wavefront Fitting for Source Localization		Abs	EC, Pos, Qual.	Gyöngy and Coussios (2010a)
Telichko, Lee, Hyun, et al. (2021)					Holfort et al. (2009)

2.4.2 Derivation of Certain Absolute Beamforming Algorithms

In this thesis, we focus on four popular beamformers: Time-domain delay-and-sum (also referred to as time exposure acoustics) (Gyöngy & Coussios, 2010a), its frequency-domain counterpart, frequency-domain delay-and-sum (FDAS) (Haworth et al., 2012, 2017), the angular spectrum (AS) approach (Arvanitis et al., 2017), and the time-domain Robust Capon beamformer (RCB) (Coviello et al., 2015). These were chosen as the most prevalent beamformers in the PCM literature used to study bioeffects but whose absolute dose values had not previously been compared against a reference value. The following subsections derive the quantitative implementations in this thesis that consider the effects of both discrete-time digital processing and compensation for spherical spreading. The implementations may differ slightly from the way they were initially implemented in the cited sources but allow for direct comparison with absolute values. The analysis steps are based on the work of Haworth et al. (2017). We will first present the continuous-time and continuous-frequency versions of the beamformers, followed by the discrete-time and discrete-frequency versions.



Qty.	Cont.	Disc.
Time	t	n
Temporal frequency	f	k
Space (x-dimension)	x	m
Spatial frequency	u	v
Time delay	τ_m	n_m

Figure 2.3: Passive cavitation mapping signal model. The inset table summarizes the continuous (Cont.) and discrete (Disc.) time and frequency notation used in the beamformer derivations.

Figure 2.3 describes the signal model used throughout the derivations. A small acoustic point source located at $\mathbf{r_s} = (x_s, z_s)$ produces a pressure field propagating outward spherically toward

a linear array. The pressure field p at point $\mathbf{r}$ decays as a function of the distance from the source (Salgaonkar et al., 2009),

$$p(\mathbf{r}, t) = \frac{p_0(t)}{4\pi|\mathbf{r_s} - \mathbf{r}|} \tag{2.9}$$

where p_0 is the initial source pressure.

The source energy is given by integrating the squared source pressure over a time interval, T, and scaling by the medium's acoustic impedance, which we denote in its expanded form ρc (density by speed of sound) instead of Z to avoid confusion with the Cartesian z-axis (Coviello et al., 2015).

$$E_s = \frac{1}{4\pi\rho c}\int_T |p_0(t)|^2 dt \tag{2.10}$$

The goal of passive beamforming is to find this source energy while considering the decay of the pressure field through scaling factors.

The four beamformers below model the M-element linear array elements as omnidirectional point receivers. As such, the pressure signal incident on an element m of the linear array located at position $\mathbf{r_m}$ after propagating through a medium with speed of sound c is given by

$$p_m(t) = p(\mathbf{r_m}, \mathbf{t} + |\mathbf{r_m} - \mathbf{r_s}|/\mathbf{c}) = \frac{p_o(t + |\mathbf{r_m} - \mathbf{r_s}|/c)}{4\pi|\mathbf{r_m} - \mathbf{r_s}|/c}. \tag{2.11}$$

Since the true location and energy of the source, $\mathbf{r_s}$ is unknown, the goal of the beamformers is to produce an image of the energy at different pixel locations, denoted $E(\mathbf{r})$, for the users to localize and quantify the source given $p_m(t)$ measured by an array.

Time-domain Delay-and-Sum

Using the above signal model, we can derive an expression for the image E_{TDAS} using the delay-and-sum principle. Examining Equation 2.11 for the general point $\mathbf{r}$, we first steer each element to the point of interest by time-shifting the signal by the one-way propagation time to the point, $\tau_m(\mathbf{r}) = |\mathbf{r_m} - \mathbf{r}|/c$ and scaling by the propagation distance $d_m(\mathbf{r}) = |\mathbf{r_m} - \mathbf{r}|$ to obtain

$$\tilde{p}_m(\mathbf{r}) = 4\pi d_m(\mathbf{r}) p_m(t + \tau_m(\mathbf{r})). \tag{2.12}$$

To extract the energy, we perform a coherent sum over all the elements, divide by the number of elements, then square and integrate the resultant over a time interval T.

$$\begin{aligned}\tilde{E}(\mathbf{r}) &= \frac{1}{4\pi M^2 \rho c} \int_{t_0}^{t_0+T} \left| 4\pi \sum_{m=1}^{M} d_m(\mathbf{r}) p_m(t + \tau_m(\mathbf{r})) \right|^2 dt \\ &= \frac{4\pi}{M^2 \rho c} \int_{t_0}^{t_0+T} \left| \sum_{m=1}^{M} d_m(\mathbf{r}) p_m(t + \tau_m(\mathbf{r})) \right|^2 dt\end{aligned} \tag{2.13}$$

If the location $\mathbf{r} = \mathbf{r}_s$, then the steered signals will be in phase and sum constructively. Otherwise, the signals will be out of phase and sum destructively.

As pointed out by (Haworth et al., 2017), this operation alone produces a DC bias in the measured energy. We subtract the incoherent sum with the same scaling factors to remove this DC bias to obtain the continuous-time TDAS beamformer.

$$\begin{aligned}E_{TDAS}(\mathbf{r}) = &\frac{4\pi}{M^2 \rho c} \int_{t_0}^{t_0+T} \left| \sum_{m=1}^{M} d_m(\mathbf{r}) p_m(t + \tau_m(\mathbf{r})) \right|^2 dt \\ &- \frac{4\pi}{M^2 \rho c} \int_{t_0}^{t_0+T} \left[\sum_{m=1}^{M} |d_m(\mathbf{r}) p_m(t + \tau_m(\mathbf{r}))|^2 \right] dt\end{aligned} \tag{2.14}$$

Discretizing Equation 2.14, we note that the signal p_m is sampled at sampling interval Δt with corresponding sampling frequency $f_s = 1/\Delta t$ at sample points n ranging from 1 to $N = \text{floor}(T/\Delta t)$. Accordingly, the time delay τ_m becomes sample delay $n_m = \text{floor}(\tau_m/\Delta t) + 1$ so the steered signal $p_m(t + \tau_m(\mathbf{r}))$ becomes $p_m[n + n_m(\mathbf{r})]$. Thus, the discrete-time TDAS beamformer is given by

$$\begin{aligned}E_{TDAS}(\mathbf{r}) = &\frac{4\pi}{M^2 \rho c f_s} \left\{ \sum_{n=1}^{N} \left| \sum_{m=1}^{M} d_m(\mathbf{r}) p_m[n + n_m(\mathbf{r})] \right|^2 \right. \\ &\left. - \sum_{n=1}^{N} \left[\sum_{m=1}^{M} |d_m(\mathbf{r}) p_m[n + n_m(\mathbf{r})]|^2 \right] \right\}.\end{aligned} \tag{2.15}$$

To reduce the numerical error caused by the floor operator, the RF data can be optionally upsampled prior to computing the sample delays.

Frequency-domain Delay-and-Sum

The FDAS beamformer performs the same operations as TDAS but in the frequency domain via Fourier transform. This is possible due to the coherent summation being a linear operation. The

following derivation modifies the one in (Haworth et al., 2017) to include the spherical spreading compensation model derived above.

The Fourier transform results in $p_m(t) \leftrightarrow P_m(f)$ whose units are Pa and Pa·s, respectively:

$$P_m(f) = \int_0^T p_m(t) e^{-j2\pi ft} dt \tag{2.16}$$

We can use a finite time window here if we assume the whole cavitation signal is present in the time window $t = [0, T]$ and zero everywhere else. According to the time-shift property of the Fourier transform, applying the element-steering time-delay τ_m is equivalent to multiplying the Fourier transform by a complex exponential:

$$p_m(t + \tau_m) \leftrightarrow e^{j2\pi f\tau_m} \cdot P_m(f) \tag{2.17}$$

Similar to the time-domain case, we then sum over all the elements and compensate for the distance to the pixel, yielding

$$\tilde{P}_m(\mathbf{r}, f) = 4\pi \sum_{m=1}^{M} d_m(\mathbf{r}) \cdot e^{j2\pi f\tau_m} \cdot P_m(f). \tag{2.18}$$

To obtain the energy at the pixel, we apply Parseval's theorem to Equation 2.13 which equates the signal energy from the time domain to that in the frequency domain by a factor of $1/N$, so that

$$\tilde{E}(\mathbf{r}) = \frac{4\pi}{M^2 N \rho c} \int_{-\infty}^{\infty} \left| \sum_{m=1}^{M} d_m(\mathbf{r}) e^{j2\pi f\tau_m} P_m(f) \right|^2 df. \tag{2.19}$$

With the removal of DC energy, this becomes

$$\begin{aligned} E_{FDAS}(\mathbf{r}) = &\frac{4\pi}{M^2 N \rho c} \int_{-\infty}^{\infty} \left| \sum_{m=1}^{M} d_m(\mathbf{r}) e^{j2\pi f\tau_m} P_m(f) \right|^2 df \\ &- \frac{4\pi}{M^2 N \rho c} \int_{-\infty}^{\infty} \sum_{m=1}^{M} \left| d_m(\mathbf{r}) P_m(f) \right|^2 df. \end{aligned} \tag{2.20}$$

Note that the square of the complex exponential that would be in the second term has a magnitude of 1.

To reexpress Equation 2.20 in its discrete form, both the time and frequency domain operations have to be discretized. The continuous-time, continuous-frequency Fourier transform (CFT) and the discrete-time, discrete-frequency Fourier transform (DFT) are defined as follows, where k is

the discrete variable for the frequency domain.

$$P(f) = \mathcal{F}\{p(t)\} = \int_{-\infty}^{\infty} p(t) \cdot e^{-j2\pi ft} dt \tag{2.21}$$

$$P[k] = \mathcal{F}\{p[n]\} = \sum_{n=1}^{N} p[n] \cdot e^{-j2\pi kn/N} \tag{2.22}$$

$$P_{eq}[k] = \frac{1}{f_s} P[k] \tag{2.23}$$

As shown in the second line, the DFT lacks a dt term, so to ensure equivalence between the two, an extra $\Delta t = 1/f_s$ scaling factor is required to ensure that the units stay equivalent between the two methods (Pa·s) (Haworth et al., 2017). With the DFT equivalence established and taking $df = \Delta f = f_s/N$, Equation 2.20 becomes

$$\begin{aligned} E_{FDAS}(\mathbf{r}) = \frac{4\pi}{M^2 N \rho c f_s} \Bigg\{ \sum_{n=0}^{N-1} \left| \sum_{m=1}^{M} d_m(\mathbf{r}) e^{j2\pi k n_m/N} P_m[k] \right|^2 \\ - \sum_{n=0}^{N-1} \sum_{m=1}^{M} |d_m(\mathbf{r}) P_m[k]|^2 \Bigg\}. \end{aligned} \tag{2.24}$$

Angular Spectrum

In contrast to the delay-and-sum beamformers, the angular spectrum approach operates in the Fourier domain for both time and spatial frequencies (Cobbold, 2006). For 2D PCM, it beamforms one image depth line at a time with a time- and spatial-Fourier domain transfer function to propagate the signals incident on the array back to their origin location. We will consider the beamforming of a line with the same lateral spatial limits as the array aperture. For a given depth z to be beamformed from the aperture, the continuous-time and continuous-space transfer function H to be applied to each temporal frequency f and spatial frequency u is

$$H(f, u; z) = exp\{jzk'_z\} = exp\left\{jz\sqrt{k'(f)^2 - k'_x(u)^2}\right\}, \tag{2.25}$$

where we denote the spatial and temporal wave numbers $k'(f)$ and $k'_x(u)$ (not to be confused with the discrete frequency index, k). The spatial and temporal wave numbers are defined based on the frequency limits of the 2D-DFT performed on each dimension. The continuous form is as follows:

$$k'(f) = \frac{2\pi}{\lambda} = \frac{2\pi f}{c} \tag{2.26}$$

$$k'_x(u) = \frac{2\pi}{\lambda_x} = 2\pi u \tag{2.27}$$

Since the RF data is already discretized in the spatial dimension due to the finite number of elements, it will be easier to define the values of f and u in terms of their discrete equivalents, k and v. We will consider the discrete-time and discrete-space matrix representation of the pressure incident on the array in the frequency domains:

$$P[v,k] = \mathcal{F}_{2D}\{p[m,n]\} = \sum_{m=0}^{M-1}\sum_{n=0}^{N-1} p[v,k]\cdot e^{-j2\pi kn/N}\cdot e^{-j2\pi vm/M} \tag{2.28}$$

with $v = 0, 1, ..., M-1$ and $k = 0, 1, ..., N-1$ as before, with frequency resolution $\Delta f = f_s/N$ and $\Delta u = \frac{1}{M\Delta x}$ where Δx is the array pitch. The discrete functions of $k'(f)$ and $k'_x(u)$ are thus

$$\begin{aligned} k'[k] &= \frac{2\pi k f_s}{Nc}, & k &= 0, 1, ..., N-1 \\ k'_x[v] &= \frac{2\pi v}{M\Delta x}, & v &= 0, 1, ..., M-1 \end{aligned}$$

Substituting those into Equation 2.25, we obtain the discrete version of the transfer function

$$H[v,k;z] = \exp\left\{jz\sqrt{\left(\frac{2\pi k f_s}{Nc}\right)^2 - \left(\frac{2\pi v}{M\Delta x}\right)^2}\right\}. \tag{2.29}$$

To obtain the beamformed line $\tilde{P}[m,k;z]$, we apply the transfer function element-wise to $P[v,k]$ and perform the inverse DFT in the spatial domain only.

$$\tilde{P}[m,k;z] = \mathcal{F}_v^{-1}\left\{P[v,k]\odot H[v,k]\right\} \tag{2.30}$$

$$= \frac{1}{M}\sum_{v=0}^{M-1} P[v,k]\odot \exp\left\{jz\sqrt{\left(\frac{2\pi k f_s}{Nc}\right)^2 - \left(\frac{2\pi v}{M\Delta x}\right)^2}\right\} \tag{2.31}$$

To compute the total energy, we multiply the expression for $\tilde{P}[m,k;z]$ by the distance from the origin to compute the spherical spreading compensation, then square and sum over the temporal frequencies k as before.

$$E_{AS}(x;z) = \frac{4\pi d(x,z)^2}{MN\rho c f_s}\sum_{k=0}^{N-1}\left|\mathcal{F}_v^{-1}\left\{P[v,k]\odot H[v,k]\right\}\right|^2 \tag{2.32}$$

This produces an image whose x-dimension is constrained by the array aperture dimensions and whose x-resolution is defined by the spatial inverse DFT, while the image grid in the z-dimension can be defined just as in the delay-and-sum beamformers. Thus, for the imaging grid to match the coordinates of the other beamformers, two strategies are possible. First, the inverse spatial DFT can be zero-padded to increase the resolution of the final image grid. Second, we can crop and interpolate the output E_{AS} to the desired image coordinates.

Robust Capon Beamformer

The Robust Capon beamformer (RCB) (Stoica, Wang, & Li, 2003) is an adaptive optimal beamformer that implements diagonal loading (J. Li, Stoica, & Wang, 2003) to suppress interference from other sources and reduce the sensitivity of the beamformer to errors in array calibration. In this section, the continuous-time implementation from (Coviello et al., 2015) is first presented (though frequency-domain implementations are also possible (Polichetti et al., 2021)), followed by the discretization steps as previously shown.

We previously defined the expressions for the element-specific time delays $\tau_m(\mathbf{r})$ and $n_m(\mathbf{r})$ in the TDAS derivation. RCB expands on the TDAS beamformer. Coviello et al. estimate the sample covariance matrix $\mathbf{R}_s$ (MxM) from the finite-duration pre-steered pressure signals (i.e. where the element-specific time delays are already applied), which we define as $\tilde{\mathbf{p}}(t) = [p_1(t+\tau_1), p_2(t+\tau_2), ..., p_M(t+\tau_M)]^T$, $\tilde{\mathbf{p}}[n] = [p_1[n+n_1], p_2[n+n_2], ..., p_M[n+n_M]]^T$ (MxN matrix) as follows

$$\mathbf{R}_s = \int_T \tilde{\mathbf{p}}(t)\tilde{\mathbf{p}}^H(t)dt. \tag{2.33}$$

$$\mathbf{R}_s = \frac{1}{f_s}\tilde{\mathbf{p}}[m,n]\tilde{\mathbf{p}}^H[m,n]. \tag{2.34}$$

In the minimum variance (Capon) problem, the goal is to compute a normalized weight vector $\mathbf{w}$ to apply to the signal of each element that solves

$$\min_{\mathbf{w}} \quad \mathbf{w}^T\mathbf{R}_s\mathbf{w} \quad \text{subject to} \quad \mathbf{w^T 1}_M = 1 \tag{2.35}$$

where $\mathbf{1}_M$ denotes a M-length vector of ones. This results in the analytical solution $\hat{\mathbf{w}} = \frac{\mathbf{R}_s^{-1}\mathbf{1}_M}{\mathbf{1}_M^T\mathbf{R}_s^{-1}\mathbf{1}_M}$ and expression for cavitation dose (energy)

$$E_{MV}(\mathbf{r}) = \frac{4\pi}{M\rho c}\frac{1}{\mathbf{1}_M^T\mathbf{R}_s^{-1}\mathbf{1_M}}. \tag{2.36}$$

This algorithm is known to be sensitive to uncertainties in the array steering vector (presumed to be $\mathbf{1}_M$, but could in practice be different due to imperfect calibration and/or dead elements), finite sampling errors in $\mathbf{R_s}$ (Besson, 2018), white noise, and interference from other sources (Coviello et al., 2015) due to the matrix inversion requirement.

For RCB, Stoica et al. (2003) propose a diagonal loading extension as a way to mitigate some of these issues. They propose the following constrained optimization problem to be solved by the

method of Lagrange multipliers:

$$\min_{\mathbf{a}} \quad \mathbf{a}^T \mathbf{R}_s^{-1} \mathbf{a} \quad \text{subject to} \quad \|\mathbf{a} - \mathbf{1}_M\|^2 = \varepsilon. \tag{2.37}$$

The above optimization problem has the analytical optimal solution $\hat{\mathbf{a}} = \mathbf{1}_M - (\mathbf{I} + \lambda \mathbf{R}_s)^{-1} \mathbf{1}_M$, where the Lagrange multiplier $\lambda \geq 0$ determines the amount of diagonal loading. Coviello et al. (2015) re-express the optimal solution in terms of the eigenvalue decomposition of $\mathbf{R}_s = \mathbf{U}\mathbf{V}\mathbf{U}^T$

$$\hat{\mathbf{a}} = \mathbf{1}_M - \mathbf{U}(\mathbf{I} + \lambda \mathbf{V})^{-1} \mathbf{U}^H \mathbf{1}_M \tag{2.38}$$

where $\mathbf{U}$ is the matrix of eigenvectors and $\mathbf{V}$ is a diagonal matrix containing the eigenvalues. The value of λ is then determined by substituting the above equation into and solving the constraint equation

$$\begin{aligned} g(\lambda) &\triangleq \|\hat{\mathbf{a}} - \mathbf{1_M}\|^2 \\ &= \|(\mathbf{I} + \lambda \mathbf{R}_s)^{-1} \mathbf{1}_M\|^2 = \varepsilon. \end{aligned} \tag{2.39}$$

With the knowledge that $\mathbf{R}_s$ should be positive semidefinite, Stoica et al. (2003) note that $g(\lambda)$ is a monotonically decreasing function and λ is bounded by quantities determined by the eigenvalues ($\mathbf{V}$) of $\mathbf{R}_s$ (omitted here for brevity). This means that the value for λ is solvable with a few iterations of a numerical function-solving method such as Newton's method. Since the optimization problem may not preserve the magnitude of the steering vector ($\|\mathbf{1}_M\|^2 = M$), the resulting energy must be scaled by $\|\hat{\mathbf{a}}\|^2/M$ (Stoica et al., 2003).

Given the above, the energy at the resultant beamformed point, with the spherical-spreading compensation (diagonal matrix of distances $\mathbf{D}(\mathbf{r}) = \text{diag}(\mathbf{d}(\mathbf{r}))$ and other scaling factors, is

$$E_{RCB}(\mathbf{r}) = \frac{4\pi}{f_s \rho c} \frac{\|\hat{\mathbf{a}}\|^2}{M} \frac{1}{\hat{\mathbf{a}}^H \mathbf{D}^{-1} \mathbf{U}\mathbf{V}(\lambda^{-2} + 2\lambda^{-1}\mathbf{V} + \mathbf{V}^2)^{-1} \mathbf{U}^H \mathbf{D}^{-1} \hat{\mathbf{a}}} \tag{2.40}$$

Note that because of the interference suppression and tunability of the beamformer, removal of the DC component that was performed for TDAS and FDAS is not required in RCB.

2.5 Chapter Summary

The fundamentals of microbubble cavitation, their acoustic responses, and acoustic measurement methods are discussed. Passive imaging of cavitation allows for the computation of acoustic energy released by cavitation sources from within the imaging plane. A review of the literature reveals

a gap in cavitation dose standardization, which can be addressed by comparing the absolute dose accuracy of PCM algorithms with an independent reference measurement. The principles of delay-and-sum beamforming originally used in active, pulse-echo imaging can be adapted for the passive reception of cavitation emissions. Finally, the derivation of cavitation dose for four passive beamformers is presented with consideration of the effects of both spherical spreading and discrete processing.

Chapter 3

Method and Platform for Evaluating Passive Cavitation Mapping Algorithms

3.1 Chapter Overview

This Chapter presents the experimental and processing methods for the proposed algorithm comparison. Section 3.2 illustrates the design and characterization of the cavitation exposure platform for codetection of cavitation activity. Section 3.3 details the methods used to calibrate the ultrasound imaging probe for quantitative PCM. Finally, Section 3.4 describes the processing, comparative analysis, and beamforming implementation details used to compare the different algorithms.

3.2 Design of a Cavitation Exposure Platform and Tested Parameters

To test the two hypotheses presented in Chapter 1, a cavitation testbed was designed that would allow for the controlled exposure of MBs to a focused ultrasound source (Figure 3.1) and whose cavitation emissions can be received simultaneously by both a diagnostic ultrasound imaging array (for PCM) and a PCD. The cavitation testbed assembly consists of a submersible platform

machined out of aluminum designed to hold the FUS transducer and PCD at specific positions from the cavitation target. A 0.6 mm inner diameter silicone tube (0.2 mm wall thickness) with flowing microbubbles was chosen as the cavitation target. This tube was selected as its relatively small diameter would allow us to assess the spatial localization accuracy of PCM algorithms. The tube was held within the focal region of a FUS transducer (aperture 89 mm, focal length 52.5 mm) by notches in a custom conic tube holder 3D printed in polylactic acid (PLA) polymer. The location of the maximum within the focal region was verified by measuring the pressure field of the FUS transducer within the exposure platform (Figure 3.1 inset), which shows that the tube's transverse cross-section fits within and longitudinally spans the -3 dB lateral beamwidth (1.50 mm nominal, 1.60 mm measured) for a total excited volume of 0.45 mm^3. The field profile measurements also confirmed that the conic tube holder did not disrupt the FUS transducer's pressure field development.

Cavitation emissions from the flowing microbubbles were detected on the centre 64 channels of a L14-5 array (Ultrasonix, 128 channels, 0.3048 mm element pitch, 5 mm element height) acquired by a US4R-Lite scanner (US4US) positioned approximately 50 mm away by an external retort stand. In this geometry, the modest elevation focusing of the array elements allows it to capture cavitation activity from the entire target volume. Reference PCD measurements were simultaneously captured with a 400-μm diameter aperture capsule hydrophone (ONDA Corp., HGL-400) positioned 5.5 mm from the centre of the tube using the machined fixture. The proximity of the hydrophone to the tube was required to boost the signal level above the hydrophone's noise floor. At this distance, the target area spans a maximum of 16.6°, within the hydrophone's nominal 30° acceptance angle. As shown, the depth axes of the hydrophone and linear array were positioned at 90° and 45°, respectively, to the HIFU transmission axis to prevent direct insonation from the FUS transducer.

Prior to data acquisition for each experiment, the silicone tube was filled with air and a 0° plane-wave acquisition was obtained for later B-mode extraction of the tube position. A complete list of the exposure parameters for this experiment is shown in Table 3.1. Liposome solution (9:1 DSPC:DSPE-PEG2000, 2 mg/mL) prepared with a lipid-film hydration method (Has & Sunthar, 2020) was shaken under a decafluorobutane gas headspace and diluted 1:40 in deionized water to produce a concentration on the order of 10^8 MBs/mL. A syringe of diluted microbubble suspension attached to the silicone tube was placed in a syringe pump operating at

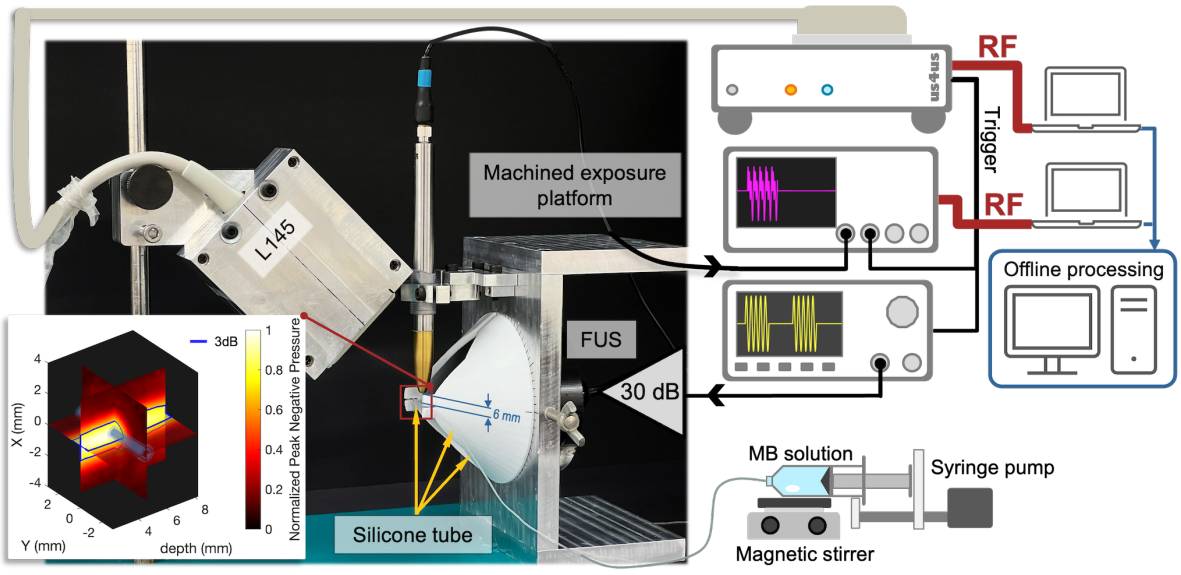


Figure 3.1: Cavitation exposure platform with PCM-PCD codetection. Inset: Field profile measurements of the FUS transducer with 6dB beamwidth in blue and the position of the silicone tube shown in light blue.

a flow rate of 1.5 mL/min. The platform was immersed in a tank of off-gassed water at 22°C, corresponding to a speed of sound of approximately 1490 m/s (Wilson, 1959). The ultrasound excitation pulses produced by the FUS transducer were driven by a Siglent function generator (SDG2042X) output to a 30 dB amplifier and impedance matching circuit. The pulses consisted of a 1 MHz 20-cycle sinusoidal waveform with peak negative pressures ranging from 0 to 1000 kPa in intervals of 50 kPa. Signals from the capsule hydrophone, which was connected to a 20 dB preamplifier (Onda Corp., AHS-2010-100), were digitized with a Rigol digital oscilloscope at a sample rate of 500 MHz and later lowpass filtered and downsampled to 32.5 MHz to match the scanner's sampling rate. A sync signal from the us4R-Lite scanner was used to trigger the signal generator pulse and the oscilloscope acquisition. For each experimental pressure, 700 frames were captured from the scanner for PCM, while 50 acquisitions were captured by the oscilloscope for PCD over approximately 30 seconds. This procedure was repeated three times (experiments later labelled N1-N3). In between repetitions, the array, tube, and hydrophone were disassembled and reassembled to induce some variability in the positioning.

Table 3.1: Exposure Platform Experimental Parameters

Parameter	**Value**
Imaging Parameters	
Ultrasound Platform	us4us us4R-Lite
Probe	Ultrasonix L14-5
Number of elements	64 (128 available)
Array element pitch	0.3048 mm
Array element height	5 mm
Sampling frequency	32.5 MHz
Number of frames per dataset	700 frames
Analog gain	40 dB
Distance to cavitation	50-60 mm
Hydrophone Parameters	
Hydrophone	Onda HGL-400
Preamplifier	Onda AHS-2010-100 (20 dB)
Active element diameter	400 μm
Oscilloscope	Rigol DS1104Z
Sampling frequency	500 MHz
Number of waveforms per dataset	50 frames
Exposure Parameters	
Signal generator	Siglent SDG2042X
Amplifier	Benthowave Instrument Inc. BII-5121 (30 dB)
Impedance Matching	Benthowave Insturment Inc. BII-6010
FUS transducer	Benthowave Instrument Inc. BII-7653-1000
Peak negative pressure	0:100:1000 kPa
Pulse length	20 cycles
Pulse repetition interval	50 ms
Microbubble concentration	$\approx$ 2.8x10^8 MB/mL
Tube inner/outer diameter	0.6 mm/1 mm
Flow rate	1.5 mL/min
Average flow speed	89 mm/s

3.3 Ultrasound Array Calibration Methods

The frequency-dependent receive sensitivity magnitude response of the PCM array, required to convert from units of volts to pressure, was determined through a frequency sweep method depicted in Figure 3.2. A $\frac{1}{4}$-inch piston transducer (Olympus, 5 MHz centre frequency) was used to transmit 30-cycle sinusoidal pulses at fixed frequencies from 2.1 to 10.5 MHz in steps of 0.1 MHz generated by an arbitrary function generator (Siglent SDG2042X). Input amplitudes of 5 V_{pp} or 10 V_{pp} were chosen to ensure adequate signal levels on the hydrophone and prevent saturation of the linear array in its main bandwidth. In the first set of acquisitions (Figure 3.2A), a capsule hydrophone with 400-μm active diameter (Onda Corp., HGL-400) was aligned with the centre of the source transducer's field profile by a 3-axis motion stage (IntelLiDrives Ltd.) at a distance of 58 mm from the piston transducer. The 3-axis motion stage has a minimum step size of 4 μm and has previously been used in the field profile analysis of other ultrasound probes (Maffett et al., 2022). The hydrophone was then scanned over the element height ($h = 5$mm) in steps of 0.04 mm, and pressure waveforms were acquired at a 50 MHz sampling frequency. The waveforms were median filtered over five acquisitions at each point to reduce the impact of electrical noise during the experiment. To calculate the peak negative voltage for each point at each frequency, the signal was bandpass filtered to the centre frequency $\pm$ 0.5 MHz. The median of the 20 largest negative peaks from the RF data was then taken before applying the hydrophone's sensitivity provided by the manufacturer. Examples of the resulting field profiles at 3, 6.5, and 10 MHz are shown in the inset (Figure 3.1). To obtain the final hydrophone pressure $P_H(f)$, the peak negative pressure magnitude was spatially averaged (denoted by $\langle\cdot\rangle$) over all the readings in the 5 mm element height (y) to account for the spatial averaging of the array element (Equation 3.1).

$$\begin{aligned} |P_H(f,y)| &= \frac{|V_H(f,y)|}{M_H(f)} \\ \langle |P_H(f)| \rangle &= \frac{1}{h}\int_y \frac{|V_H(f,y)|}{M_H(f)} dy \end{aligned} \tag{3.1}$$

In the second set of acquisitions (Figure 3.2B), the hydrophone was replaced with the linear array. It was aligned visually to the same guide 58 mm from the piston transducer and centred over its field profile. The piston transducer was scanned over the centre 64 elements, and 50 frames were extracted from each array element at each frequency to determine the mean peak negative voltage ($V_{A,m}$ where subscripts A denotes Array and m denotes element number). Each

element's peak negative voltage was divided by the hydrophone's spatially averaged peak negative pressure to obtain its receive sensitivity frequency response from 2.1 to 10.5 MHz. The calibration was repeated in triplicate. The mean frequency response of the three experiments was smoothed with MATLAB's `smooth` function (with a linear model) before its use in the receive sensitivity compensation of experimental data.

$$P_H(f) = \frac{\overline{V_H}(f)}{M_H(f)} \qquad M_{A,m}(f) = \frac{V_{A,m}(f)}{P_H(f)}$$

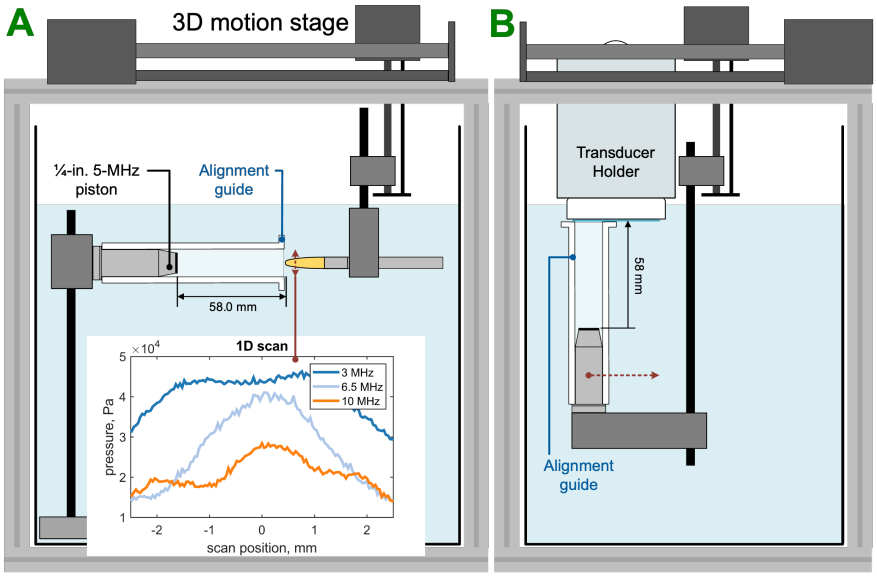


Figure 3.2: L14-5 element sensitivity calibration method. A) First set of acquisitions where the hydrophone scans over the element height at different frequencies to obtain the reference pressure, $P_H(f)$. B) Second set of acquisitions where the source transducer is scanned over the array aperture to obtain the voltage response $V_{A,m}$, which is then converted to a sensitivity value, $M_{A,m}$

3.4 Ultrasound Imaging, Preprocessing, and Beamforming

3.4.1 Beamformer Implementation Details

Table 3.2 summarizes the parameters used during beamforming. Spatial zero-padding and windowing for the angular spectrum (AS) beamformer were necessary to reduce the effect of wraparound errors caused by the low spatial sampling. The effect of the Tukey window was compensated by

dividing the result of Equation 2.32 by the mean squared value of the window (Haworth et al., 2017). The beamformers, which were implemented in MATLAB and accelerated with the builtin `gpuArray` function, processed data on a server with a Xeon E5-2699 v4 CPU, with a total of 768GB RAM and NVIDIA A4000 graphics card. The exact CPU and memory resources available at the time were not quantifiable due to the shared nature of the server.

Table 3.2: Beamforming Parameters

Parameter	Value
Image Dimensions	128 px x 128 px
Field of View	20 mm x 30 mm
Speed of Sound	1490 m/s
Beamformed Signal Length	1626 samples / 50 μs
Zero-padding (spatial)	AS - to 128 elements
Windowing (spatial)	AS - 64-tap Tukey window, 0.25 cosine fraction

3.4.2 Cavitation Mapping Signal Processing Pipeline

The following RF data preprocessing steps were identical for the PCD and PCM data. First, RF data were time-gated to a 50 μs window surrounding the cavitation signal and bandpass filtered to 2.7-10.7 MHz, representing signal from the 3rd to 10th harmonics. To convert the units to pressure, the RF data were first Fourier-transformed. Then, the receive sensitivity frequency response magnitude of each element (Figure 4.10) was interpolated and applied before inverse-Fourier transforming to obtain the calibrated time-domain signal. All data were bandpass filtered to the frequencies of interest before beamforming to ensure equivalence between time- and frequency-domain beamformers. For the PCD data specifically, since significant electrical noise was present, the frequency spectrum of noise taken from the end-region of the signal (outside the 50-μs window) was subtracted from the cavitation signal spectrum before log compression, frequency band analysis, and cavitation dose calculation. Analysis of different frequency bands was accomplished by Fourier-transforming the pressure RF data and applying a frequency-domain mask with a bandwidth of 0.1 MHz to isolate or eliminate specific frequency components. The frequency bands of interest included the narrowband harmonic and ultraharmonic frequencies

from 3 to 10 MHz, the sum of all harmonic frequencies, the sum of all ultraharmonic frequencies, and the sum of all the frequencies in between the harmonic and ultraharmonic frequencies (broadband) from 3 to 10 MHz, for a total of 18 sets of frequency bands. After bandpass filtering, the same datasets were Hilbert transformed and passed into the four beamformers described in Section 2.4.2.

Using the resulting beamformed cavitation maps, the cavitation dose within the tube was calculated as follows. First, the tube position was determined from the B-mode images by finding the axial and lateral position of the peak reflection, which would correspond with the top of the tube lumen that forms an echogenic tube-air boundary. With the knowledge of the lumen diameter of 0.6 mm, the coordinates of the centre of the tube could be calculated, and the corresponding PCM pixels within the lumen could be identified. The PCM-derived cavitation dose was calculated as the mean energy from the pixels within the tube.

3.4.3 Robust Capon Beamformer Tuning

As mentioned in Chapter 2, Section 2.4, the Robust Capon beamformer utilizes an empirically determined parameter, ε, for interference rejection. In this experiment, the optimal value of ε was manually determined through pilot beamforming of 5 frames from each data set. The maximum pixel values were compared to those obtained from the FDAS beamformer. As ε increases, the ratio (RCB/FDAS) between the two beamformers' maximum pixels increases monotonically, and the optimal value is interpolated. As shown in the processing example in Figure 3.3, the optimal ε value for the harmonics band, at 600 kPa, in experiment N1, would be approximately 1. The results of the tuning are presented in the next Chapter.

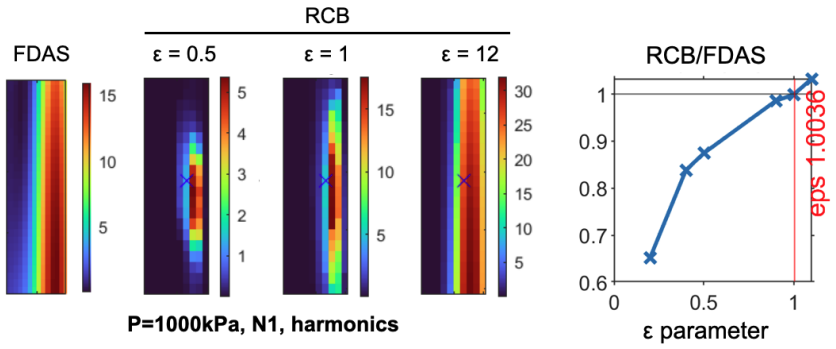


Figure 3.3: RCB tuning example. Comparison of FDAS and RCB with 3 different values of ε for experiment N1, pressure at 1000 kPa and beamformed over the harmonic frequency bands (reduced 2 mm x 8 mm field of view). Colourbar units in nJ. (Far right) Testing different estimate ratios (RCB/FDAS) showed that the optimal value was 1.0.

Chapter 4

Experimental Results of the Passive Cavitation Mapping Evaluations

4.1 Chapter Overview

This chapter presents the results of the cavitation exposure experiment and analysis described in the previous chapter. First, an overview of the beamforming results is provided in Section 4.2. Second, the magnitudes of the cavitation dose computed by each algorithm and how they correspond to cavitation dynamics are highlighted in Section 4.3. Next, Section 4.4 analyzes the discrepancies between the cavitation doses computed by each beamformer. This is followed by an assessment of the spatial localization accuracy of the algorithms, given by the location of each map's maximum pixel, in Section 4.5, and an analysis of each algorithm's beam area in Section 4.6. After, the output of the reference hydrophone used as a passive cavitation detector is presented in Section 4.7. Finally, the receive sensitivity of the L14-5 array and pressure field profile of the FUS excitation transducer are reported in Section 4.8.

4.2 Overview of Beamforming Results

4.2.1 Summary B-mode and PCM Overlay

Figure 4.1 shows the B-mode images with overlaid PCM plots for each beamformer (columns) in each experiment (rows N1-3) in the 1000 kPa case over the harmonic frequencies. The red circles

indicate the true tube lumen locations. For experiments N1 and N3, the tube lumen was located approximately on-axis at depths between 53-57 mm. In experiment N2, the lumen was positioned 5.54 mm right of centre at the same approximate depth. As shown, the PCM-estimated tube location (indicated by the white circle) is generally deeper than the true location.

4.2.2 Effect of Tuning on RCB

An example of the results of the ε parameter tuning for RCB is shown in Figure 4.2. The effect of tuning on dose estimate and beam area are shown for three values of ε shown in Figure 4.2A. When $\varepsilon = 0.5$, RCB underestimates FDAS energy but has the smallest beam area, which contrasts with the $\varepsilon = 12$ case where both the beam area and dose estimate are much greater. In this case, the optimal value of ε that achieved the closest mean energy estimate to FDAS was 1. This parameter search was repeated for each experimental pressure from 400 kPa and above, as summarized in Figure 4.2B. The ε values determined for each frequency at 400 kPa were applied to pressures from 0-400 kPa. Overall, the distributions for the optimal parameter were wider for the narrow frequency bands (3-10 MHz) compared to the multi-frequency harmonic (H), ultraharmonic (UH) and broadband (BB) bands. The median ε value also increased with frequency and reduced signal level (which is not shown here).

4.3 PCM-Estimated Dose at Increasing Pressure

4.3.1 Overview

Figure 4.3 summarizes the PCM outputs of beamformers in the harmonic, ultraharmonic, and broadband frequency bands (A, B, and C, respectively) in response to increasing pressure in the first repetition of the experiment (N1). The first four columns provide a stacked visualization of the mean PCM maps derived from the four PCM algorithms – angular spectrum (AS), frequency-domain delay-and-sum (FDAS), time-domain delay-and-sum (TDAS) and Robust Capon beamformer (RCB) – at each tested pressure from 0 to 1000 kPa. Only the ¿50th percentile of pixel magnitudes from each map is plotted for ease of visualization. The black lines trace the location of the maximum pixel within each map, around which the cavitation dose is calculated for each experimental condition. The cavitation doses are plotted in Fig.4.3A-i, B-i and C-i, showing an

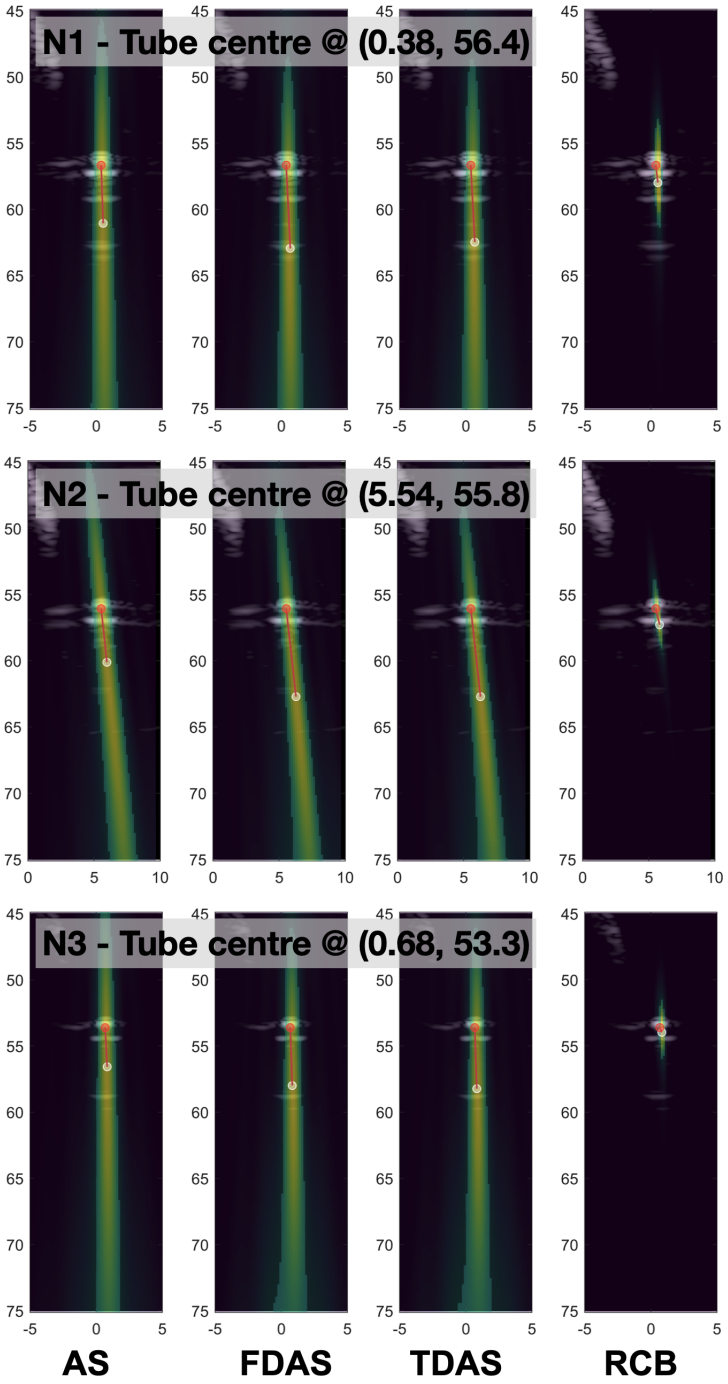


Figure 4.1: Example PCM plots obtained from the 1000 kPa dataset beamformed on the harmonic frequency bands for each experiment (N1-3). Actual tube positions determined from the B-mode image are stated (in mm) and overlaid as red circles, with lines out to the maximum pixels (white circles) in each PCM map.

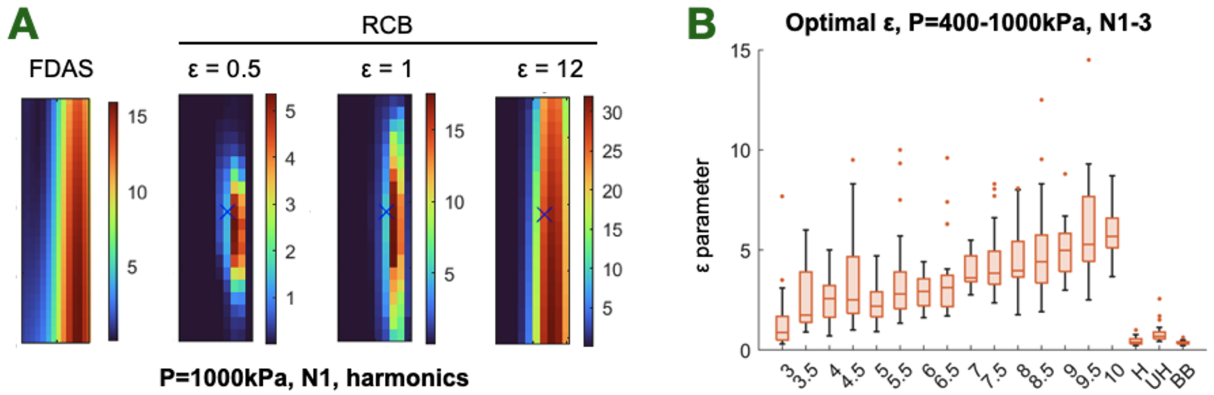


Figure 4.2: RCB tuning results. Summary plot of final tuned values of ε for each experimental condition for pressures 400 kPa and greater.

increasing trend as pressure increases for all frequency bands. (Analysis of Figure 4.3ABC-ii is conducted in Sections 4.5 and 4.6.)

4.3.2 Cavitation Dose Thresholds

Figure 4.4 presents the same dose vs. pressure plots as Figure 4.3ABC-i for experiments N1-3 along with the corresponding mean energy density spectra computed from the pre-beamformed RF data incident upon the PCM array. Using columns 1-3, we can identify the approximate pressure thresholds that coincide with the onset of cavitation in each frequency band, and cross-reference the increase in the dose with the appearance of their corresponding spectral features in the 4th column. In N1 and N3, the harmonics have an initial onset between 200-300 kPa, followed by a slight dip at 400 kPa, and an increase again at 500 kPa. In N2, there appears to be only an initial onset at 400-500 kPa. This is followed by an additional larger change in harmonic cavitation dose after 700 kPa and the start of a plateau is visible in N1 and N2. The shape of the broadband curves roughly follows the same trend as the harmonics, with an initial onset at 500 kPa and again at 700 kPa, but at a ten-fold smaller magnitude. A plateau of broadband dose is only seen in N2. Lastly, the onset of ultraharmonic components appears slightly at 500 kPa but has a more obvious onset after 800 kPa – this is also evident in the spectra shown in column 4.

Examining the doses computed by the beamformers in columns 1-3, the dose calculated by FDAS and TDAS follow each other almost exactly (the green curve, representing FDAS, is exactly

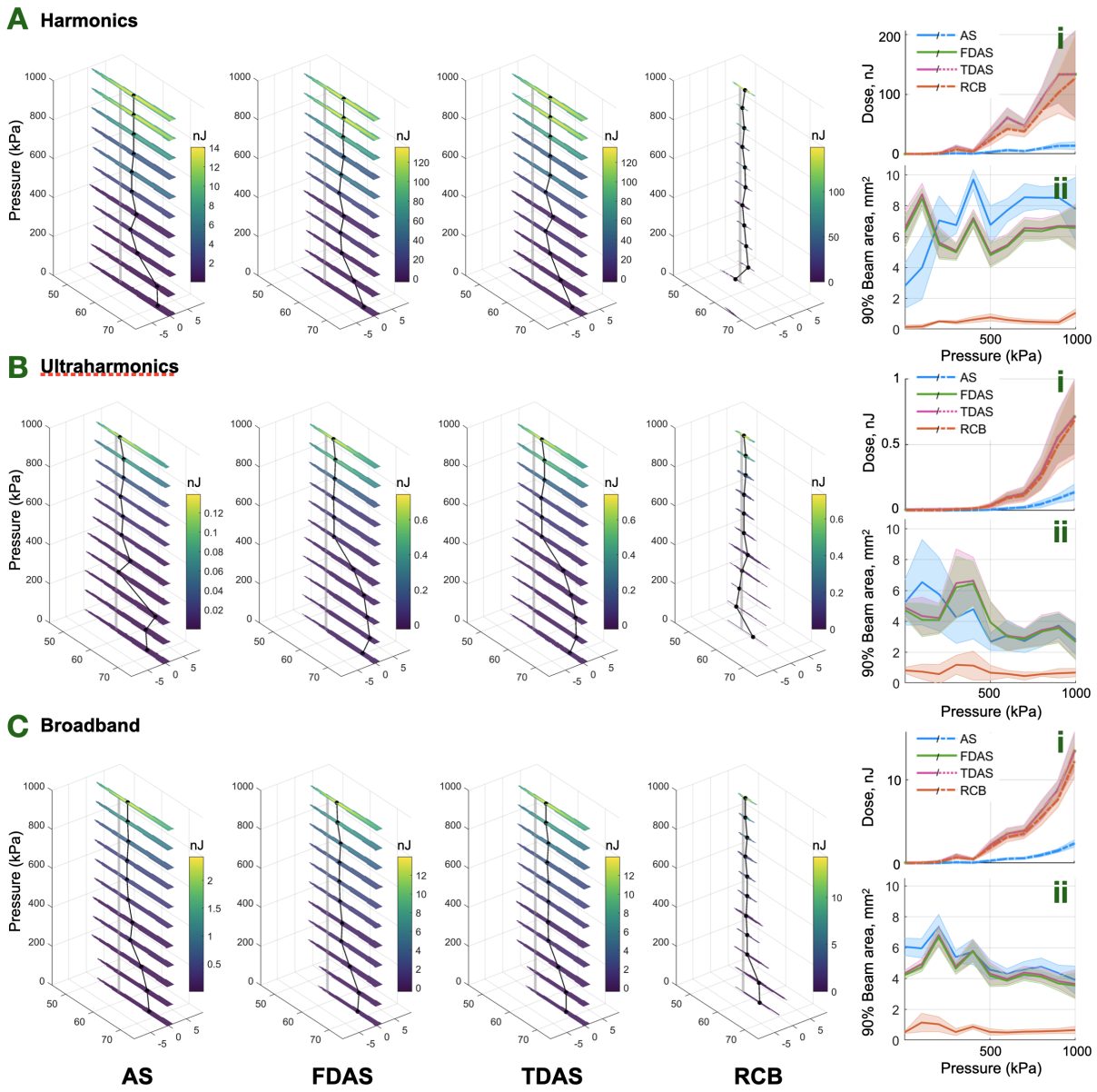


Figure 4.3: Summary of beamformer outputs against increasing pressure for A) harmonic, B) ultraharmonic, and C) broadband frequency bands, averaged over 15 acquisitions in experiment 1 (N1). Left to right: Stacked 2D cavitation maps from each beamformer – AS (angular spectrum), FDAS (frequency-domain delay-and-sum), TDAS (time-domain delay-and-sum), and RCB (Robust Capon Beamformer) – with increasing pressure (z-axis). Only the top 50 percentiles of pixels in each map, representing the 6dB beam area, are coloured. The colourmaps are based on the range of pixel values over all pressures for each beamformer. The gray cylinder passing through each map represents the true position of the silicone tube's lumen. The black line traces the location of the maximum pixel of each map. i): Cavitation dose computed around the maximum pixel for each beamformer plotted against input pressure. ii): Mean and std. dev. (shaded) beam area from the top 90th percentile of pixels in each map.

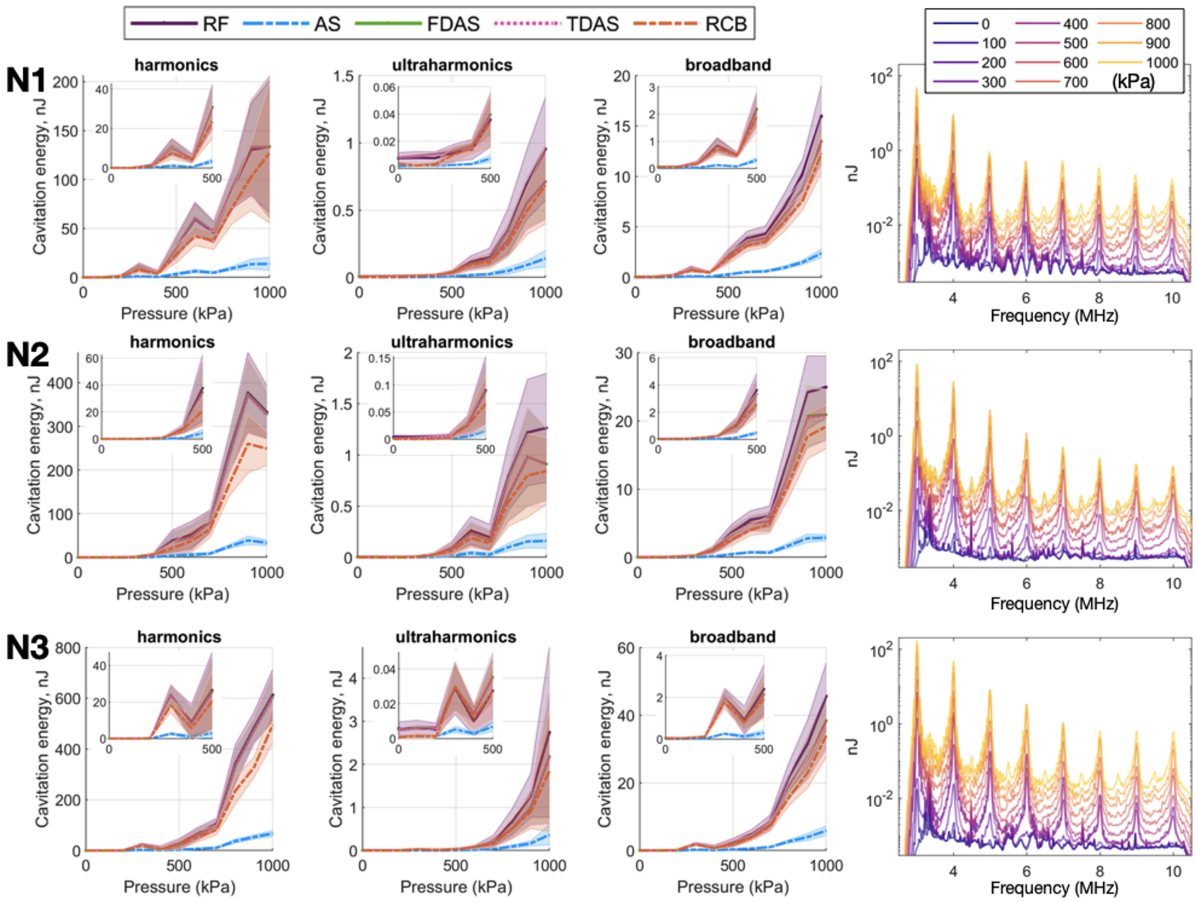


Figure 4.4: Cavitation dose computed by each beamformer and from raw RF data for each experiment (N1-3), analyzed in the harmonic, ultraharmonic, and broadband frequency bands, and the associated energy density spectra computed from the pre-beamformed RF data. Insets show a closer view from 0 to 500 kPa.

obscured by the pink curve, TDAS). The FDAS and TDAS beamformers closely follow the dose computed from the pre-beamformed RF data in the harmonic band but are lower than it in the ultraharmonic and broadband bands. The RCB-derived doses follow a similar trend to the DAS beamformers in all the frequency bands at slightly lower amplitude, but AS underestimates all the other methods. These trends also hold for the narrow frequency bands. For a complete picture of the cavitation dose against pressure for more frequency bands in each experiment, see Appendix A.1.2.

4.4 PCM-Estimated Dose Differences

To more easily compare the relative performance of PCM algorithms on dose estimation, pairwise (frame-to-frame) differences in the cavitation doses for each beamformer were taken relative to the output from FDAS (% diff re FDAS = $100\%(E_{test} - E_{FDAS})/E_{FDAS}$) as shown in Figure 4.5. In this analysis, only the experimental conditions above the cavitation thresholds identified in the previous section were included to exclude large % differences caused by near-zero dose values below the cavitation threshold. The raw difference plots from which these box plots are derived are shown in Appendix Section A.3.

In Figure 4.5A, the median pairwise signed % differences from the FDAS are plotted against the frequency bands (each frequency has n=45). From this analysis, a few trends are evident. First, TDAS practically has 0 difference from FDAS for all frequency bands. Second, as the narrow frequency band increases, the median signed percent difference of AS increases, but its absolute difference decreases, going from -90% at 3 MHz to -57% at 10 MHz. The variation in the median % difference (given by the size of the bar) is also relatively small within frequency bands, indicating little dependence on pressure. (See Appendix A.3 for more detailed difference plots that support this.) Third, there is considerable variation in the median % differences of RCB in the narrow frequency bands. However, the % differences are relatively closer to 0% and less variable for the harmonic, ultraharmonic, and broadband bands than the narrowband frequencies.

Whereas Figure 4.5A examines the median % difference over 15 frames, Figure 4.5B examines the interquartile range (IQR) of the % differences. As before, the small IQRs in TDAS further support that TDAS often measures the same energy as FDAS, as expected. Next, the AS % difference IQR increases slightly as frequency increases in the narrowband case but is much smaller for the harmonics, ultraharmonics, and broadband. Lastly, for RCB, there is no apparent frequency-dependent trend, but the % difference IQR is greater than TDAS and AS in the narrow frequency bands. There was large variability in frame-frame differences both within experiments and across different experimental conditions. Like AS, however, RCB's IQRs are smaller in the harmonic, ultraharmonic, and broadband cases.

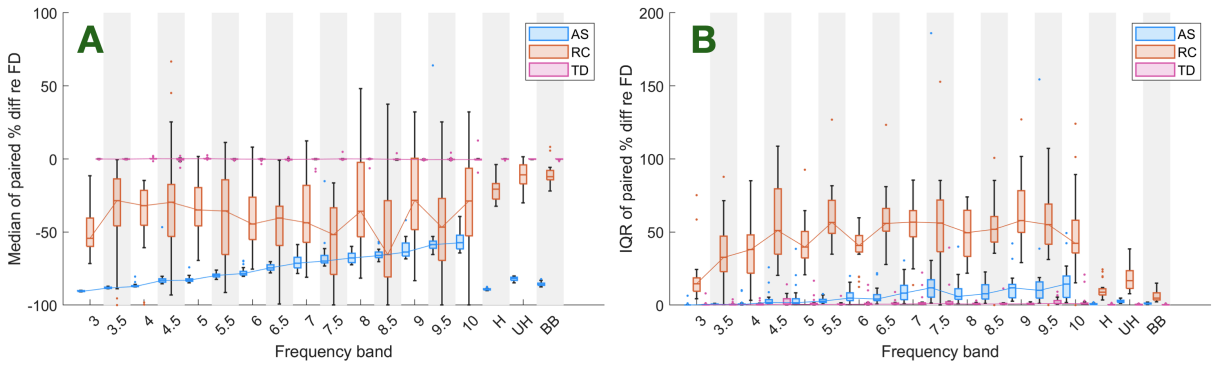


Figure 4.5: Summary of pairwise beamformer cavitation dose differences from FDAS algorithm over frequency for all experiments (N1-3) and pressures above the cavitation threshold. AS=angular spectrum, RC=Robust Capon, TD=time-domain delay-and-sum. A) Boxplots show the median pairwise % difference of 45 frames for each experimental condition (beamformer, experiment number, pressure) above the cavitation threshold. B) Boxplots show the IQR (interquartile range) of pairwise % differences in 45 frames for each experimental condition.

4.5 Source Localization Accuracy

The source localization accuracy was determined based on the distance between the maximum pixel location in the map to the known tube location from the B-mode images. These are traced by the black lines in relation to pressure (on the vertical axis) in the 3D representations in Figure 4.3 and in relation to the frequency band (on the vertical axis) in Figure 4.6.

4.5.1 Constant Frequency / Varied Pressure

Referring to the pressure-dependent behaviour in Figure 4.3, we see the black lines tracing the maximum pixel location for the harmonic, ultraharmonic, and broadband frequencies. Below the cavitation threshold (approximately 300-400 kPa for harmonics and broadband, and 500 kPa for ultraharmonics), where the signal is low, the position error is greater. The maximum positions of AS, FDAS, and TDAS are deep relative to the actual tube location (in grey), whereas RCB can vary above or below the tube location. As the pressure increases above the cavitation thresholds, the positions of the maxima stabilize at a constant, closer distance to the tube. Compared to AS, FDAS, and TDAS, RCB achieves a closer final position to the tube position. For these plots in the narrowband frequencies and for the other experiments, refer to Appendix A.1.2.

4.5.2 Constant Pressure / Varied Frequency

Next, Figure 4.6 shows the frequency-dependent PCM outputs in a similar fashion as Figure 4.3, but with normalized colourmaps. From the stacked PCM representations, we see a general trend of the maximum pixel location approaching the true tube location as the narrow frequency band increases for AS, FDAS, and TDAS in the 700kPa and 1000kPa cases (Figure 4.6B, C). In comparison, the maximal location computed by RCB is closer to the true tube location for each frequency band (representative distances are summarized in Table 4.1). At 400 kPa Figure 4.6A, which is close to the cavitation threshold for harmonics and below the threshold for ultraharmonics, there is more variability in the maximum pixel location for all the beamformers.

The localization errors obtained for each frequency in each experimental condition are summarized in Figure 4.7. The box plots summarize the signed distance error from the tube centre with respect to frequency for all frames in experimental conditions above the cavitation threshold (n=45 in each box plot). A positive localization error indicates a PCM-derived location that is deeper than the true location. The same frequency-dependent trends for each beamformer are apparent here. In the case of the harmonics, ultraharmonics, and broadband cases, their maps are dominated by signals in the lower bands (3-4 MHz), so their pixel locations are influenced by those as well.

Table 4.1: Mean ± Std Dev of Distance (mm) from Maximum Pixel to Tube Centre

Localization error, mm (Mean ± Std. dev.)			
	3 MHz	5 MHz	10 MHz
AS	7.02±1.53	3.14±2.24	1.23±1.76
FDAS	7.68±1.86	3.64±2.60	1.23±1.53
TDAS	7.85±1.94	3.70±2.65	1.24±1.54
RCB	2.46±2.03	1.94±1.15	0.88±1.46

4.6 PCM Beam Area Performance

To evaluate the beam area, the area of the top 90th percentile of pixels (A90, or pixels within 10% of the maximum value) was computed for each PCM map. The A90 trends are summarized

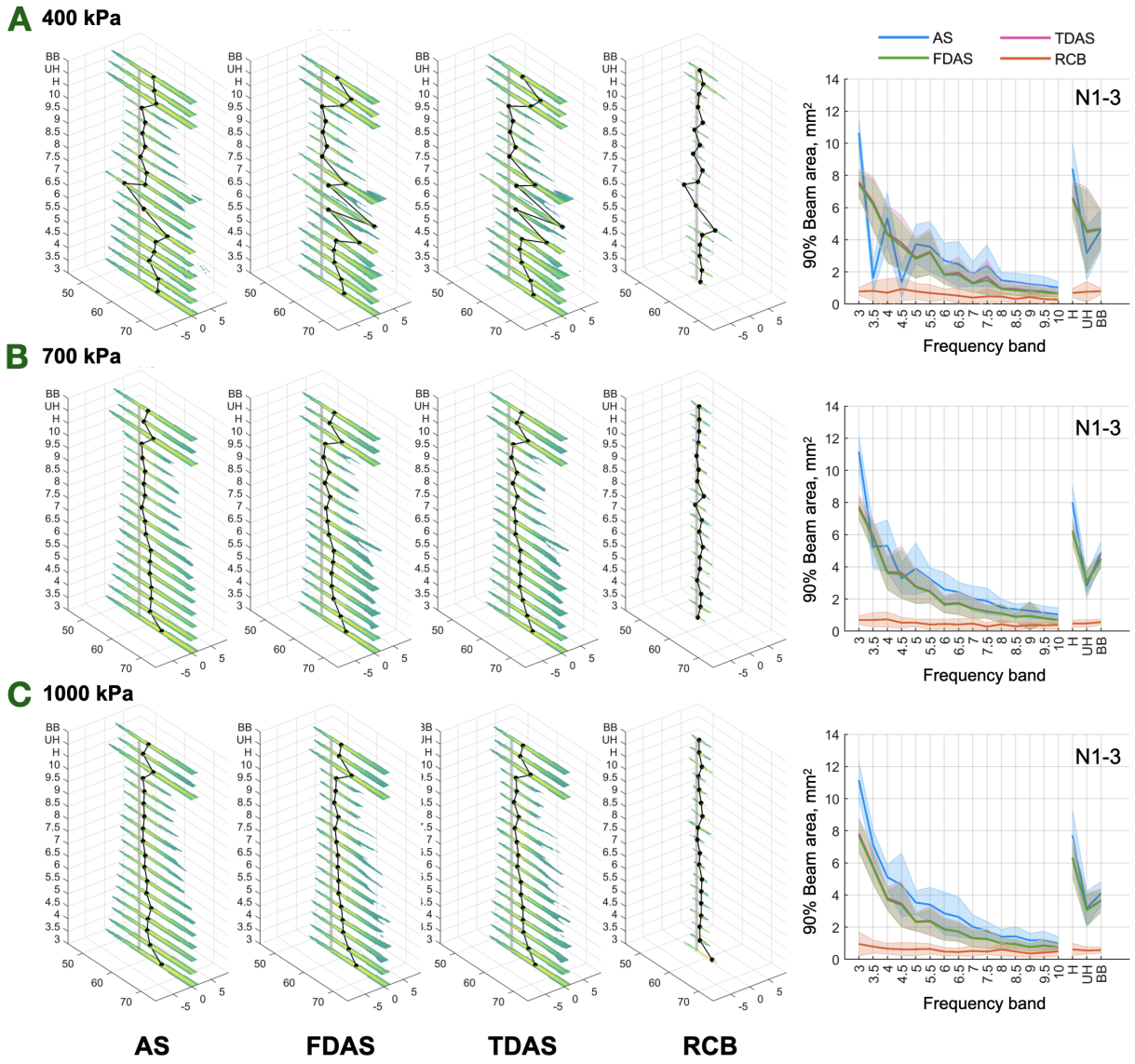


Figure 4.6: Summary of beamformer outputs against frequency at A) 400 kPa, B) 700 kPa, and C) 1000 kPa, averaged over 15 acquisitions in experiment 1 (N1). Left to right: Stacked 2D cavitation maps from each beamformer – AS (angular spectrum), FDAS (frequency-domain delay-and-sum), TDAS (time-domain delay-and-sum), and RCB (Robust Capon Beamformer) – at each frequency band (z-axis). Only the top 50 percentiles of pixels in each map, representing the 6dB beam area, are coloured. The colourmaps are normalized based on the maximum pixel value in each frame. The gray cylinder passing through each map represents the true position of the inner diameter of the silicone tube. The black line traces the location of the maximum pixel of each map. Last column: Mean and std. dev. (shaded) beam area from the top 90 percentile of pixels in each map for all experiments (N1-3).

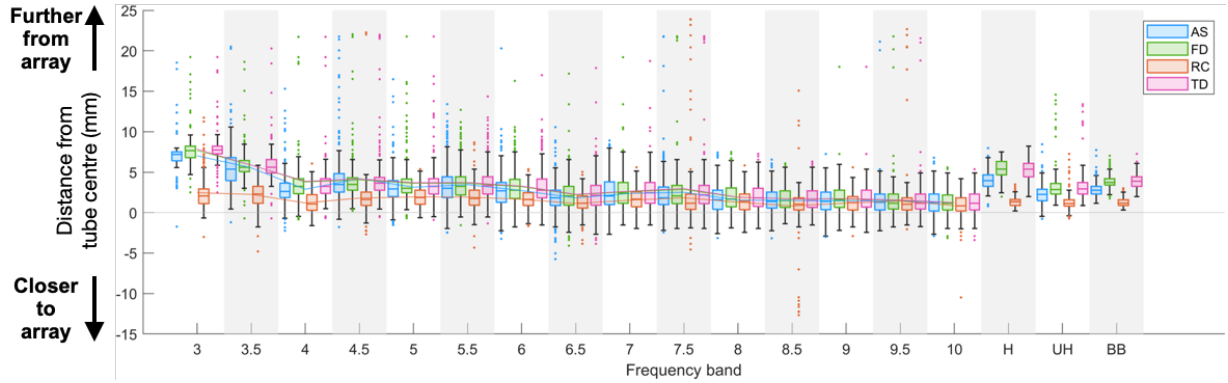


Figure 4.7: Summary of beamformer maximum pixel distances to the tube. Box plots contain distances from all experiments (N1-3) and pressures above the cavitation threshold.

in Figures 4.3ii and the rightmost column of 4.6. First, looking at pressure-dependent behaviours in Figure 4.3ii, the harmonic, ultraharmonic, and broadband beam areas appear to increase, decrease, and decrease slightly, respectively, as a function of pressure for AS, FDAS, and TDAS when above the cavitation threshold. In contrast, the rightmost column of Figure 4.6 shows frequency-dependent beam area trends for AS, FDAS, and TDAS. As narrowband frequency increases, the beam area decreases non-linearly, with AS having a slightly larger mean beam area than FDAS and TDAS. Unlike the other methods, the RCB beamwidth is constant with increasing pressure and frequency.

A comparison of the -6dB dose beam area is also presented in Figure 4.8, which shows the mean lateral and axial beamwidths computed from each PCM map above the cavitation threshold against a theoretical value for the beamwidths. The theoretical values were obtained with the Fresnel approximation of the diffraction pattern of a rectangular aperture for an on-axis point source using Equations 2.8 and 2.7. First, examining Figure 4.8(A, C), the lateral beamwidths for AS, FDAS, and TDAS follow the theoretical beamwidth as frequency increases, asymptotically approaching the tube size of 0.6 mm (which the theoretical beamwidth passes). RCB does not seem to exhibit a frequency-dependent relationship and remains closer to the tube size or smaller. In the axial case, AS, FDAS, and TDAS again follow the theoretical values, with AS having a slightly longer depth of field and the DAS beamformers performing slightly better. Conversely, RCB has a relatively constant depth of field that consistently performs better than the theoretical diffraction pattern but is still approximately ten times longer than the true tube size.

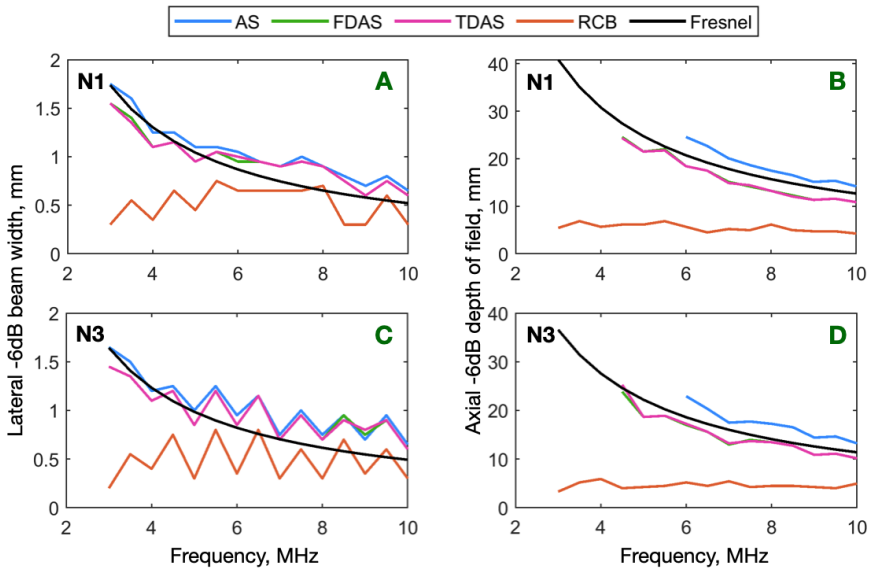


Figure 4.8: Lateral (A,C) and axial (B,D) -6dB beam widths of each PCM algorithm compared to the theoretical beam width plotted against frequency. The theoretical -6dB beam width (black) was calculated the Fresnel approximation for a rectangular transducer (Equations 2.8 and 2.7). Experiments N1 and N3 are shown here since they represent the on-axis case assumed by the approximation.

4.7 Cavitation Dose vs. Hydrophone

Figure 4.9 summarizes the results comparing the hydrophone as a reference PCD (HGL-400) to the equivalent from the PCM array (L14-5). First, the mean energy density spectra obtained from the distance-compensated, raw RF data from the hydrophone and array are presented in Figure 4.9A for each pressure condition in the first experiment. Similar to the results discussed in Section 4.2, the spectra from the L14-5 show an increasing trend, with the harmonics starting to appear at around 200 kPa, ultraharmonics around 700 kPa, and the broadband (indicated by a rising baseline) around 400 kPa. The HGL-400 spectra show a similar trend for the 3rd and 4th harmonics at 3 and 4 MHz, which appear to onset at 300 and 400 kPa, respectively, as seen in the inset. However, the spectra for the HGL-400 have a higher noise floor than many of the L14-5's higher harmonics at 1000 kPa and, therefore, also lack many of the spectral features present in L14-5, such as the presence of higher harmonics, ultraharmonics, and broadband increase. Additionally, the magnitudes of the HGL-400 spectra at 3 and 4 MHz underestimate

that of the L14-5 by 12-fold and 4-fold, respectively, at 1000 kPa. We see the effect of these spectral differences in the resulting cavitation dose calculation in Figure 4.9B, which compares the dose from the HGL-400 hydrophone to the L14-5 RF data and the FDAS beamformer. For the dose computed from the hydrophone, the harmonics are underestimated at high pressures and overestimated at low pressures. The ultraharmonic and broadband doses change according to the noise profile on the hydrophone and have no relation to the doses computed from the L14-5 pre-beamformed and FDAS methods. The corresponding plots from the other experiments, provided in Appendix A.4, show similar trends. The effect of the noise present on the HGL-400 was an unexpected finding, and its impact is addressed further in Chapter 5.

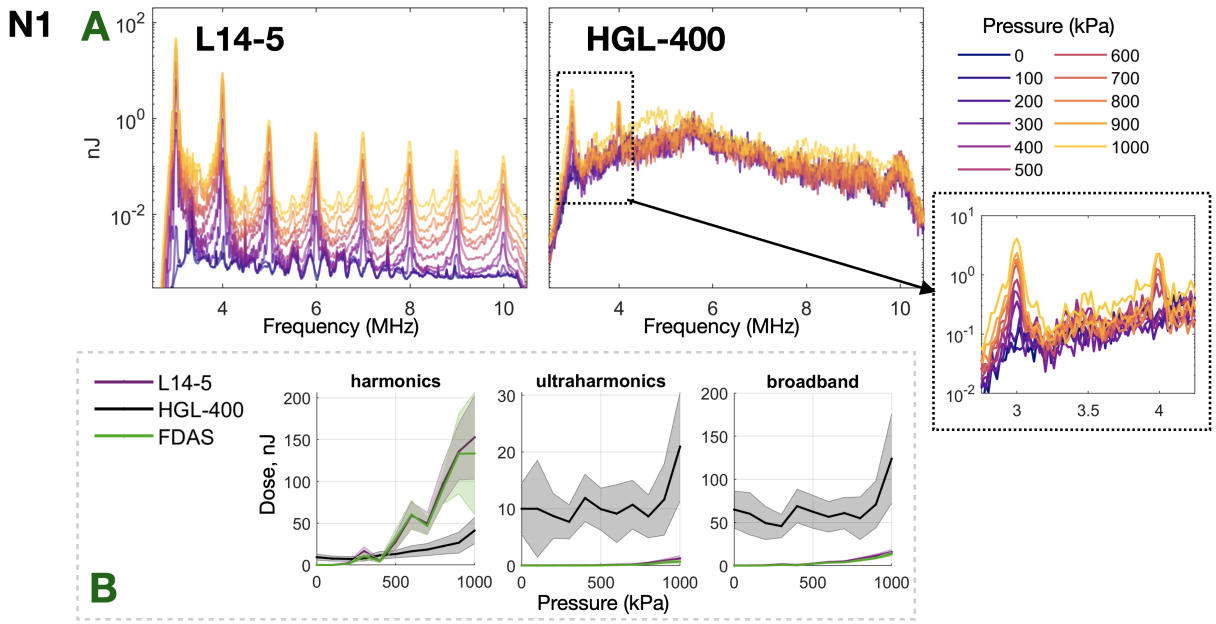


Figure 4.9: Summary of reference hydrophone PCD readings against PCM output in experiment 1. A) Mean spectra as simultaneously detected on the L14-5 array (left) and the HGL-400 hydrophone (right) over each pressure from 0 to 1000 kPa. The inset shows a closer view of the HGL-400 spectrum at the 3rd and 4th harmonics. B) Cavitation dose computed from the RF data of the L14-5 and HGL-400 compared to that of FDAS PCM beamformer in the harmonic, ultraharmonic, and broadband frequency bands.

4.8 Array Calibration and FUS Characterization Results

The 3D pressure field of the FUS transducer around the tube was mapped and is shown in Figure 4.10. From Figure 4.10A, the transverse cross-section of the silicone tube (light blue) fits within -3dB beam width of the focal area. Figure 4.10B presents the FUS field profile along the tube with a sweep of the nominal pressures experienced by the MBs in the tube. From these measurements, the maximal width of the beam above the cavitation threshold (assumed to be between 200 to 300 kPa as determined in Section 4.3) is 3.2 mm in the 1000 kPa case.

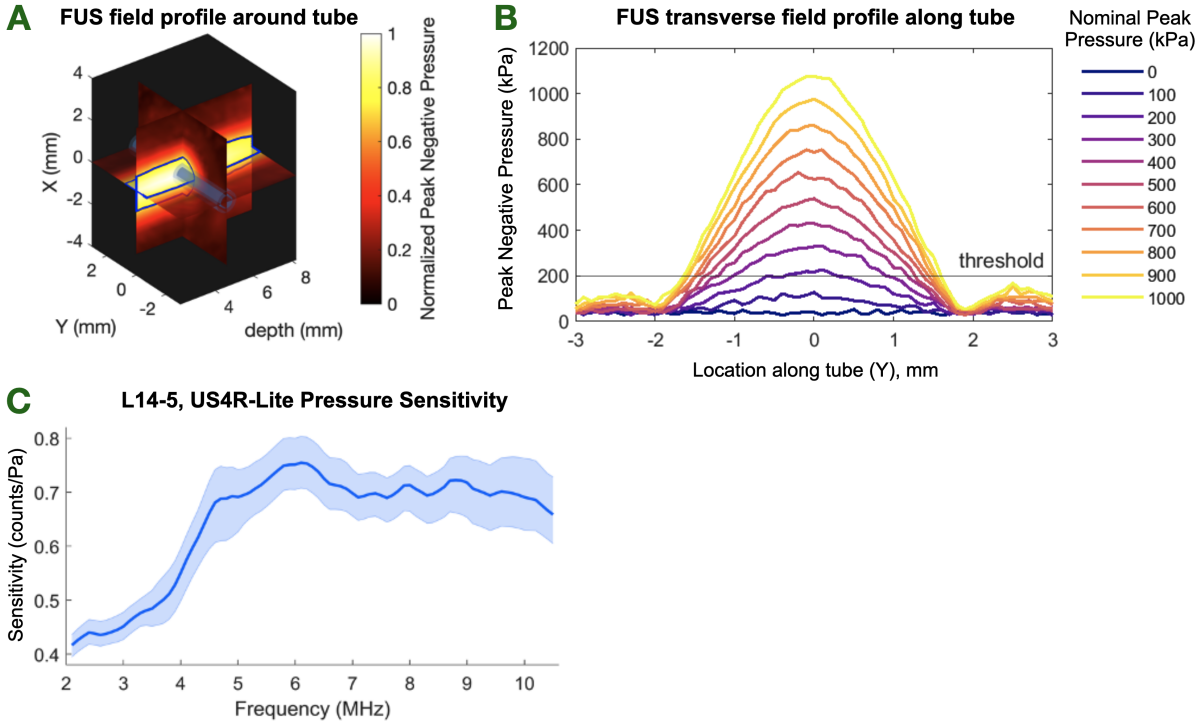


Figure 4.10: A) 3D field profile of the FUS focal area surrounding the tube (light blue). B) Detailed field profile scanned along the tube at the tested input pressures between 0-1000 kPa. C) Mean element receive sensitivity of L14-5 array as detected on the US4R-Lite scanner operating at 40 dB. Shaded error bars indicate the standard deviation over the 64 channels.

Chapter 5

Interpretation and Discussion of Experimental Results

5.1 Chapter Overview

This Chapter presents the interpretation of the trends observed in the previous Chapter, with reference to expected results from current literature and the specifics of the beamformer implementations. Interpretation of cavitation dynamics, relative dose differences, spatial performance, and PCM vs. PCD analysis are detailed. The Chapter concludes with a discussion of the advantages and limitations of the study.

5.2 Observed Cavitation Doses Versus Expected Cavitation Dynamics

5.2.1 Cavitation Thresholds

As discussed in Section 2.2, the cavitation dose thresholds should correspond to the onset of different cavitation regimes as pressure increases. This is also related to the proportion of the FUS beam in different pressure bins, as shown in Figure 4.10. As the pressure increases, a greater length of the tube lumen (up to 3.2 mm) is exposed to ultrasound, affecting how many bubbles are insonified at different pressure magnitudes. As such, the regions experiencing different cavitation

regimes change, affecting the measured cavitation dose in each frequency band. It is important to keep in mind that the measured bubble activity is innately heterogeneous throughout this experiment.

The initial onset of harmonics between 200-300 kPa (recall Figure 4.4) corresponds to the onset of non-linear bubble vibrations, which agrees with expected pressure thresholds for this type of microbubble (Stride & Coussios, 2019). The onset of the ultraharmonic peaks in the spectra occurs between 500-700 kPa, which also agrees with the typically expected pressure (Stride & Coussios, 2019), corresponds to the onset of increasingly non-linear vibration modes commonly seen before the onset of inertial cavitation. However, the onset of broadband components, which generally correspond with the most transient and violent bubble dynamics, appears to track the harmonics and occur earlier than the ultraharmonic components. This is not typical behaviour and is likely an erroneous measurement due to spectral leakage of the nearby high-amplitude harmonic components into adjacent frequency bins, which can be seen in the pre-beamformed spectra in column 4 of Figure 4.4. Spectral leakage is an important signal processing consideration for PCM (Haworth et al., 2017). It is a consequence of performing a discrete Fourier transform on a finite-duration signal, resulting in increased bandwidth of narrowband signals. In this experiment, a given bubble spends a limited time exposed to ultrasound (20 cycles), which also makes inertial cavitation less likely to occur compared to pulses with longer cycles (Y. Lin et al., 2017; Xu, He, Zhong, Qiu, & Tu, 2019). As such, it is unlikely that the supposed initial onset of the broadband component is due to 'premature' inertial cavitation but spectral leakage. As shown by Haworth et al. (2017), the effects of spectral leakage can be mitigated by selecting an appropriate windowing function, though this was not the focus of this experiment. At higher pressures (800-1000 kPa, Figure 4.4), the broadband dose is likely a combination of energy from both spectral leakage and inertial cavitation events. The presence of inertial cavitation is evident in experiment N1, where the harmonic dose plateaus after 900 kPa (so its contribution to the broadband dose through spectral leakage stops increasing), but the broadband and ultraharmonics continue to rise. Plateaus or decreases in the harmonic and ultraharmonic components at high pressures may indicate energy being transferred to the broadband components due to the transition from stable to inertial cavitation.

Aside from the artifactual dosing of broadband components, the PCM-derived cavitation doses qualitatively correspond to the expected cavitation dynamics in this experiment. This also shows

that the cavitation exposure platform can generate a variety of cavitation regimes on which to test the performance of PCM algorithms.

5.2.2 Non-Beamformed Dose is Greater than Beamformed Dose in Ultraharmonic and Broadband Frequencies

In addition to comparing beamformer-derived doses, cavitation dose derived from pre-beamformed (RF) data was also included in Figure 4.4, where we saw that the estimated cavitation dose was slightly greater for the ultraharmonics and broadband than for the beamformed data, but agreed closely to the DAS beamformers for the harmonics. Due to the design of the experimental setup to position the treatment volume fully within the array's elevational focus, it was expected that the RF data would contain all the cavitation activity occurring within the treated volume and thus yield similar dose estimates as the beamformed data. The discrepancy between RF and PCM-derived ultraharmonics and broadband doses, in particular, could be partly due to the spectral leakage. As discussed above, the higher amplitude of the harmonic frequencies contributes to the ultraharmonic and broadband frequencies via spectral leakage. Since windowing does not affect the phase content of the RF data, the DAS beamforming operation may be able to suppress some of the effects of spectral leakage, resulting in a lower estimated beamformed dose than non-beamformed dose. Addressing the spectral leakage limitation through the appropriate choice of windowing functions would help increase the overall accuracy of both beamformed and non-beamformed doses and reduce the uncertainty in future quantitative assessments.

Overall, the agreement between the non-beamformed and beamformed cavitation doses demonstrates that utilizing a reference PCD is a feasible way to evaluate the cavitation dose accuracy of PCM algorithms.

5.3 Factors Affecting Dose Estimation Difference

5.3.1 Equivalence between Time- and Frequency-domain Delay-and-Sum

As expected, the time-domain and frequency-domain implementations of the delay-and-sum beamformer for PCM were shown to be equivalent in Section 4.4. This was evident when comparing the two implementations' absolute magnitudes and relative differences. However, FDAS

was significantly faster than TDAS, even when beamforming the full bandwidth. Additionally, although pre-filtering was implemented to maintain signal consistency, FDAS can beamform multiple frequency bands simultaneously. In contrast, TDAS relies on pre-filtering followed by multiple beamforming operations to extract the maps with specific spectral features. Therefore, while the cavitation dose and spatial performance were equivalent, FDAS is preferred over TDAS due to its faster computational speed and flexibility.

5.3.2 Constant Percent Differences Between Angular Spectrum and Delay-and-Sum

One of the main observations in the Results section is that there is a frequency-dependent bias in the mean doses between AS and FDAS, and this bias is not dependent on the pressure as long as there is enough signal (i.e., above the cavitation threshold). In Figure 4.5, the median % difference appears to have a linear relationship with frequency in the 3-10 MHz frequency range. The origin of this bias could be innate algorithm differences, experiment-specific, or both. The main difference between the two algorithms is that AS is signal-energy-preserving through the forward and inverse Fourier transforms by Parseval's theorem, whereas FDAS, in using coherent summation, is not. Looking at Equation 2.32, AS forms 2D images one lateral line in depth at a time. At every depth line, AS performs a forward and inverse Fourier transform. Hence, its innate assumption is that the energy incident upon the array is the sum energy of any cavitation sources in the RF data at that depth and will distribute this energy in the lateral direction. (This can be proven by summing the signal energy across every lateral line after removing spherical compensation.) If the bias between AS and FDAS could be characterized, there could be merit in determining a frequency-dependent correction factor to reconcile the cavitation doses calculated from AS and FDAS (or other methods), given that they follow the same trend. This could be valuable since AS beamforms significantly faster than the other tested beamformers (Arvanitis et al., 2017), making it a relatively easy-to-implement candidate for real-time PCM. Correcting the dose bias would enable translatable cavitation dose values in the literature. However, since testing the dose bias in all experimental configurations was not the focus of this experiment, it is possible that other experimental configurations with multiple cavitation sources in disparate spatial locations could affect the degree of bias and, thus, the correction factor. Nevertheless, we revealed a frequency-dependent constant dose difference between the AS and DAS techniques for

PCM.

5.3.3 Large Variation in Differences Between RCB and Delay-and-Sum

Compared to AS and TDAS, the RCB algorithm shows much higher variability in the pairwise % differences in cavitation dose compared to FDAS (Figure 4.5). The magnitude of the variability is higher in the narrow-frequency bands than in the multi-frequency bands. This is likely tied to the stability of the tuned optimization parameter, ε, which is data-dependent. Recall from Section 3.4 that the tuning process is performed independently on all frequency bands and input pressure separately and is based on the relative maximum pixel value of 5 frames to FDAS. In reviewing the tuned values of ε in Figure 4.2, the variability in the optimal ε values, like the pairwise differences, is higher for the narrow frequency bands (3-10 MHz) compared to the multi-frequency bands (H, UH, BB). This means the narrowband ε values tuned on five frames in each data set were less generalizable to the remaining ten frames in the dataset, resulting in higher variability in the resulting beamformed dose within each experimental condition. Additionally, they were also not generalizable between the different pressures. In contrast, the values of ε tuned for the wider frequency bands (H, UH, BB) were more generalizable to both the frames within a specific pressure and to frames between different pressures. The data- and system-dependence of the optimal tuning of parameter ε is well documented, with a range of reported optimal values depending on the beamformed frequency, ultrasound system and number of cavitation sources (Polichetti et al., 2021; Coviello et al., 2015).

The difference in wide- and narrowband performance seems counterintuitive due to RCB and other optimal beamformers often being used to enhance narrowband signals in the far field (Van Veen & Buckley, 1988). However, simulations and analysis of RCB for PCM were developed with mostly broadband signals in mind, and interference suppression was demonstrated for a broadband bubble cavitation model (Coviello et al., 2015). Coviello et al. show that TDAS (and, consequently, FDAS) is susceptible to overestimating cavitation due to multi-bubble interactions. The interference suppression ability is demonstrated in Section 4.3 Figure 4.4 where the cavitation doses reported by RCB were generally slightly less than TDAS or FDAS. The analysis shown in this experiment supports the preferred use of RCB for wide-band cavitation data while showing less stable performance with narrowband cavitation data.

5.4 Frequency-Dependent Spatial Performance

As seen in Sections 4.5 and 4.6, the most apparent trend is the increasing spatial performance in both maximum pixel location accuracy and beam width with increasing frequency for AS, FDAS, and TDAS. This is an expected result due to the spatial resolution of passive beamformers being defined by the point-spread-function or diffraction pattern of the imaging array used (Haworth et al., 2017; Stride & Coussios, 2019) instead of pulse length. Due to this, the nominal lateral and axial beamwidths are directly related to the array geometry (aperture size) and wavelength of interest as described in Equations 2.8 and 2.7 explained in Section 2.3.2.

In comparing the lateral and axial beamwidths of the three non-optimal beamformers (AS, FDAS and TDAS) to the theoretical beamwidth in Figure 4.8, AS appears to have the largest beam area overall. Additionally, these methods follow the theoretical beamwidth given by the Fresnel approximation. AS has the longest depth-of-field in the axial direction, exceeding the Fresnel approximation, while FDAS and TDAS have a shorter depth-of-field. These relative relationships are consistent with existing literature (Arvanitis et al., 2017). In contrast, RCB improves upon pixel localization and beam area without apparent frequency dependence, especially in tail artifact suppression. FDAS and TDAS are prone to tail artifacts, or the lengthening of the beam past the expected region, which can be attributed to interference and correlation between multiple bubbles within the focal area (Coviello et al., 2015), a factor in this experiment.

In addition to reduced beam area, the error in maximum pixel location decreases asymptotically with increasing frequency for AS, FDAS, and TDAS (Figure 4.7, Table 4.1). This corresponds with the decreasing beam area. The minimum error stabilizes to approximately 1.23 mm from the true location, or 1 pixel in the lateral direction and 4-5 pixels in the axial direction. The spherical compensation profile might explain some of this. Spherical compensation is required for calculating the source energy; however, it may also introduce bias in the maximum pixel location for those algorithms with longer beamwidths. If we assume that without the spherical compensation, the axial beam's maximum is at the tube location, multiplying this by a linearly increasing function can shift the position of its peak and increase the overall axial beamwidth. Incorrect localization of the source away from the centre of the transducer is not uncommon (Telichko, Lee, Jakovljevic, & Dahl, 2021). Still, we can see that strategies that decrease the beamwidth and suppress interference (e.g., RCB) are less affected.

Overall, we showed that the data from the designed experimental configuration is capable of simultaneously testing the spatial and dose magnitude performance of the PCM algorithms. The algorithms' spatial performances align with expected values, validating the primary hypothesis.

5.5 Hydrophone as a Passive Cavitation Detector

In Section 4.7, we showed that although the HGL-400 hydrophone could detect some of the cavitation dynamics in the 3rd and 4th harmonics, there were two main discrepancies. The first discrepancy was that the hydrophone noise shielded most of the cavitation dynamics. The second discrepancy was that the magnitude of the hydrophone's energy density spectrum was much smaller, and the relative magnitudes between the 3rd and 4th harmonics differed from those on the L14-5 array. Unfortunately, the complete cause for the difference is unknown, but there are some possible explanations. We hypothesize the hydrophone or its preamplifier may have sustained some damage prior to the experiments that may have affected its electrical shielding (allowing for noise injection) and sensitivity. During the implementation of the experiment, we noticed relatively high-amplitude (approximately 100-200 mV compared to <50 mV cavitation signal) impulsive electrical noise in ultrasonic frequencies that appeared on the hydrophone's oscilloscope channel when the hydrophone was dipped in the water. Further evidence for poor electrical isolation was the presence of signal bleed-through from the function generator's excitation pulse that partially drove the decision to use 20-cycle pulses to prevent signal overlap. Although we found that signal averaging over multiple acquisitions can reduce the noise amplitude, this was not performed since that would have also filtered out the broadband cavitation signals, which are also stochastic and impulsive. Overall, significant effort was made to address these limitations before the experiment and during the analysis and preparation of this thesis, but it was not possible to replace the hydrophone in the thesis timeline. Thus, due to limitations in the instrumentation, the use of a hydrophone as an independent 'ground truth' validation method for cavitation dose (secondary hypothesis), while promising, was inconclusive in this experiment.

5.6 Advantages and Limitations of the Study

5.6.1 Single Experimental Configuration

In this study, we proposed an experimental geometry where the position and orientation of the tube perpendicular to the array aperture allowed for the simultaneous evaluation of both total cavitation dose and spatial performance. An advantage of this approach is that the treated volume could be easily measured, identified, and contained within a small field of view for dosing purposes. One of the limitations discussed above pointed out that in this pseudo-single-point-source setup, we cannot easily empirically measure any data-dependent or spatial-dependent effects on cavitation dose bias (e.g., with the AS beamformer). However, the scope of such a study is likely better suited to simulations, which can then inform experimental validation on an experimental setup like this using a reduced set of configurations.

5.6.2 Constant Preprocessing Steps

The use of constant preprocessing steps (prefiltering and sampling) is required because they reduce the number of confounding factors when comparing the relative performance of beamformers. In practice, however, when implementing time-domain and frequency-domain passive beamformers, researchers tend to use filtering techniques that match their operating domain to separate the harmonic, ultraharmonic, and broadband components. For example, in TD beamforming, RF data are almost always filtered to the desired frequency bands before beamforming, such as with FIR bandpass, notch, and comb filters. Conversely, in FD beamforming, only the frequencies of interest are beamformed, an equivalent process to the frequency masking used in this study. However, as discussed in Section 5.2, the preprocessing steps complicated the interpretation of cavitation dynamics (due to spectral leakage). While the scope of the preprocessing allowed us to assess beamformer-specific differences, future work assessing the performance of different frequency-band filtering techniques (such as Lyka, Coviello, Kozick, and Coussios (2016)) could provide more confidence in the accuracy of the stable and inertial cavitation doses.

5.6.3 Hydrophone Codetection

Unfortunately, the key limitations in this study were the hydrophone's hardware issues preventing its use as a robust reference value for cavitation dose. In the initial testing for the development of the experimental geometry, the hydrophone's low sensitivity justified closer positioning to the cavitation target (5.5 mm) than the linear array (53-57 mm), which would not reflect clinical scenarios. Additionally, the interfering noise resulted in an inability to confidently compare cavitation doses between PCD and PCM as intended. While we were able to use the same PCD signal processing techniques by using the pre-beamformed linear array RF data as a PCD, this did not accomplish our initial goal of using an *independent* acoustic reference measurement. Finally, in this configuration, 1:1 PCD-PCM waveform analysis was not possible with the current oscilloscope instrumentation setup, so the PCD-PCM analysis was also limited to the average dose over the total exposure time. In summary, codetection was a part of the evaluation that did not work as planned with the available instrumentation.

To address these limitations, the hydrophone would be replaced with a properly shielded dedicated PCD transducer with greater sensitivity. An unfocused PCD is less sensitive than a focused PCD but would be a more direct replacement for the hydrophone. A focused PCD transducer would have greater sensitivity that would allow it to be placed at a similar distance from the tube as the PCM. However, since the frequencies of interest are higher than the excitation frequency, its beam width would likely not be sensitive to the entire 3.2 mm insonified length of the tube. Thus, to ensure a comparable cavitation dose, this would need to be addressed by altering the orientation of the linear array so that its aperture is parallel to the tube and then registering the PCD-detected beam area with the resulting PCM-derived dose. This configuration would remove the ability to simultaneously assess spatial localization (which is already a large focus for existing algorithms) but could provide a richer cavitation image with spatial differences in cavitation regimes.

Chapter 6

Significance and Conclusions of Study Findings

6.1 Summary of Contributions

PCM has become an increasingly important technique for localizing and quantifying cavitation activity for controlling cavitation-based therapies such as blood-brain-barrier opening and targeted drug delivery. While quantitative PCM with absolute values is needed to elucidate the relationships between cavitation dose and bioeffects, a comprehensive comparison of the cavitation dose accuracy in combination with spatial localization metrics has not been performed. To address this need, we proposed a platform for codetection of cavitation with a calibrated ultrasound array and hydrophone to simultaneously evaluate the spatial and dose accuracy of PCM algorithms. We derived absolute implementations of four popular beamformers, TDAS, FDAS, RCB, and AS, which considered the effects of spherical spreading and discrete-time processing, thus allowing for the direct comparison of dose magnitudes. The experimental platform enabled the comparison of beamformer performance on various cavitation dynamics, which correlated well with the expected behaviours. Even with the appropriate spherical-spreading modelling and discrete-processing scaling factors, we demonstrated innate beamformer differences in computing cavitation dose for AS and RCB compared to the DAS methods. Although issues with hydrophone instrumentation prevented the full realization of an independent codetection scheme, the agreement between non-beamformed and beamformed cavitation doses showed that comparing total

cavitation doses from a PCD with this experimental configuration is feasible.

6.2 Significance of Study Findings

6.2.1 Equivalent Beamformer Implementations Reveal Fundamental Differences

By implementing beamformers with equivalent models and evaluating cavitation dose magnitudes from the proposed experimental platform, we were able to show some fundamental differences between beamformers. Specifically, we demonstrated a frequency-dependent bias in the AS-derived cavitation dose compared to the DAS methods. In addition, we also showed frequency bandwidth-dependent stability of RCB estimates. We also showed that the spatial performance differences aligned with the expected results reported in previous studies, demonstrating that the proposed experimental platform could successfully validate the relative performance between beamformers. On a broader scale, the algorithmic dose results imply that without accounting for beamformer-dependent biases and variation in future dose-bioeffect studies, we will continue to see significant variations in computed dose-bioeffect relationships that will be difficult to decouple from beamforming effects. However, by assessing PCM algorithms' cavitation dose accuracy, such as in this study, we can make more informed selections of PCM methods and, in the future, account for biases introduced by different beamformers.

6.2.2 Standardization of Cavitation Dose

The steps to cavitation dose standardization involve the characterization of the sources of error in PCM (this thesis), analysis of the importance of different dose metrics, and standardization of dose reporting. The biases demonstrated between algorithms strengthen the motivation to standardize cavitation dose reporting. There are existing guidelines for reporting the ultrasound exposure parameters in therapeutic ultrasound (Padilla & ter Haar, 2022); however, these focus mainly on the excitation ultrasound, or input, parameters. While the guidelines' most recent iteration was updated to include some guidance for reporting treatment monitoring methods such as PCM and PCD, we have shown that the doses computed from quantitative PCM and PCD are multifactorial, dependent on the system bandwidth, preprocessing, and beamforming method. As

such, dose-bioeffect studies would also benefit from a guideline for standard reporting of cavitation dose. The key parameters not addressed in the current guidelines include reporting the doses in physical units (Joules or similar), the array's element sensitivity, and the signal processing details to inform readers of the potential sources of dose biases. Including these parameters in PCM research would aid in unifying research between the ultrasound inputs, acoustic cavitation outputs, and biological outcomes.

6.3 Future Directions

6.3.1 Evaluation of the Wider Scope of PCM Algorithms

There are several ways we could expand the scope of PCM algorithm evaluation – either through further testing the signal processing methods or making changes to experimental configurations. A natural extension to this study would be to perform a similar analysis on more of the beamformers presented in Table 2.1 with the suggested changes to the PCD instrumentation. The scope of testing could also be expanded by varying the harmonic/ultraharmonic/broadband filtering methods to determine any effect on beamformer performance and accuracy. To address the limitation of the single test configuration, we can also swap out the linear array or scanner or repeat it in different scenarios. A collaborative approach that would aid in standardization efforts would be to make the experimental platform and data available to other researchers (and vice-versa, for their own implementation), which would provide opportunities for cross-platform cross-validation. Together, these efforts would accumulate a greater body of data from which we could analyze the relationships behind the beamformer-specific dose biases, as discussed in Chapter 5.

6.3.2 Combined Approach for PCM Image Formation

Knowledge gained from the beamformer comparisons can undoubtedly drive innovations for new PCM techniques. One approach would be to combine multiple beamformers in such a way as to leverage their different advantages. To reduce the computational complexity while retaining cavitation dose accuracy, an image mask could be derived from a beamformer with a smaller beam area, such as RCB, and applied to a cavitation map generated with a faster beamformer,

such as AS or FDAS. This could be useful in a therapeutic scenario where the treatment requires a sustained level of cavitation in a fixed volume, where the cavitation region would be expected to change at a slower rate than the dose. Such a combined approach was recently explored by Haworth, Salido, Lafond, Escudero, and Holland (2023), where the authors generated spatial filtering maps based on a phase-coherence factor and successfully applied them to FDAS-derived images to reduce artifacts.

6.4 Concluding Remarks

Accurate measures of cavitation dose play a vital role in the safe and effective use of cavitation-mediated therapies, such as non-invasive blood-brain barrier disruption and intratumoral drug delivery. In this thesis, we devised an experimental platform allowing for the controlled codetection of cavitation activity with a linear array and passive detector, thereby enabling the evaluation of quantitative PCM beamformers on various cavitation behaviours. Analysis of four implemented beamformers revealed differences in their cavitation dose magnitudes that were dependent on the frequencies and bandwidths used. Thus, when PCM algorithms are used to compute cavitation dose in bioeffects studies, even calibrated scanners will produce beamformer-specific biases, which negatively affects the generalizability of these studies. Decoupling the cavitation dose from the effects of the specific beamformer and other signal processing techniques could be facilitated in future works through the standardization of cavitation dosimetry. The experimental methods and analysis presented in this work have provided a starting point for evaluating more PCM algorithms' dose accuracy and developing new approaches that will further guide the design of cavitation-mediated treatments in the clinic. Overall, we expect that the unification of cavitation dose measures will lead to smoother translation of therapeutic ultrasound so that robust, safe, and efficacious targeted treatments can reach patients.

References

Arvanitis, C. D., Clement, G. T., & McDannold, N. (2015). Transcranial assessment and visualization of acoustic cavitation: Modeling and experimental validation. *IEEE Transactions on Medical Imaging*, *34*(6), 1270-1281. doi: 10.1109/TMI.2014.2383835

Arvanitis, C. D., Crake, C., McDannold, N., & Clement, G. T. (2017). Passive acoustic mapping with the angular spectrum method. *IEEE Transactions on Medical Imaging*, *36*, 983-993. doi: 10.1109/TMI.2016.2643565

Bae, S., Liu, K., Pouliopoulos, A. N., & Konofagou, E. E. (2021). Coherence-factor-based passive acoustic mapping for real-time transcranial cavitation monitoring with improved axial resolution. In *2021 IEEE International Ultrasonics Symposium (IUS)* (p. 1-4). doi: 10.1109/IUS52206.2021.9593643

Besson, O. (2018). An alternative to diagonal loading for implementation of a white noise array gain constrained robust beamformer. *Signal Processing*, *152*, 79-82. doi: 10.1016/j.sigpro.2018.05.019

Bouakaz, A., Versluis, M., & de Jong, N. (2005). High-speed optical observations of contrast agent destruction. *Ultrasound in Medicine and Biology*, *31*, 391-399. doi: 10.1016/j.ultrasmedbio.2004.12.004

Boulos, P., Varray, F., Poizat, A., Kalkhoran, M. A., Gilles, B., Bera, J., & Cachard, C. (2016). Passive cavitation imaging using different advanced beamforming methods. In *2016 IEEE International Ultrasonics Symposium (IUS)* (p. 1-4). doi: 10.1109/ULTSYM.2016.7728447

Boulos, P., Varray, F., Poizat, A., Ramalli, A., Gilles, B., Bera, J.-C., & Cachard, C. (2018). Weighting the passive acoustic mapping technique with the phase coherence factor for passive ultrasound imaging of ultrasound-induced cavitation. *IEEE Transactions on Ultrasonics, Ferroelectrics, and Frequency Control*, *65*(12), 2301-2310. doi: 10.1109/TUFFC.2018.2871983

Brenner, D. R., Poirier, A., Woods, R. R., Ellison, L. F., Billette, J.-M., Demers, A. A., ... Holmes, E. (2022). Projected estimates of cancer in canada in 2022. *Canadian Medical Association Journal*, *194*(17), E601–E607. doi: 10.1503/cmaj.212097

Burgess, M. T., Apostolakis, I., & Konofagou, E. E. (2018). Power cavitation-guided blood-brain barrier opening with focused ultrasound and microbubbles. *Physics in Medicine and*

Biology, *63*. doi: 10.1088/1361-6560/aab05c

Canadian Cancer Statistics Advisory, Canadian Cancer Society, Statistics Canada and Public Health Agency of Canada. (2022). *Canadian cancer statistics: A 2022 special report on cancer prevalence* (Tech. Rep.). Toronto, ON: Canadian Cancer Society. Retrieved September 15, 2023, from `cancer.ca/Canadian-Cancer-Statistics-2022-EN`

Capon, J. (1969). High-resolution frequency-wavenumber spectrum analysis. *Proceedings of the IEEE*, *57*(8), 1408-1418. doi: 10.1109/PROC.1969.7278

Chen, H., Brayman, A. A., Evan, A. P., & Matula, T. J. (2012). Preliminary observations on the spatial correlation between short-burst microbubble oscillations and vascular bioeffects. *Ultrasound in Medicine and Biology*, *38*, 2151-2162. doi: 10.1016/j.ultrasmedbio.2012.08.014

Chen, H., Brayman, A. A., Kreider, W., Bailey, M. R., & Matula, T. J. (2011). Observations of translation and jetting of ultrasound-activated microbubbles in mesenteric microvessels. *Ultrasound in Medicine and Biology*, *37*, 2139-2148. doi: 10.1016/j.ultrasmedbio.2011.09.013

Chen, H., & Konofagou, E. E. (2014). The size of blood-brain barrier opening induced by focused ultrasound is dictated by the acoustic pressure. *Journal of Cerebral Blood Flow and Metabolism*, *34*, 1197-1204. doi: 10.1038/jcbfm.2014.71

Cobbold, R. S. C. (2006). *Foundations of biomedical ultrasound*. Oxford University Press.

Coussios, C. C., Farny, C. H., ter Haar, G., & Roy, R. A. (2007). Role of acoustic cavitation in the delivery and monitoring of cancer treatment by high-intensity focused ultrasound (hifu). *International Journal of Hyperthermia*, *23*, 105-120. doi: 10.1080/02656730701194131

Coviello, C., Kozick, R., Choi, J., Gyöngy, M., Jensen, C., Smith, P. P., & Coussios, C. C. (2015). Passive acoustic mapping utilizing optimal beamforming in ultrasound therapy monitoring. *The Journal of the Acoustical Society of America*, *137*, 2573-2585. doi: 10.1121/1.4916694

Daneman, R., & Prat, A. (2015). The blood-brain barrier. *Cold Spring Harbor perspectives in biology*, *7*(1), a020412. doi: 10.1101/cshperspect.a020412

Davies, H. J., Morse, S. V., Copping, M. J., Sujarittam, K., Bourgin, V. D., Tang, M. X., & Choi, J. J. (2021). Imaging with therapeutic acoustic wavelets-short pulses enable acoustic localization when time of arrival is combined with delay and sum. *IEEE Transactions on Ultrasonics, Ferroelectrics, and Frequency Control*, *68*, 178-190. doi: 10.1109/TUFFC.2020

.3026165

de Oliveira, C., Weir, S., Rangrej, J., Krahn, M. D., Mittmann, N., Hoch, J. S., ... Peacock, S. (2018). The economic burden of cancer care in canada: a population-based cost study. *Canadian Medical Association Open Access Journal*, *6*(1), E1–E10. doi: 10.9778/cmajo .20170144

Dollet, B., Marmottant, P., & Garbin, V. (2019). Bubble dynamics in soft and biological matter. *Annual Review of Fluid Mechanics*, *51*, 331-355. doi: 10.1146/annurev-fluid-010518 -040352

Duan, X., Lo, S. Y., Lee, J. C. Y., Wan, J. M. F., & Yu, A. C. H. (2022). Sonoporation of immune cells: Heterogeneous impact on lymphocytes, monocytes and granulocytes. *Ultrasound in Medicine and Biology*, *48*, 1268-1281. doi: 10.1016/j.ultrasmedbio.2022.02.022

Duan, X., Yu, A. C., & Wan, J. M. (2019). Cellular bioeffect investigations on low-intensity pulsed ultrasound and sonoporation: Platform design and flow cytometry protocol. *IEEE Transactions on Ultrasonics, Ferroelectrics, and Frequency Control*, *66*, 1422-1434. doi: 10.1109/TUFFC.2019.2923443

Fink, M., Montaldo, G., & Tanter, M. (2003). Time-reversal acoustics in biomedical engineering. *Annual Review of Biomedical Engineering*, *5*(1), 465-497. doi: 10.1146/annurev.bioeng.5 .040202.121630

Frinking, P. J. A., Bouakaz, A., Kirkhorn, J., Cate, F. J. T., & de Jong, N. (2000). Ultrasound contrast imaging: current and new potential methods. *Ultrasound in Medicine and Biology*, *26*, 965-975. doi: 10.1016/S0301-5629(00)00229-5

Garaszczuk, R., Yong, J. H. E., Sun, Z., & de Oliveira, C. (2022). The economic burden of cancer in canada from a societal perspective. *Current Oncology*, *29*(4), 2735–2748. doi: 10.3390/curroncol29040223

Gray, M. D., & Coussios, C. C. (2018). Broadband ultrasonic attenuation estimation and compensation with passive acoustic mapping. *IEEE Transactions on Ultrasonics, Ferroelectrics, and Frequency Control*, *65*, 1997-2011. doi: 10.1109/TUFFC.2018.2866171

Gray, M. D., Lyka, E., & Coussios, C. C. (2018). Diffraction effects and compensation in passive acoustic mapping. *IEEE Transactions on Ultrasonics, Ferroelectrics, and Frequency Control*, *65*, 258-268. doi: 10.1109/TUFFC.2017.2778509

Gyöngy, M., & Coussios, C. C. (2010a). Passive cavitation mapping for localization and tracking

of bubble dynamics. *The Journal of the Acoustical Society of America*, *128*, EL175-EL180. doi: 10.1121/1.3467491

Gyöngy, M., & Coussios, C. C. (2010b). Passive spatial mapping of inertial cavitation during hifu exposure. *IEEE Transactions on Biomedical Engineering*, *57*, 48-56. doi: 10.1109/TBME.2009.2026907

H. Abadi, S., Van Overloop, M. J., & Dowling, D. R. (2013). Frequency-sum beamforming in an inhomogeneous environment. *Proceedings of Meetings on Acoustics*, *19*(1), 055080. doi: 10.1121/1.4799027

Haram, M., Hansen, R., Bouget, D., Myhre, O. F., Davies, C. d. L., & Hofsli, E. (2023). Treatment of liver metastases with focused ultrasound and microbubbles in patients with colorectal cancer receiving chemotherapy. *Ultrasound in Medicine and Biology*, *49*(9), 2081–2088. doi: 10.1016/j.ultrasmedbio.2023.05.013

Has, C., & Sunthar, P. (2020). A comprehensive review on recent preparation techniques of liposomes. *Journal of Liposome Research*, *30*, 336-365. doi: 10.1080/08982104.2019.1668010

Haworth, K. J., Bader, K. B., Rich, K. T., Holland, C. K., & Mast, T. D. (2017). Quantitative frequency-domain passive cavitation imaging. *IEEE Transactions on Ultrasonics, Ferroelectrics, and Frequency Control*, *64*, 177-191. doi: 10.1109/TUFFC.2016.2620492

Haworth, K. J., Mast, T. D., Radhakrishnan, K., Burgess, M. T., Kopechek, J. A., Huang, S.-L., ... Holland, C. K. (2012). Passive imaging with pulsed ultrasound insonations. *The Journal of the Acoustical Society of America*, *132*, 544-553. doi: 10.1121/1.4728230

Haworth, K. J., Salido, N. G., Lafond, M., Escudero, D. S., & Holland, C. K. (2023). Passive cavitation imaging artifact reduction using data-adaptive spatial filtering. *IEEE Transactions on Ultrasonics, Ferroelectrics, and Frequency Control*, *70*(6), 498-509. doi: 10.1109/TUFFC.2023.3264832

Holfort, I. K., Gran, F., & Jensen, J. A. (2009). Broadband minimum variance beamforming for ultrasound imaging. *IEEE Transactions on Ultrasonics, Ferroelectrics, and Frequency Control*, *56*(2), 314-325. doi: 10.1109/TUFFC.2009.1040

Hu, Y., Wan, J. M. F., & Yu, A. C. H. (2013). Membrane perforation and recovery dynamics in microbubble-mediated sonoporation. *Ultrasound in Medicine and Biology*, *39*, 2393-2405. doi: 10.1016/j.ultrasmedbio.2013.08.003

Hu, Y., Wei, J., Shen, Y., Chen, S., & Chen, X. (2023). Barrier-breaking effects of ultrasonic

cavitation for drug delivery and biomarker release. *Ultrasonics Sonochemistry*, *94*, 106346. doi: 10.1016/j.ultsonch.2023.106346

Idbaih, A., Canney, M., Belin, L., Desseaux, C., Vignot, A., Bouchoux, G., ... Carpentier, A. (2019). Safety and feasibility of repeated and transient blood–brain barrier disruption by pulsed ultrasound in patients with recurrent glioblastoma. *Clinical Cancer Research*, *25*(13), 3793-3801. doi: 10.1158/1078-0432.CCR-18-3643

Jiang, Z., Sujarittam, K., Yildiz, B. I., Dickinson, R. J., & Choi, J. J. (2022). Passive cavitation detection with a needle hydrophone array. *IEEE Transactions on Ultrasonics, Ferroelectrics, and Frequency Control*, *69*, 233-240. doi: 10.1109/TUFFC.2021.3120263

Jones, R. M., & Hynynen, K. (2019). Advances in acoustic monitoring and control of focused ultrasound-mediated increases in blood-brain barrier permeability. *British Journal of Radiology*, *92*. doi: 10.1259/bjr.20180601

Jong, N. D., Bouakaz, A., & Frinking, P. (2002). Basic acoustic properties of microbubbles. *Echocardiography*, *19*, 229-240. doi: 10.1046/j.1540-8175.2002.00229.x

Kamimura, H. A. S., Wu, S. Y., Grondin, J., Ji, R., Aurup, C., Zheng, W., ... Konofagou, E. E. (2021). Real-time passive acoustic mapping using sparse matrix multiplication. *IEEE Transactions on Ultrasonics, Ferroelectrics, and Frequency Control*, *68*, 164-177. doi: 10.1109/TUFFC.2020.3001848

Kim, P., Song, J. H., & Song, T. K. (2020). A new frequency domain passive acoustic mapping method using passive hilbert beamforming to reduce the computational complexity of fast fourier transform. *Ultrasonics*, *102*, 106030. doi: 10.1016/j.ultras.2019.106030

Kooiman, K., Roovers, S., Langeveld, S. A., Kleven, R. T., Dewitte, H., O'Reilly, M. A., ... Holland, C. K. (2020). Ultrasound-responsive cavitation nuclei for therapy and drug delivery. *Ultrasound in Medicine and Biology*, *46*, 1296-1325. doi: 10.1016/j.ultrasmedbio.2020.01.002

Lambert, J. M., & Berkenblit, A. (2018). Antibody–drug conjugates for cancer treatment. *Annual Review of Medicine*, *69*(1), 191-207. doi: 10.1146/annurev-med-061516-121357

Li, C., Clegg, H. R., Carpenter, T. M., Nie, L., Freear, S., Cowell, D. M., & McLaughlan, J. R. (2020). Modified passive acoustic mapping with diagnostic-array angular response for cavitation monitoring during HIFU ablation in ex vivo tissue. In *2020 IEEE International Ultrasonics Symposium (IUS)* (p. 1-4). doi: 10.1109/IUS46767.2020.9251786

Li, J., Stoica, P., & Wang, Z. (2003). On robust capon beamforming and diagonal loading. *ICASSP, IEEE International Conference on Acoustics, Speech and Signal Processing - Proceedings*, *5*, 337-340. doi: 10.1109/icassp.2003.1199947

Lin, H.-C., Fan, C.-H., Ho, Y.-J., & Yeh, C.-K. (2020). Dual-frequency chirp excitation for passive cavitation imaging in the brain. *IEEE Transactions on Ultrasonics, Ferroelectrics, and Frequency Control*, *67*, 1127-1140. doi: 10.1109/TUFFC.2020.2964786

Lin, Y., Lin, L., Cheng, M., Jin, L., Du, L., Han, T., ... Qin, P. (2017). Effect of acoustic parameters on the cavitation behavior of sonovue microbubbles induced by pulsed ultrasound. *Ultrasonics Sonochemistry*, *35*, 176-184. doi: 10.1016/J.ULTSONCH.2016.09.016

Lipsman, N., Meng, Y., Bethune, A. J., Huang, Y., Lam, B., Masellis, M., ... Black, S. E. (2018). Blood–brain barrier opening in Alzheimer's disease using MR-guided focused ultrasound. *Nature Communications*, *9*(1), 2336. doi: 10.1038/s41467-018-04529-6

Lu, S., Hu, H., Yu, X., Long, J., Jing, B., Zong, Y., & Wan, M. (2018). Passive acoustic mapping of cavitation using eigenspace-based robust capon beamformer in ultrasound therapy. *Ultrasonics Sonochemistry*, *41*, 670-679. doi: 10.1016/j.ultsonch.2017.10.017

Lu, S., Li, R., Yu, X., Wang, D., & Wan, M. (2019). Delay multiply and sum beamforming method applied to enhance linear-array passive acoustic mapping of ultrasound cavitation. *Medical Physics*, *46*, 4441-4454. doi: 10.1002/mp.13714

Lu, S., Yu, X., Chang, N., Zong, Y., Zhong, H., & Wan, M. (2017). Passive acoustic mapping of cavitation based on frequency sum and robust capon beamformer. In *2017 IEEE International Ultrasonics Symposium (IUS)* (p. 1-4). doi: 10.1109/ULTSYM.2017.8091936

Lu, S., Yu, X., Li, R., Zong, Y., & Wan, M. (2019). Passive cavitation mapping using dual apodization with cross-correlation in ultrasound therapy monitoring. *Ultrasonics Sonochemistry*, *54*, 18-31. doi: 10.1016/j.ultsonch.2019.02.020

Lu, S., Zhao, Y., Yu, X., Li, R., Wang, D., Zhang, B., & Wan, M. (2020). Robust artifacts suppression in ultrasound passive cavitation mapping using multi-apodization with cross-correlation. In *2020 IEEE International Ultrasonics Symposium (IUS)* (p. 1-4). doi: 10.1109/IUS46767.2020.9251527

Lyka, E., Coviello, C., Kozick, R., & Coussios, C. C. (2016, 7). Sum-of-harmonics method for improved narrowband and broadband signal quantification during passive monitoring of ultrasound therapies. *The Journal of the Acoustical Society of America*, *140*, 741-754. doi:

10.1121/1.4958991

Lyka, E., Coviello, C. M., Paverd, C., Gray, M. D., & Coussios, C. C. (2018). Passive acoustic mapping using data-adaptive beamforming based on higher order statistics. *IEEE Transactions on Medical Imaging*, *37*, 2582-2592. doi: 10.1109/TMI.2018.2843291

Maffett, R., Boni, E., Chee, A. J. Y., Yiu, B. Y. S., Savoia, A. S., Ramalli, A., ... Yu, A. C. H. (2022). Unfocused field analysis of a density-tapered spiral array for high-volume-rate 3-d ultrasound imaging. *IEEE Transactions on Ultrasonics, Ferroelectrics, and Frequency Control*, *69*(10), 2810-2822. doi: 10.1109/TUFFC.2022.3188245

Mainprize, T., Lipsman, N., Huang, Y., Meng, Y., Bethune, A., Ironside, S., ... Hynynen, K. (2019). Blood-brain barrier opening in primary brain tumors with non-invasive mr-guided focused ultrasound: A clinical safety and feasibility study. *Scientific Reports*, *9*(1), 321. doi: 10.1038/s41598-018-36340-0

Martinez, P., Bottenus, N., & Borden, M. (2022). Cavitation characterization of size-isolated microbubbles in a vessel phantom using focused ultrasound. *Pharmaceutics*, *14*. doi: 10.3390/pharmaceutics14091925

O'Reilly, M. A., Jones, R. M., & Hynynen, K. (2014). Three-dimensional transcranial ultrasound imaging of microbubble clouds using a sparse hemispherical array. *IEEE Transactions on Biomedical Engineering*, *61*, 1285-1294. doi: 10.1109/TBME.2014.2300838

Padilla, F., & ter Haar, G. (2022). Recommendations for reporting therapeutic ultrasound treatment parameters. *Ultrasound in Medicine and Biology*, *48*, 1299-1308. doi: 10.1016/j.ultrasmedbio.2022.03.001

Polichetti, M., Varray, F., Gilles, B., Bera, J. C., & Nicolas, B. (2021). Use of the cross-spectral density matrix for enhanced passive ultrasound imaging of cavitation. *IEEE Transactions on Ultrasonics, Ferroelectrics, and Frequency Control*, *68*, 910-925. doi: 10.1109/TUFFC.2020.3032345

Roovers, S., Segers, T., Lajoinie, G., Deprez, J., Versluis, M., Smedt, S. C. D., & Lentacker, I. (2019). The role of ultrasound-driven microbubble dynamics in drug delivery: From microbubble fundamentals to clinical translation. *Langmuir*, *35*, 10173-10191. doi: 10.1021/acs.langmuir.8b03779

Salgaonkar, V. A., Datta, S., Holland, C. K., & Mast, T. D. (2009). Passive cavitation imaging with ultrasound arrays. *The Journal of the Acoustical Society of America*, *126*, 3071-3083.

doi: 10.1121/1.3238260

Schoen, S., & Arvanitis, C. D. (2020a). Acoustic source localization with the angular spectrum approach in continuously stratified media. *The Journal of the Acoustical Society of America*, *148*, EL333-EL339. doi: 10.1121/10.0002095

Schoen, S., & Arvanitis, C. D. (2020b). Heterogeneous angular spectrum method for trans-skull imaging and focusing. *IEEE Transactions on Medical Imaging*, *39*, 1605-1614. doi: 10.1109/TMI.2019.2953872

Segers, T., Kruizinga, P., Kok, M. P., Lajoinie, G., de Jong, N., & Versluis, M. (2018). Monodisperse versus polydisperse ultrasound contrast agents: Non-linear response, sensitivity, and deep tissue imaging potential. *Ultrasound in Medicine and Biology*, *44*(7), 1482-1492. doi: 10.1016/j.ultrasmedbio.2018.03.019

Smith, C. A., & Coussios, C. C. (2020). Spatiotemporal assessment of the cellular safety of cavitation-based therapies by passive acoustic mapping. *Ultrasound in Medicine and Biology*, *46*, 1235-1243. doi: 10.1016/J.ULTRASMEDBIO.2020.01.009

Stoica, P., Wang, Z., & Li, J. (2003, 6). Robust capon beamforming. *IEEE Signal Processing Letters*, *10*, 172-175. doi: 10.1109/LSP.2003.811637

Stride, E., & Coussios, C. (2019). Nucleation, mapping and control of cavitation for drug delivery. *Nature Reviews Physics*, *1*, 495-509. doi: 10.1038/s42254-019-0074-y

Telichko, A. V., Lee, T., Hyun, D., Chowdhury, S. M., Bachawal, S., Herickhoff, C. D., ... Dahl, J. J. (2021). Passive cavitation mapping by cavitation source localization from aperture-domain signals - part ii: Phantom and in vivo experiments. *IEEE Transactions on Ultrasonics, Ferroelectrics, and Frequency Control*, *68*, 1198-1212. doi: 10.1109/TUFFC.2020.3035709

Telichko, A. V., Lee, T., Jakovljevic, M., & Dahl, J. J. (2021). Passive cavitation mapping by cavitation source localization from aperture-domain signals - part i: Theory and validation through simulations. *IEEE Transactions on Ultrasonics, Ferroelectrics, and Frequency Control*, *68*, 1184-1197. doi: 10.1109/TUFFC.2020.3035696

Van Veen, B., & Buckley, K. (1988). Beamforming: a versatile approach to spatial filtering. *IEEE ASSP Magazine*, *5*(2), 4-24. doi: 10.1109/53.665

Wilson, W. D. (1959). Speed of sound in distilled water as a function of temperature and pressure. *The Journal of the Acoustical Society of America*, *31*(8), 1067-1072. doi: 10.1121/

1.1907828

Wu, S. Y., Tung, Y. S., Marquet, F., Downs, M., Sanchez, C., Chen, C., ... Konofagou, E. E. (2014). Transcranial cavitation detection in primates during blood-brain barrier opening-a performance assessment study. *IEEE Transactions on Ultrasonics, Ferroelectrics, and Frequency Control*, *61*, 966-978. doi: 10.1109/TUFFC.2014.2992

Xu, H., He, L., Zhong, B., Qiu, J., & Tu, J. (2019). Classification and prediction of inertial cavitation activity induced by pulsed high-intensity focused ultrasound. *Ultrasonics Sonochemistry*, *56*, 77-83. doi: 10.1016/j.ultsonch.2019.03.031

Zhou, B., Lian, Q., Jin, C., Lu, J., Xu, L., Gong, X., & Zhou, P. (2022). Human clinical trial using diagnostic ultrasound and microbubbles to enhance neoadjuvant chemotherapy in her2- negative breast cancer. *Frontiers in Oncology*, *12*. doi: 10.3389/fonc.2022.992774

APPENDICES

Appendix A

Additional PCM Plots

A.1 Cavitation Map 3D Comparisons

A.1.1 Cavitation Maps vs. Frequency

This section presents the 3D comparison plots with constant pressure for experiments N2 and N3, which were not shown in Section 4.5 Figure 4.6.

A.1.2 Cavitation Maps vs. Pressure

This section presents the 3D comparison plots with at constant beamformed frequency bands – harmonic, ultraharmonic, and broadband – for experiments N2 and N3 (Figures A.5 and A.6) that were not shown in Figure 4.3. These are followed by 3D comparison plots at certain constant narrowband frequencies – 5, 5.5, and 8 MHz – for experiments N1-N3 in Figures A.7, A.8, and A.9, to illustrate the source localization trends mentioned in Section 4.5.2.

A.2 Cavitation Dose vs. Pressure

This section extends on Section 4.3.2 Figure 4.4, showing all plots of the cavitation dose from PCM maps vs. pressure for each frequency band and for each experiment (labelled N1 to N3).

A.3 Percent Difference Cavitation Dose from FDAS vs. Pressure

This section presents the pairwise percent differences from FDAS in response to pressure, for experimental conditions above the cavitation thresholds. The following figures show all plots of the cavitation dose percent differences each frequency band and for each experiment (labelled N1 to N3). The lines follow the median % differences and the shaded bars are the IQR of the % differences in the 15 frames. These are the medians and IQRs summarized in Section 4.4 Figure 4.5A and B respectively.

A.4 PCD vs. PCM

The following figures present the comparison between PCD and PCM spectra for each experiment (N1-N3) corresponding to the results presented in Section 4.7. Note that Figure A.16 is a duplicate of Figure 4.9 but is shown here again for ease of comparison with the other two experimental repetitions.

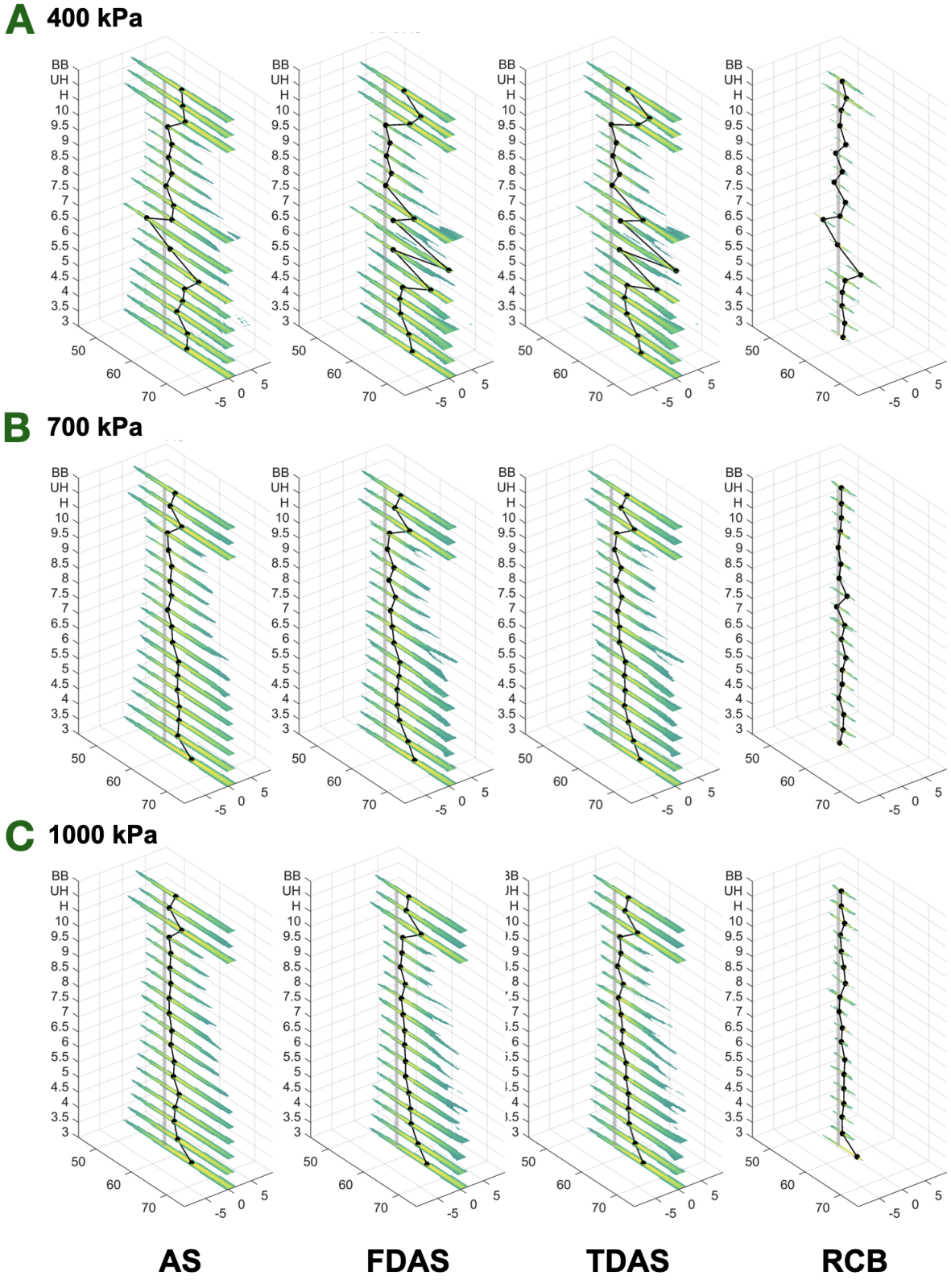


Figure A.1: 3D PCM comparisons vs. frequency at 400, 700, and 1000 kPa (N1)

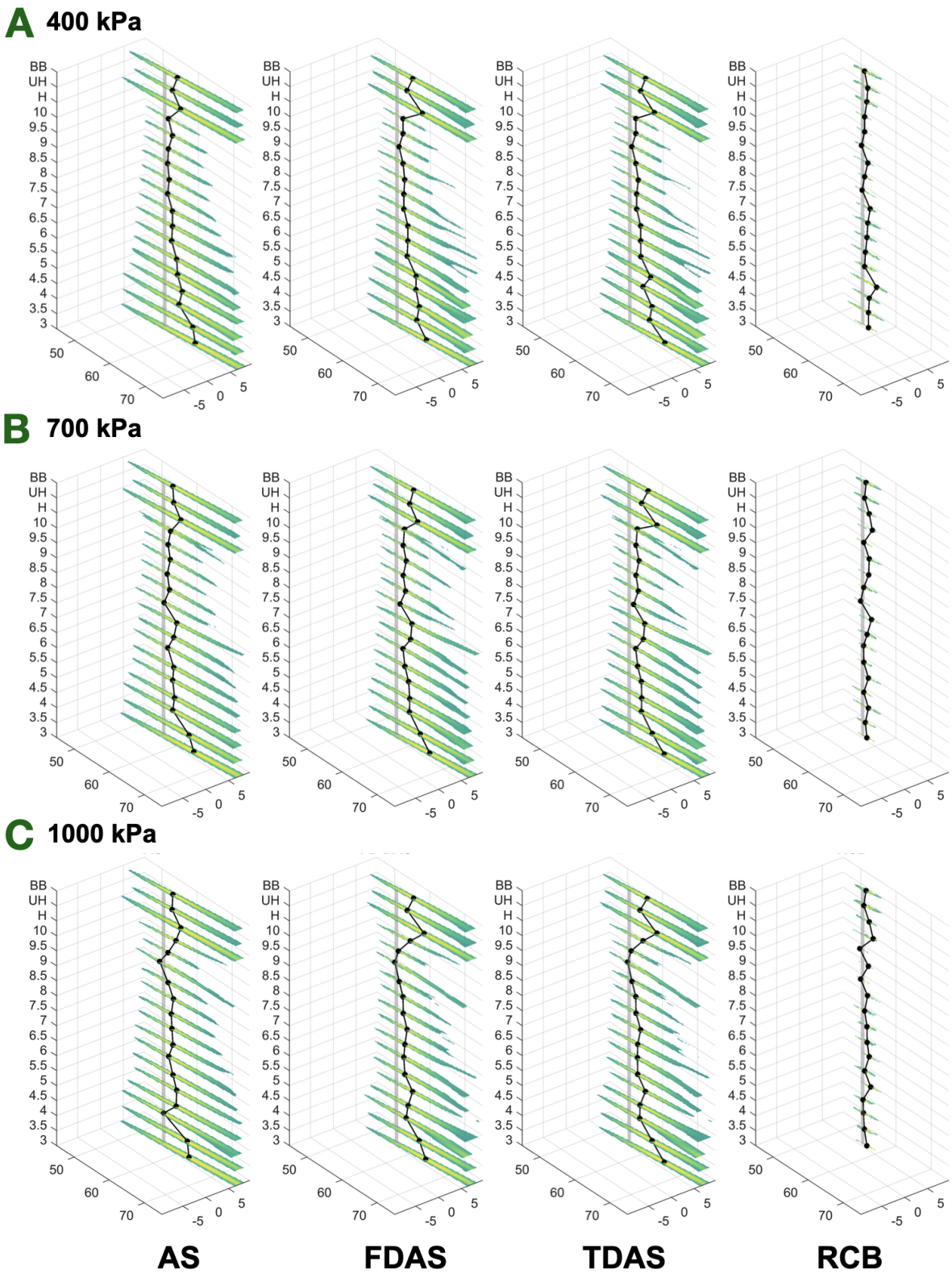


Figure A.2: 3D PCM comparisons vs. frequency at 400, 700, and 1000 kPa (N2)

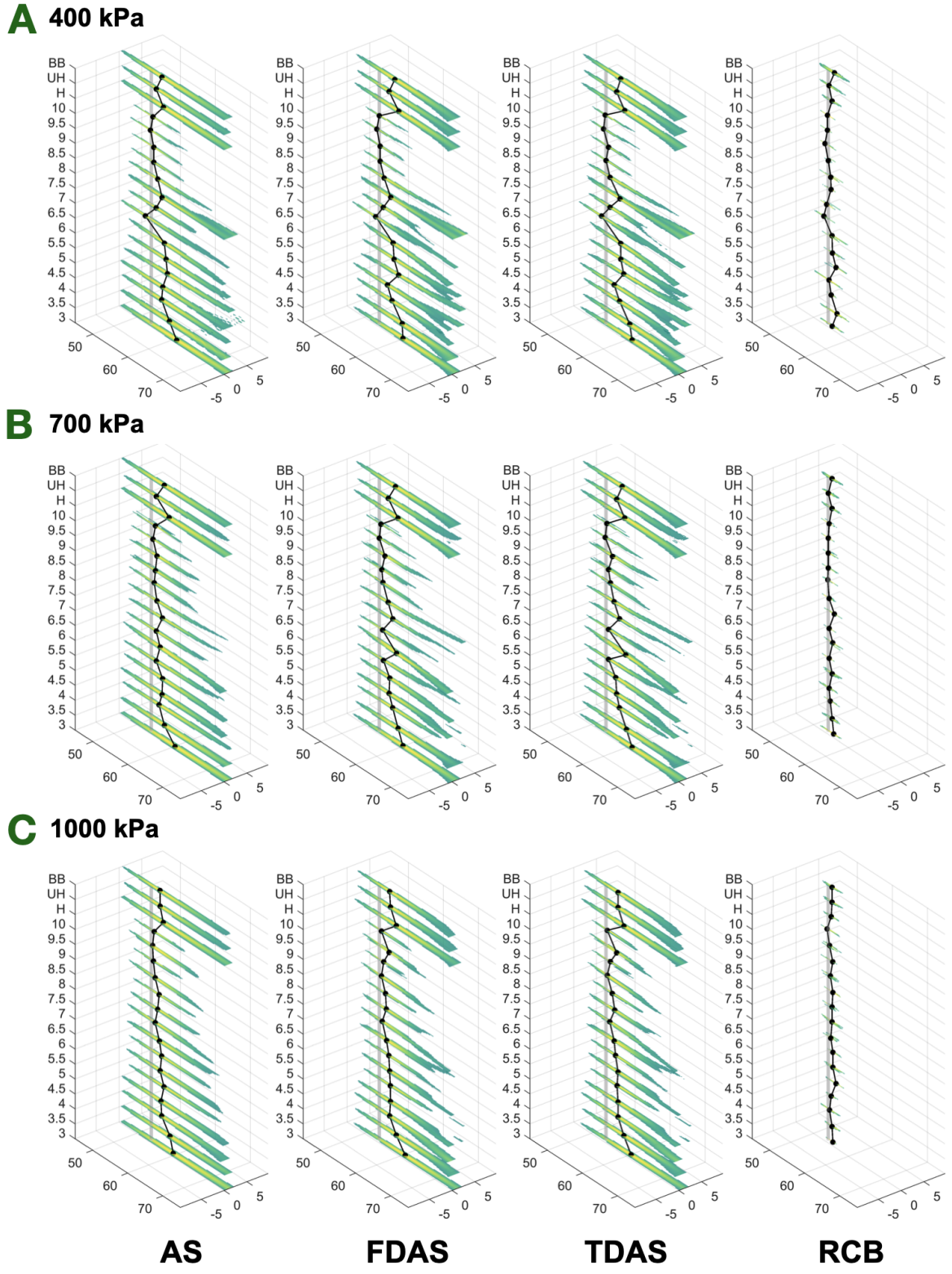


Figure A.3: 3D PCM comparisons vs. frequency at 400, 700, and 1000 kPa (N3)

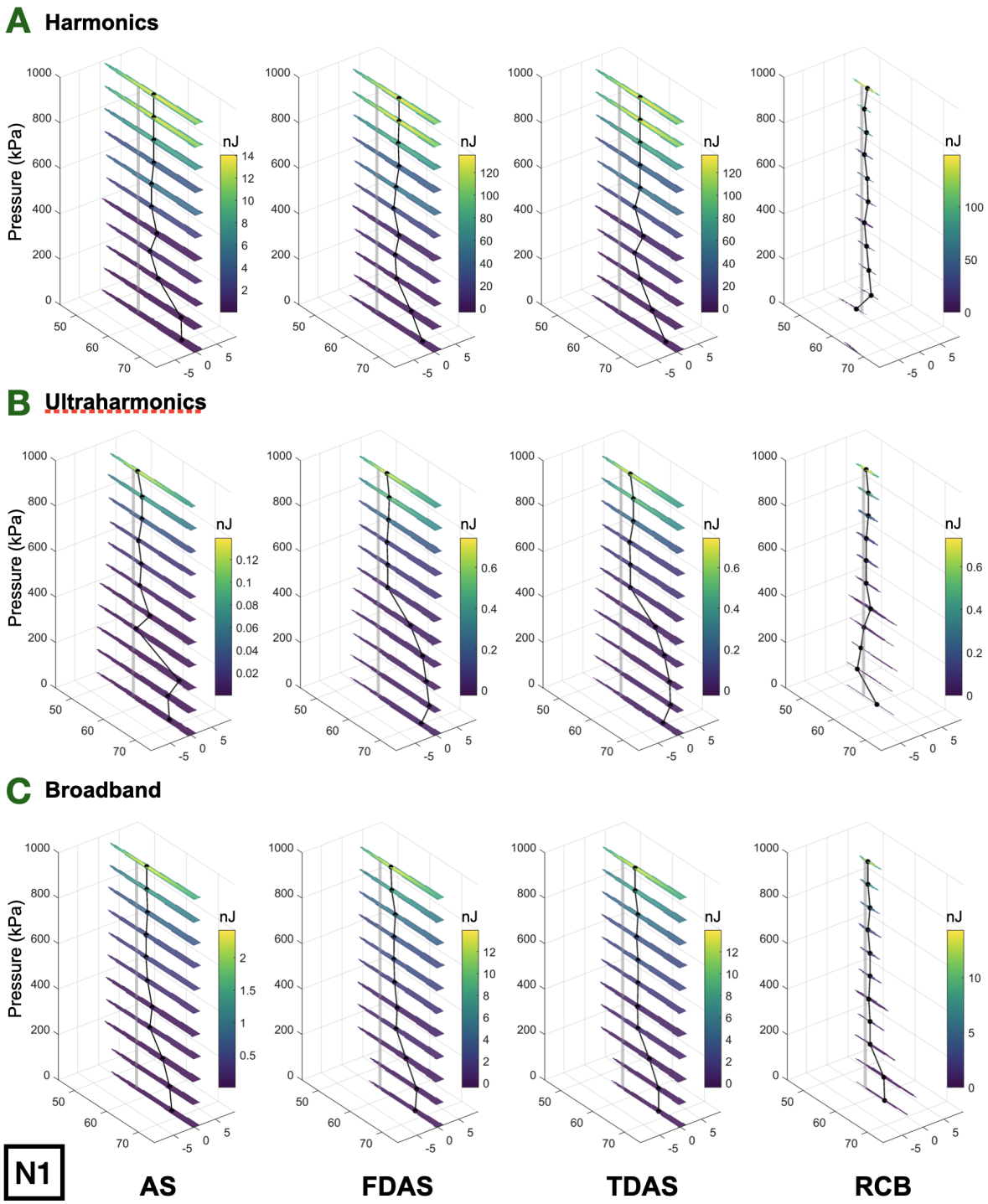


Figure A.4: 3D PCM comparisons vs. pressure at H, UH, BB bands (N1)

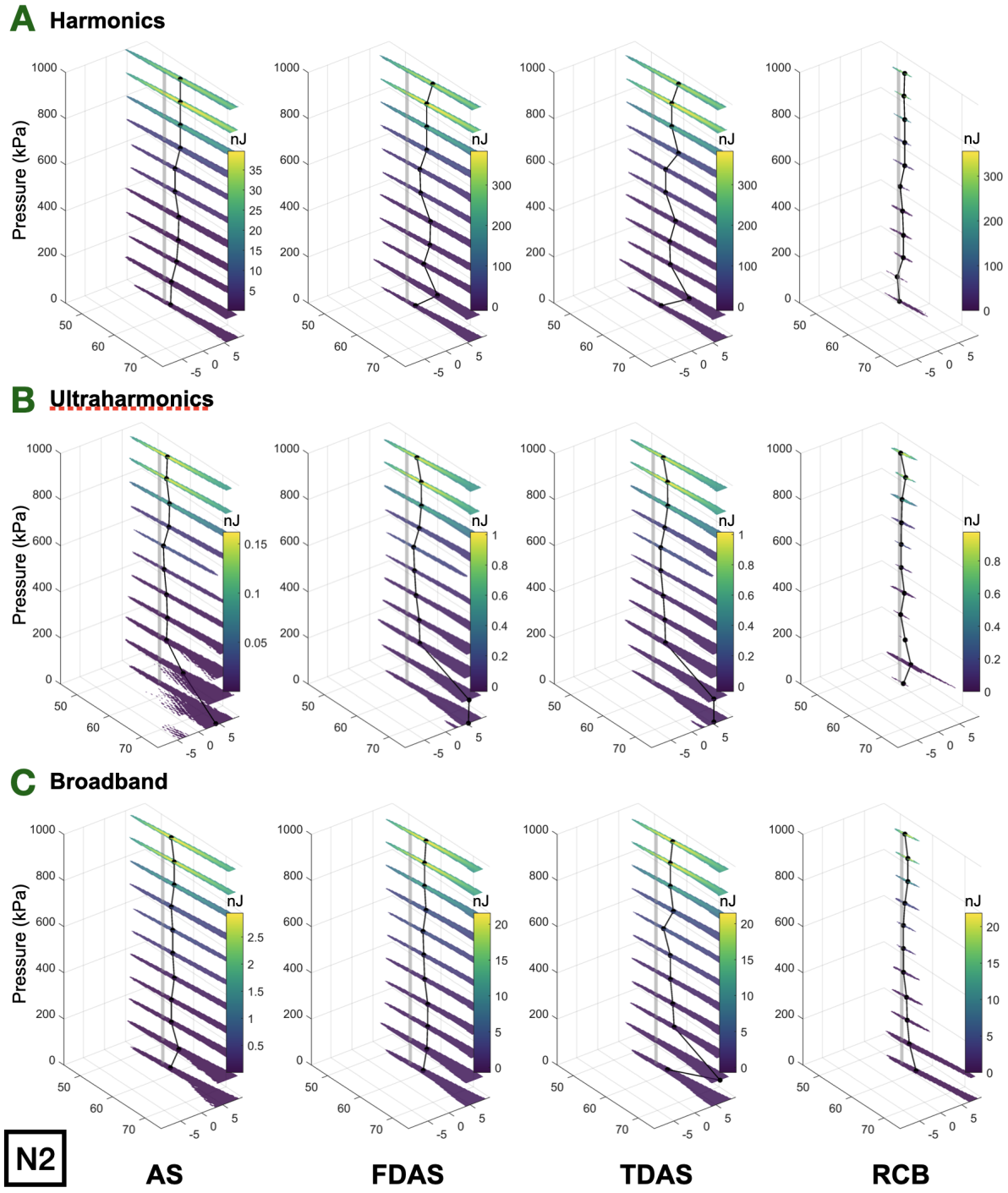


Figure A.5: 3D PCM comparisons vs. pressure at H, UH, BB bands (N2)

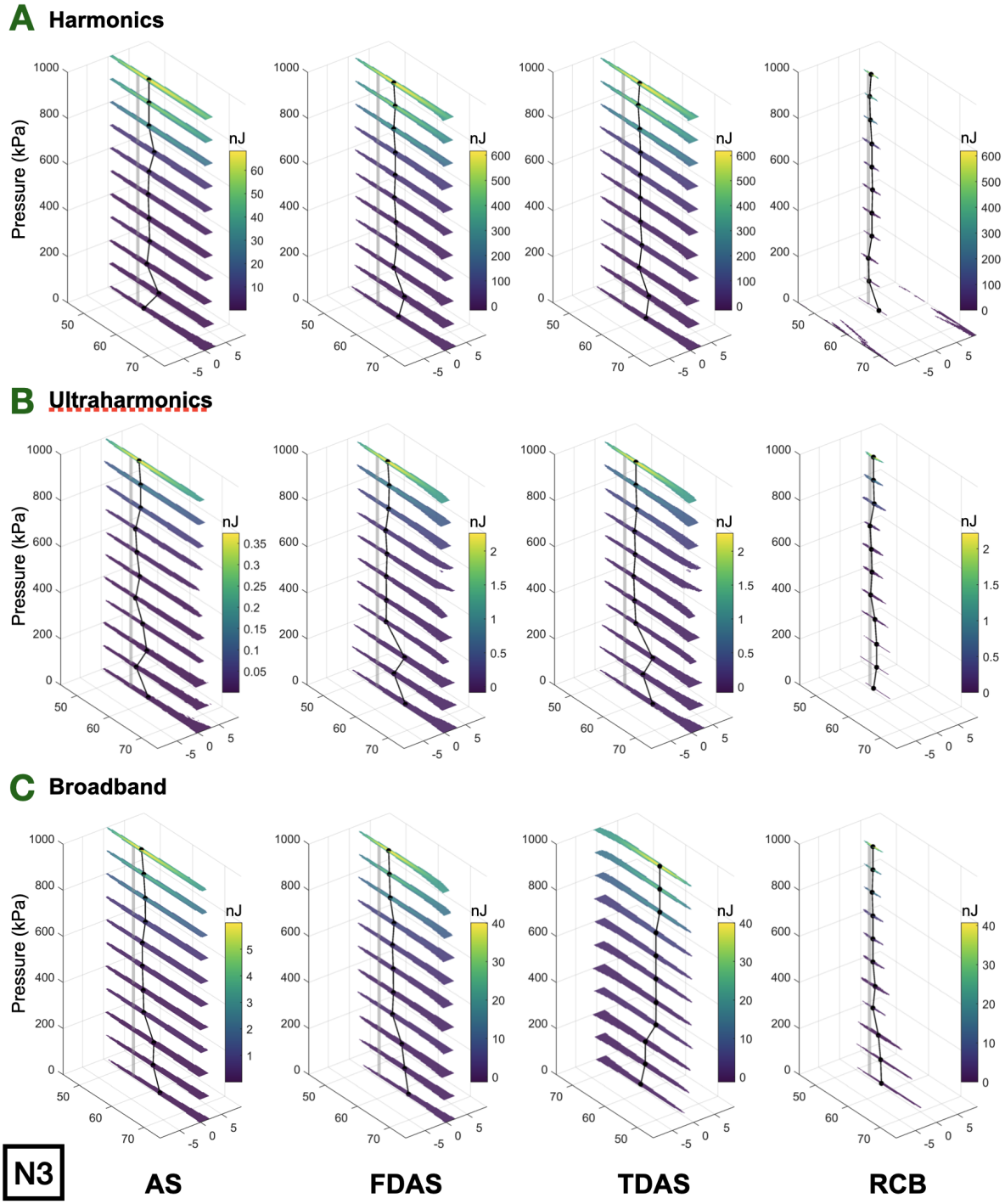


Figure A.6: 3D PCM comparisons vs. pressure at H, UH, BB bands (N3)

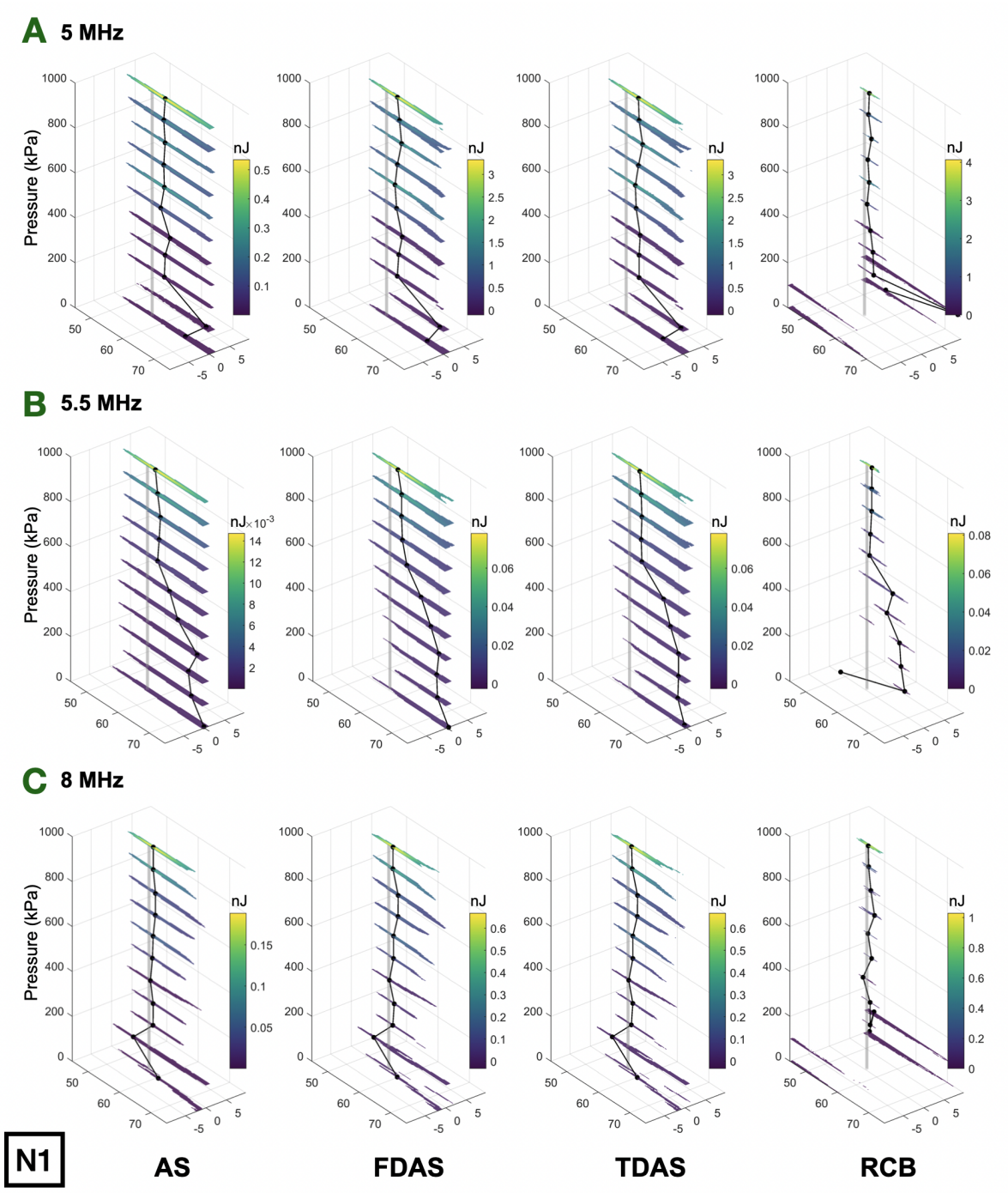


Figure A.7: 3D PCM comparisons vs. pressure at 5, 5.5 and 8 MHz bands (N1)

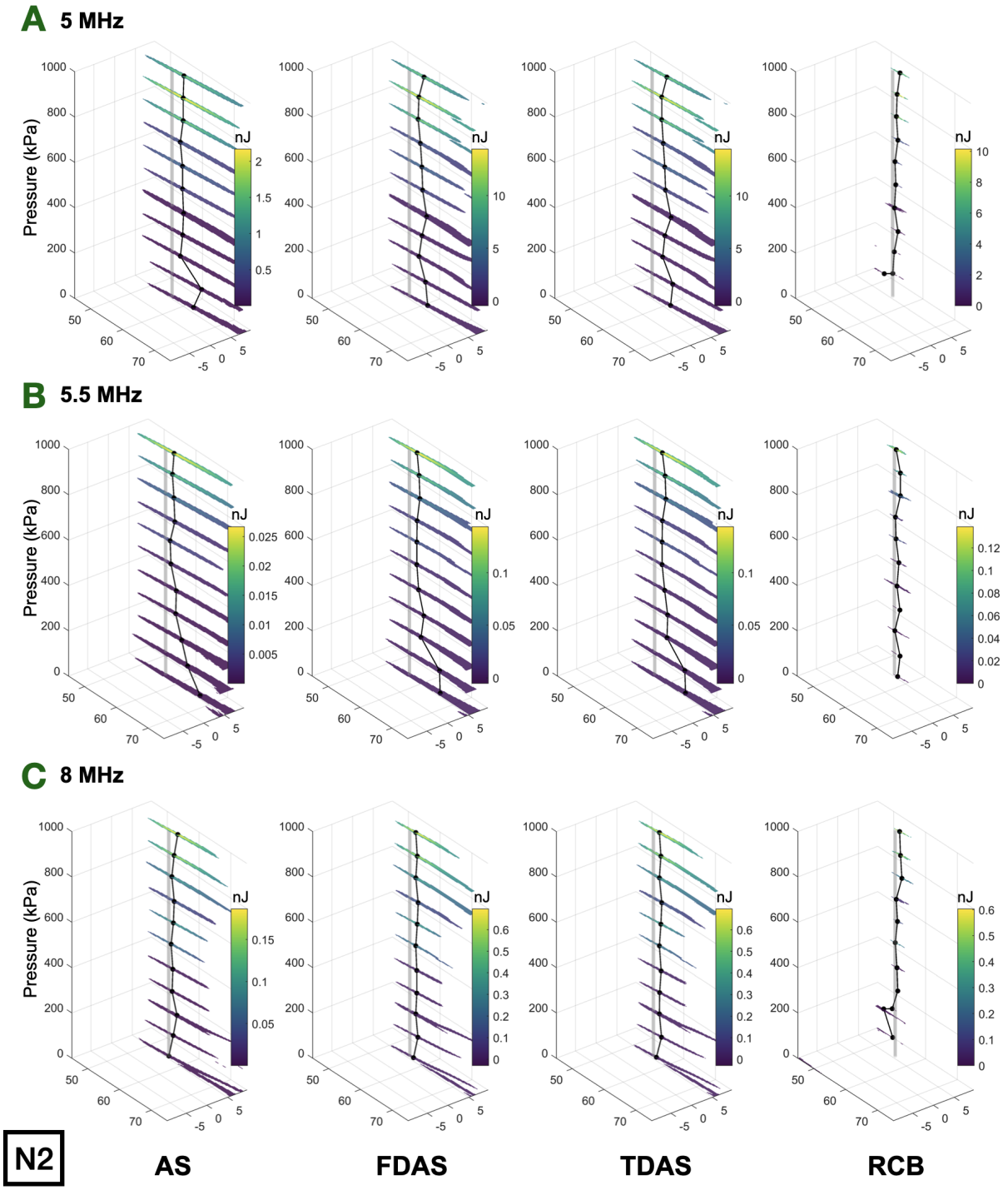


Figure A.8: 3D PCM comparisons vs. pressure at 5, 5.5 and 8 MHz bands (N2)

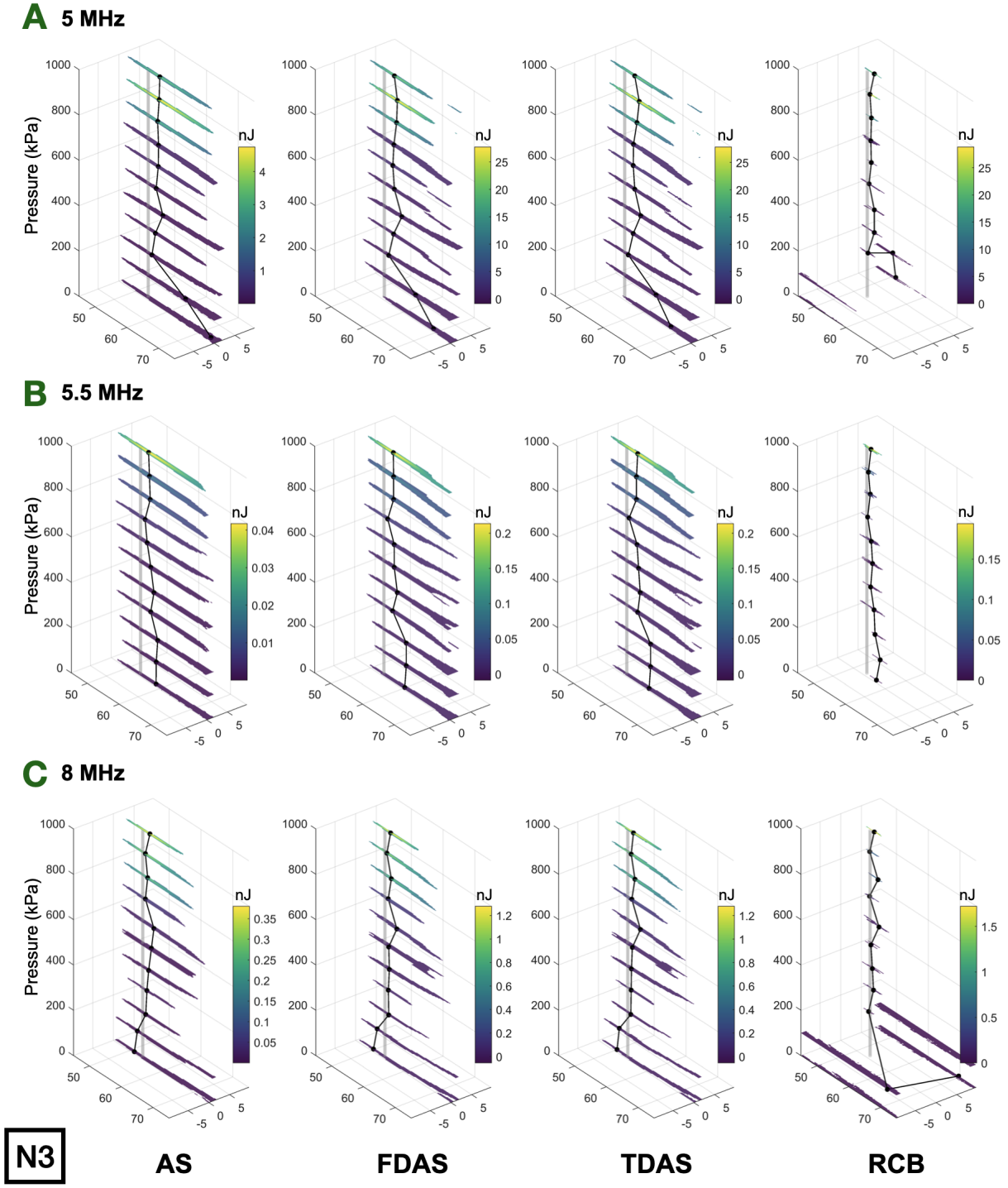


Figure A.9: 3D PCM comparisons vs. pressure at 5, 5.5 and 8 MHz bands (N3)

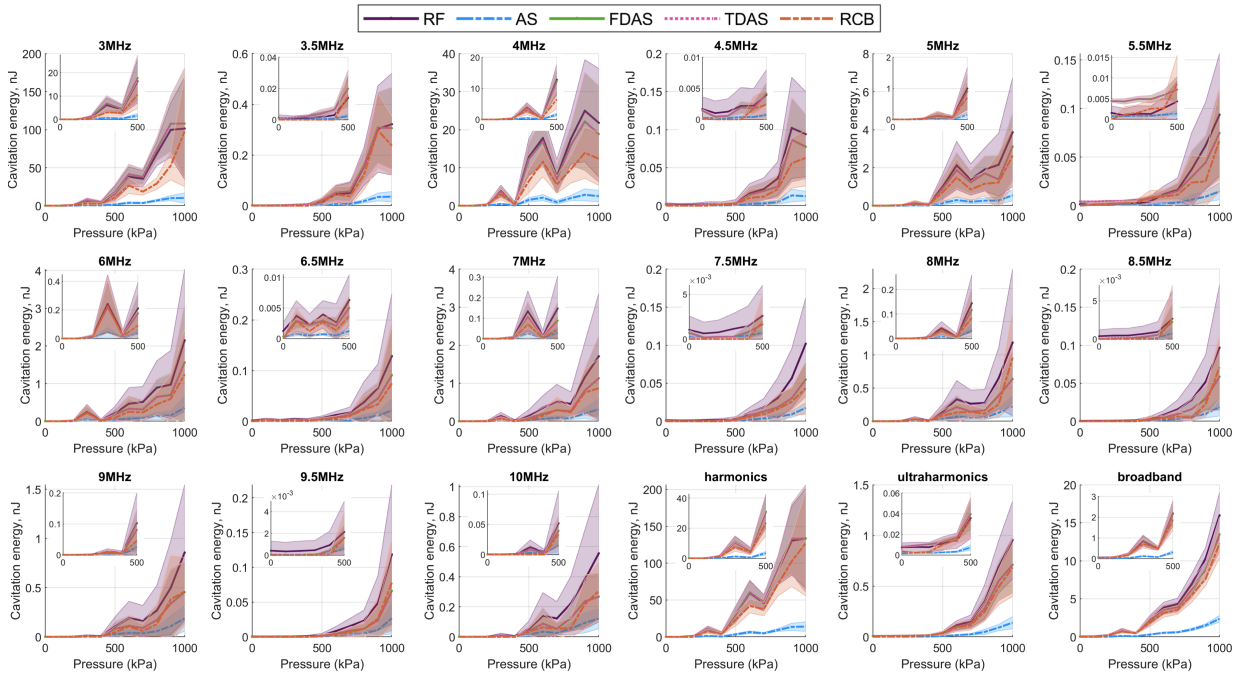


Figure A.10: PCM Dose vs. Pressure at all frequency bands (N1)

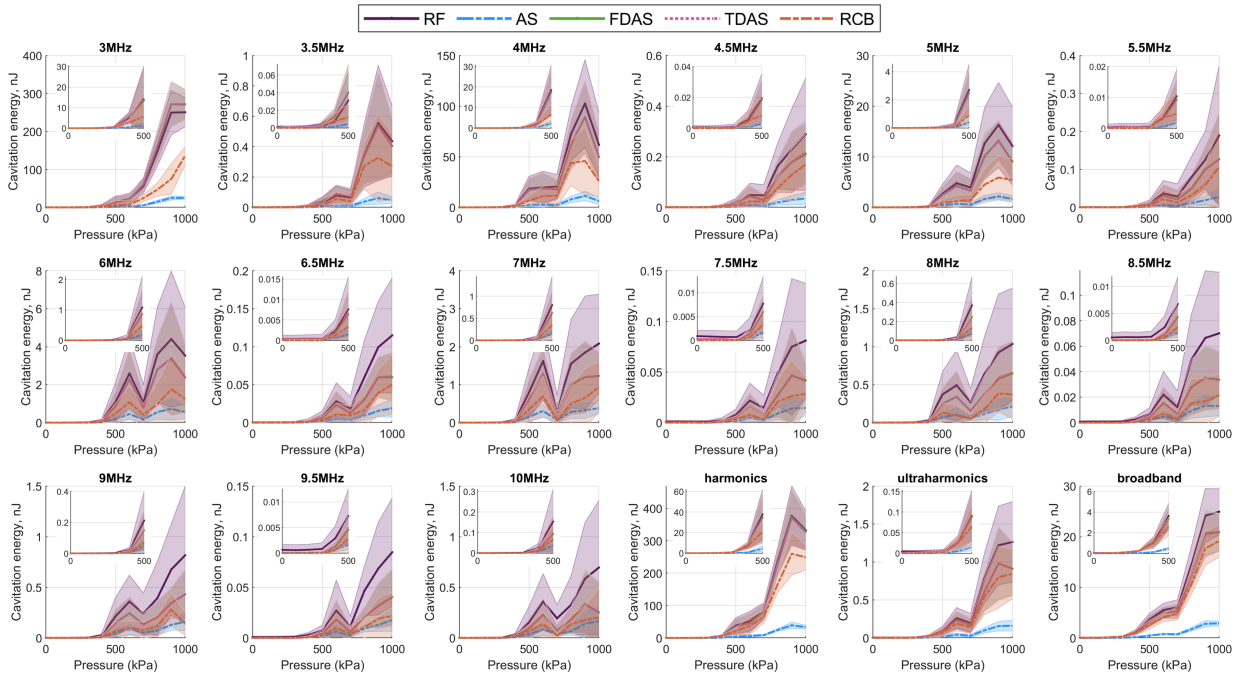


Figure A.11: PCM Dose vs. Pressure at all frequency bands (N2)

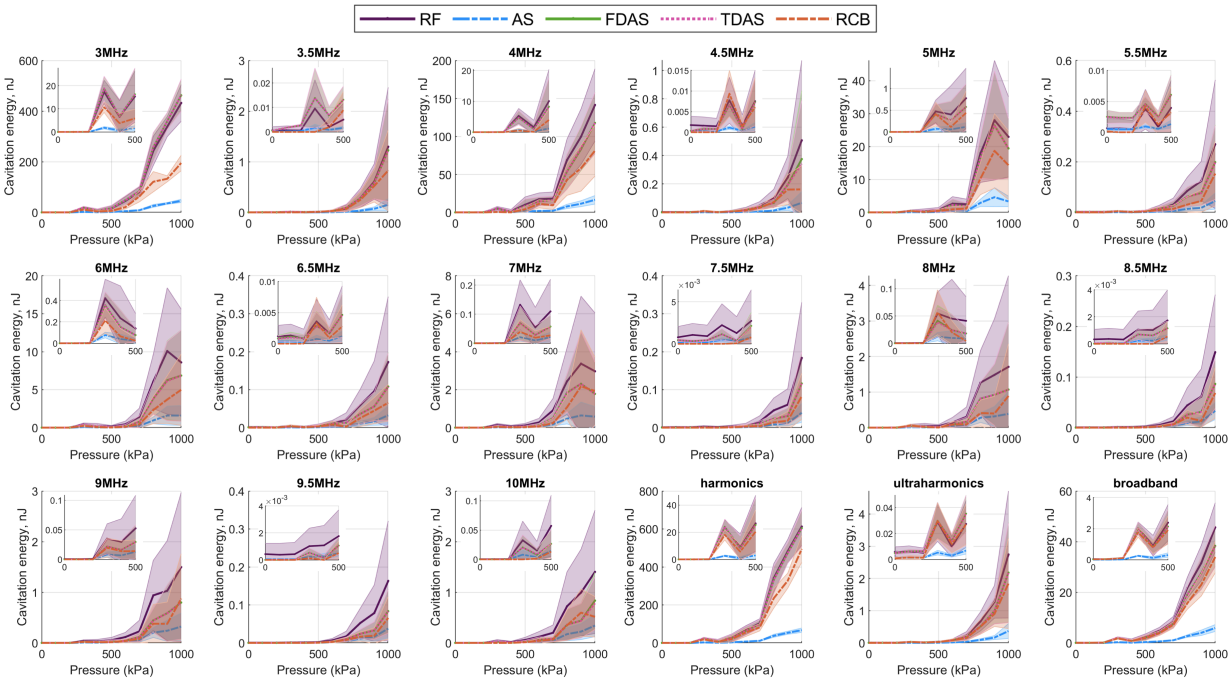


Figure A.12: PCM Dose vs. Pressure at all frequency bands (N3)

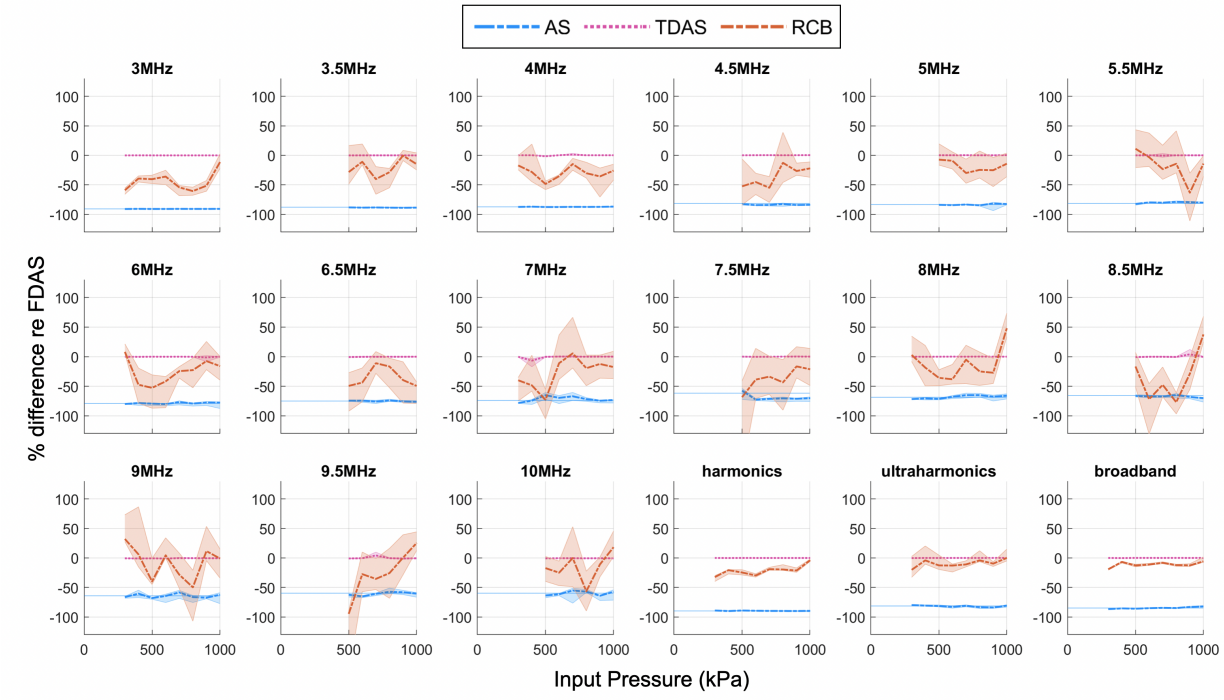


Figure A.13: PCM Dose Differences vs. Pressure at all frequency bands (N1)

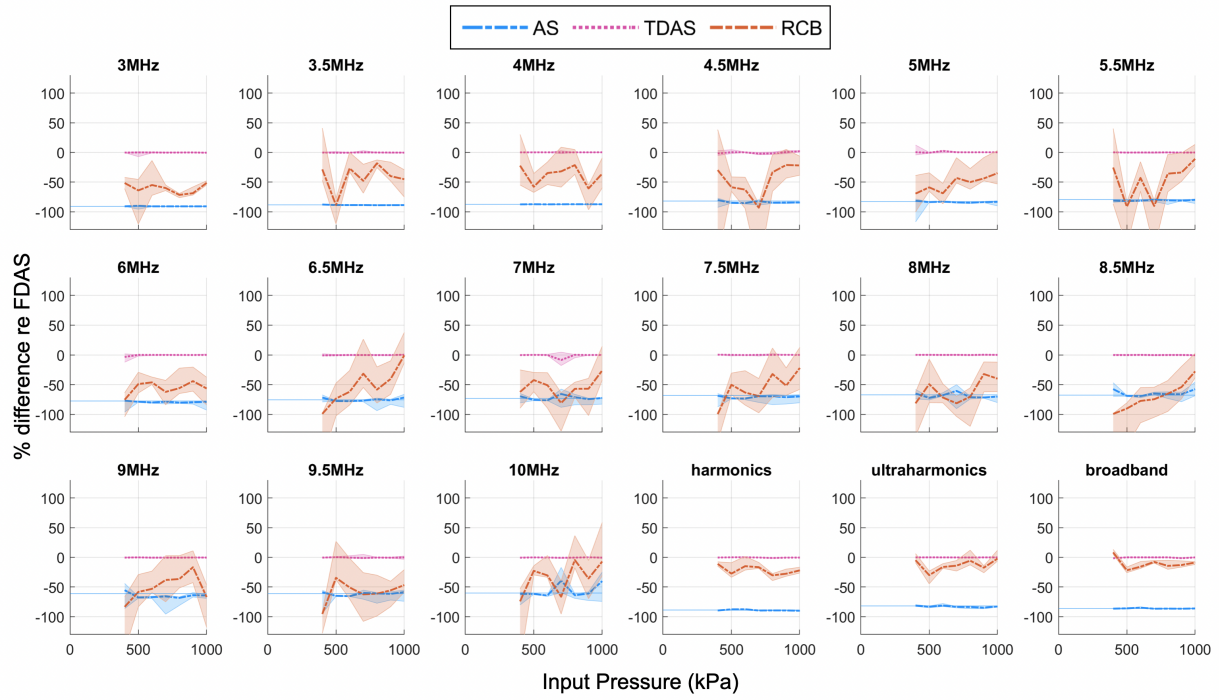


Figure A.14: PCM Dose Differences vs. Pressure at all frequency bands (N2)

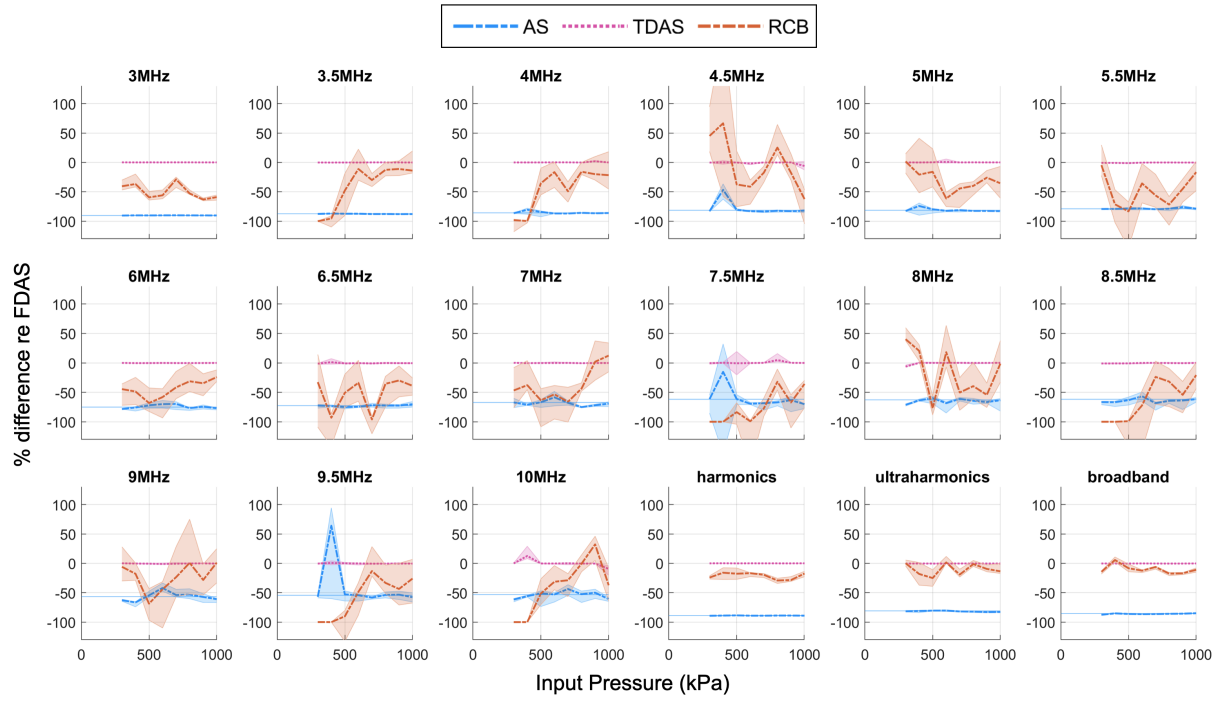


Figure A.15: PCM Dose Differences vs. Pressure at all frequency bands (N3)

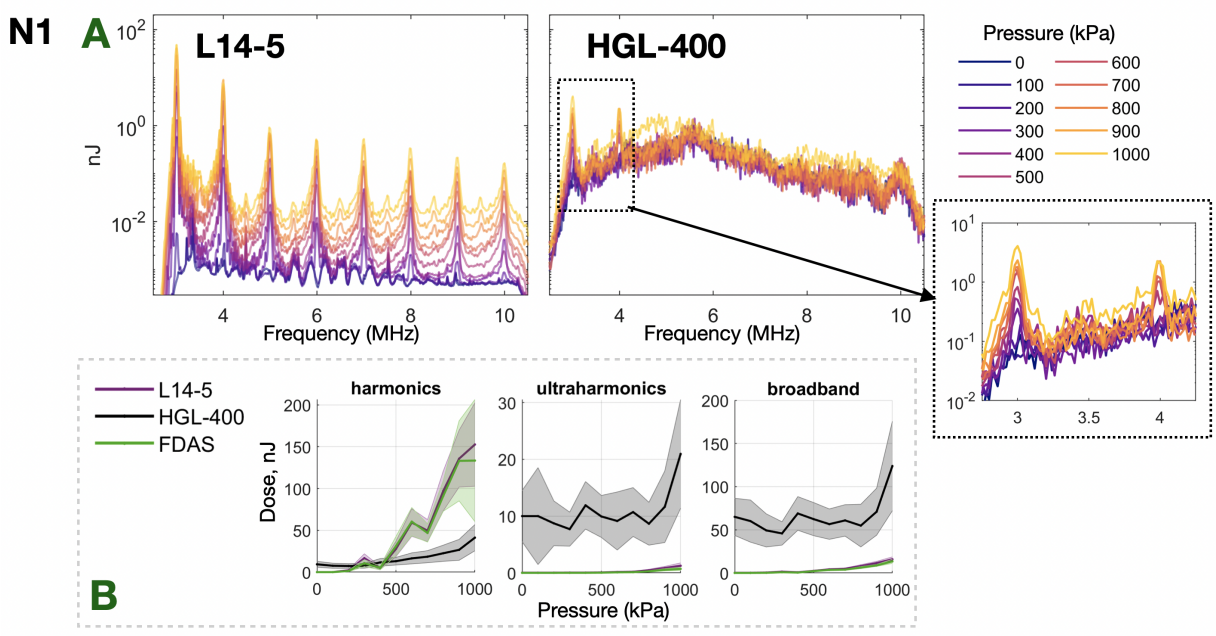


Figure A.16: PCD spectra vs. PCM spectra (N1)

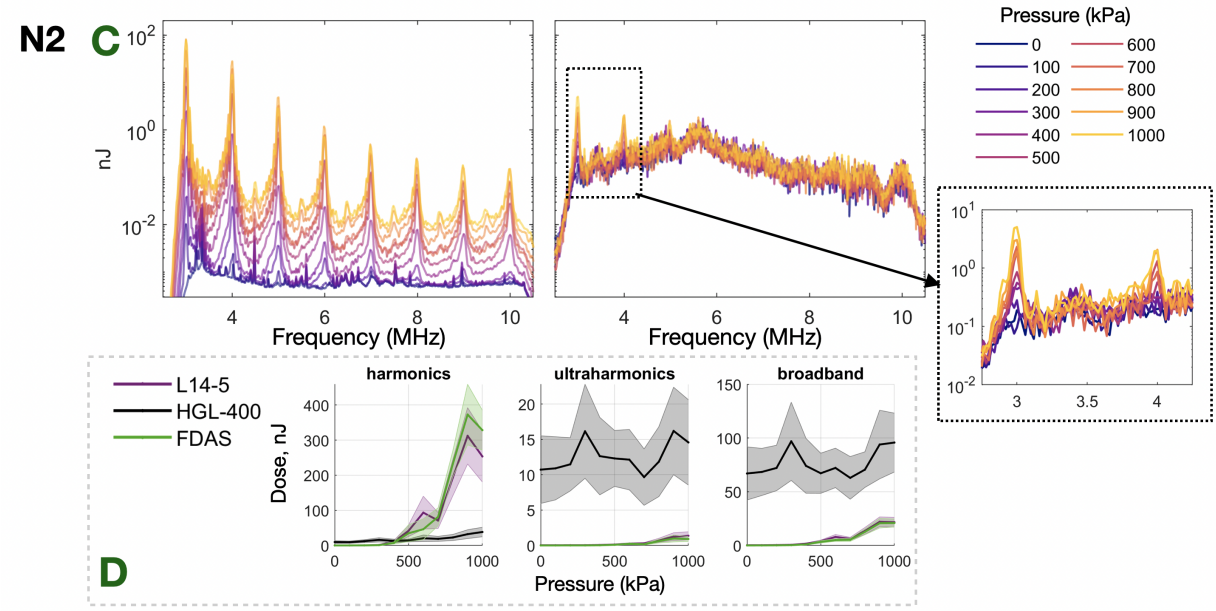


Figure A.17: PCD spectra vs. PCM spectra (N2)

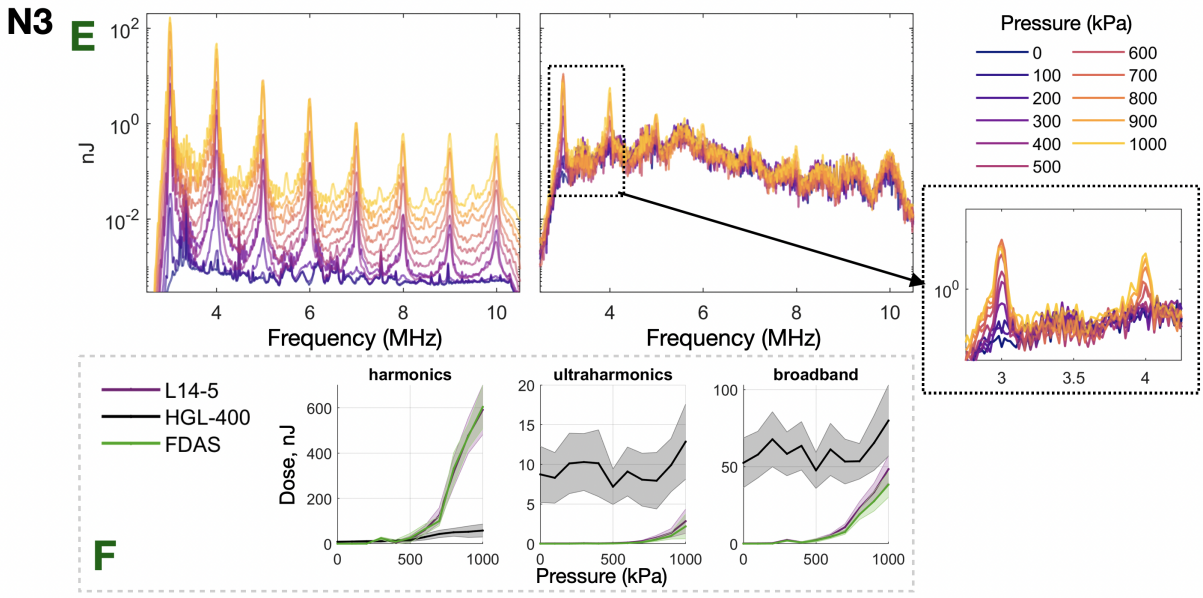


Figure A.18: PCD spectra vs. PCM spectra (N3)